Equilibrium Molecular Dynamics Study of Phonon Transport Properties at High Temperatures

by

Jalaan Avritte

A dissertation submitted to the Graduate Faculty of
Auburn University
in partial fulfillment of the
requirements for the Degree of
Doctor of Philosophy

Auburn, Alabama
December 9, 2023

Keywords: Molecular Dynamics, Thermal Conductivity, Phonon Transport, High Temperature, Gaussian Approximation Potential, Green-Kubo, Relaxation Time Approximation, Silicon

Approved by

Jianjun Dong, Chair, Professor of Physics
Marcelo A. Kuroda, Associate Professor of Physics
Yu Lin, Alumni Professor
Rafael Bernardi, Assistant Professor

Abstract

Thermal conductivity is a material property of great importance in many areas of physics including coat barriers, renewable energy, nano-electronic devices, and geological processes inside the Earth. At the microscopic level, two type of heat carriers, electronic and vibrational, regulate this macroscopic heat transport property. The lattice thermal conductivity, from lattice vibrations or phonons, dominates in semiconductors or insulators at moderate temperatures while the electronic contribution is non-negligible at ambient temperatures. While experiments are only able to measure the total conductivity, extrapolation equations are given to estimate the lattice component. Traditionally, perturbation theory predicts a temperature (T) dependence of the form $\frac{1}{T}$ at high temperatures within the Peierl's heat flux approximation and three-phonon scattering mechanisms yet the experimental extrapolations do not have the same predictions. Even for simple crystals, such as Si, the temperature dependence of the lattice conductivity remain speculative near the melting point (1680K for Si)

Alternatively, molecular dynamic (MD) simulations can be used to get a non-perturbative modelling of anharmonic lattice dynamics, but calculations of the thermal conductivity with equilibrium and non-equilibrium MD is susceptible to accuracy issues, such as finite-size effect, reliability of the inter-atomic potential, and requirements of large number of ensembles. In this work, we focus on the high temperature regime of diamond-lattice Silicon through Large-scale Atomic/Molecular Massively Parallel Simulator (LAMMPS) with the highly accurate Gaussian Approximation Potential (GAP) machine-learning inter-atomic potential.

First, we calculate the thermal conductivity with renormalized phonon frequency and life-time given the q-projected velocity auto-correlation function (ACF). The damp harmonic oscillator theory is validated at high temperature and the q-space symmetry is used to reduce the necessary large number of ensembles by averaging over equivalent q-points, with a mean equivalence number of 24. A fitting algorithm, utilizing LMFIT, is developed to fix the sensitivity of the phonon lifetime parameter by implementing an "accidental degeneracy" constraint if

non-degenerate mode frequencies are too close relative to the MD resolution. When compared to similar perturbation calculations, we find that the simulation parameters of 100 ps simulation time may induce sampling issues of the acoustic mode with long lifetimes that leads to severe underestimation of the thermal conductivity.

Then, we calculate the thermal conductivity through the Green-Kubo formalism with different orders of the heat flux auto-correlation function (HFACF) based on the Hardy heat flux operator. Applying an orthogonality rule to the second-order HFACF mitigates convergence issues when integrating the correlation function, enabling us to confirm the underestimation of phonon lifetimes. A unified transport theory, based on the second-order HFACF, is discussed that combines the inter-mode, intra-mode HFACF and the cross-correlation term, where the intra-term corresponds to the Peierl's heat flux discussed above. Our MD simulations independently confirmed that the conductivity, from the inter-mode HFACF, is comparable to Wigner transport equation results at room temperature and saturates to 0.32 W/(m-K) at 1500K. In contrast, the conductivity, from the cross-correlation term, lowers the overall prediction by about -1 W/(m-K) at all temperatures and this term is neglected by the Wigner transport equation, as well as all the recently proposed unified theory.

Finally, we perform at q-projected force fitting to get the temperature-dependent higher-order force constant (FC) matrices, namely the third- and fourth- order anharmonic and use them for the higher-order HFACF. The effective fourth-order FC matrix with a selection rule $\Delta(-\vec{q}+\vec{q_2})$ provided no improvements to q-projected force fitting when used in conjunction with the bare or renormalized FC_2 and a different approach should be used to handle the fourth-order effects. We demonstrate that a similar orthogonality rule to the one applied to the second-order HFACF enhances convergence by integration of the third-order HFACF. Only accounting for the third-order HFACF lowers the overall conductivity prediction and an improved method of the fourth-order FC is needed to clarify the importance of the fourth-order anharmonicity at high temperatures.

Acknowledgments

Well, this is unprecedented. I'm actually speechless. I put so much into the Defense acknowledgements that "I open my laptop and the words won't type out"...I think that's how the phrase goes.

First, I'd like to thank my advisor Dr. Jianjun Dong for taking in a former experimental physicist just so I can prove a point. Also, I'd like to acknowledge Dave Patrick, Dr. Allen Landers, and Auburn's Hopper and Easley Supercomputing Cluster because without them, I would not be here. I hear funding is very important and without that for the last year and a half, I would not have been as productive at writing as I would have been otherwise.

I would like to thank the members of JACS (Jalaan's Awesome Committee Squad) consisting of Dr. Marcelo Kuroda, Dr. Yu Lin, Dr. Rafael Bernardi, and Dr. Ziqin Feng. I hope all the evidence from my first oral exam is burned and sealed behind double concrete walls to never be seen again.

My current and former lab group members, David Crawford and Dr. Yi Zeng were tremendous in helping various aspects of my research.

All the pillars of my academic journey deserve their recognition. Dr Diane Reeder, my highschool physics teacher, was the reason for me choosing physics. I was just looking at various high paying careers in high school and was like "I guess engineering works". Then, on that fateful day, she told me to do physics instead and because I'm stubborn, I stuck with it. For those who don't know, I slept in class A LOT and she put a student in charge to constantly keep me awake (clearly it didn't stick). Dr. Murray Daw, my freshman physics teacher, broke the mold of how I expect physics classes to be taught. Not only did he care about his students having an excellent foundation of physics, but he took the time to make everyone feel a part of the journey. Even though, I did sleep in his class too, I hear from the grapevines that he speaks highly of me when I'm not around...or maybe I was daydreaming about that. Dr. Jian He, former teacher turned research advisor, was one of the sweetest people I've ever met in academia.

He passed away a few years ago and it would've been nice for him to be a part of this moment. He was beyond patient with me even when I was falling asleep while he taught me how to grow crystals. There might be a reoccurring theme of me being sleepy all the time. Lastly, Dr. Kimberly Mulligan-Guy, Assistant Dean for Inclusion, Equity, and Diversity in COSAM, has always been supportive and helped me put together one of my favorite events to this date, CODEWORKS, with Dr. Ashley Williams. Being able to put an event together to teach kids of underrepresented groups how to code by building hands-on projects was exceptional and I still can't believe it actually became a reality. Also, she's extremely wise and somehow has a solution for every scenario (nobody tell her I said that).

While we can't choose our family, Granny (Goldie Avritte Sr.), mother (Renee Fraser), Grandfather (Allan Fraser), Auntie (Rhonda Norman), Grandma (Goldie Avritte Jr) deserve their spotlight for making me feel loved. To my sisters (Jacinda Whitley and Jasminda Whitley), I bare the heavy burden of being the best son (while I'm the only son) and I hope you choose a path that makes you happy whatever it may be.

To my friends, if you're reading this, you know how much I cherish the bonds I create. This section could be 20 pages long and I would still feel like there's so much that would be left unsaid. That's mainly why I had 20 slides of acknowledgements during the Defense and I still felt like I left out some important names. From my freshman physics class, undergraduate physics people, painting up crews, Central Spirit, intramurals, Summerhaven peeps, international friends, and weebs, y'all were fabulous in each and every way. While graduate school was my excuse to defer being a full adult with major bills and to be called Dr. JA (pronounced "jay" cause I play a lot of basketball), there were many people along the way that made this experience so much better. My sports people (Robert Benson Jr (BJ), Dr. Monaye Merritt, Dr. Morgan Smith, Trey Sawyers, Dr. Jade Kinney, Dr. Madison Hanks, Dr. Jerraco Johnson, Jonathan Walker, Imani Hill) fueled my competitive spirit and that was a huge benefit to my mental health. I rarely get to experience many black people in my field (or academia as a whole) and I'd like to thank the people of Black Graduate and Professional Student Associations (BGPSA), with Chloe Jones, Brian Cornish, Dr. Dwayne White, Dr. Aleah Horton, Dr. Shaniqua Williams, Dr. Erika Hanley, Dr. Chelsi Battle, and many more, for making this

experience fun with all the dancing, Taco Tuesdays, and hiking trips. Also, big shout-out to the previous cohort, including Dr. Lori Scott-McCabe and Nicholas Allen, for adopting me into their circle. Also, to the Party Cruu members Dr. Tiny, Dr. Curtis Johnson and Ali Fisher (may your bond be stronger than the fibers of a couch), Courtney (Centucky) and many more. Also, let me not forget the physics department staff who are the glue to the department, Mary Prater, Jennifer Morris, and G (Glenda Stroud).

Lastly, I'd like to thank the members of Jalaan's Illuminati. These are the people who have made it to the Mount Rushmore of Jalaan and their impact shall never be forgotten. Danielle Douglas, Kadisha Francois, Dr. Kirstie McTear, Kristyn Brandenburg, Yoland Howard, Aamir Patton, Dr. Stephen Williams, and Elon Price.

Dani could literally call me randomly at 1:25 pm, to go on a random errand or sit on the couch doing nothing for a few hours and that would be a fantastic day. Also, she's one of the first people that I knew that casually had snakes and she tried to teach me how to take care of them with frozen mice (I was definitely not nervous...).

Kadisha finds a way to put me on random things like Crazy Cazboys, Crumbl Cookies, unknown thrift stores. Every time she gets excited or recently comes back from Trinidad, her Trinidadian accent snaps back to reality and it's the eighth Wonder of the World that I'm never prepared for. Dr. McTear is a perfect storm to my storm. I will have random ideas for things and instead of being like "ummm.....", she'll immediately go "okay. I'm listening..". I never know what to expect when we get together. It's a truly stochastic behavior.

Kristyn Brandenburg is a woman who needs no introduction. She somehow finds ways to hit on the heart strings just right. We been through a lot and I'm glad she was one of my first friends at Clemson. No matter what happened, she would always found a way to advocate for me even at times when I didn't deserve it. It just something in the way she says "hey, buddy..." that it gets me every time.

Yolanda Howard and Aamir Patton should get their own paragraphs but they somehow seem to invoke the same emotions. I've known them both since high school, and they're some nerds but in a good way. They are my military nerds. They somehow know how to invoke my awkwardness in ways others can't. Yolanda had me trying out different charcuterie places

being fake boujee and had me in Germany with a broken foot going to an American food spot to eat the hottest wing flavor. Also, tell me how I met them at a ghost tour in Charleston and we basically had matching fits unplanned. It's spooky.

Dr. Stephen Williams is my ex...roommate. Even before that, he was one of the selling factors for me to come to Auburn outside of my advisor. The universe should never had let us meet. I remember one time Dr Williams was recalling him tell a story to someone and they stopped him and asked "Was Jalaan there" because it's that's usually where it all begins. I think he's going to miss me a lot because he's like "hear me out...you should move to Denver" now that he's got his big boy job.

Lastly, who could ever forget to mention Elon Price. Without her support, I probably would have never been able to finish this degree the way I did. All the time of me writing and focusing, I barely had time to think of eating or other major decisions. I would've been both homeless and starving most days if it wasn't for here. These last few months I used the excuse "Sorry, I'm writing a dissertation" more than I can count and now I have to come up with a new Get Out Of Jail Free Card. Overall, she pretty cool I guess.

Oh and huge honorable mentions to my furry nephews Castiel and Crowley. They're both precious and menaces at the same time. They will look at you with the most precious eyes ever but never should you ever leave any sort of bread-like food around them especially if it's in a plastic bag. They WILL find it!

Table of Contents

List of Figures

List of Tables

Chapter 1

Motivation

The majority, if not all, of the readers engaging with this dissertation are doing so through a computer, providing clear evidence of the entanglement of advanced technology into our daily lives. The utilization of advanced technology necessitates the development of corresponding advanced materials. Engineering these advanced materials underscores the significance of scientifically studying the fundamental physics principles that regulate properties of complex materials. An example of such fundamental material properties is thermal conductivity. It is probable that among the readership, at least one individual has encountered the predicament of a mobile phone or laptop overheating during the summer season. An issue that is directly attributable to materials failing to efficiently diffuse the heat generated from the circuits to the environment due to low thermal conductivity. The subsequent sections of this chapter will demonstrate the relevance of this atom-scale computational research within the broader scope of the physics of this material property.

1.1 Thermal Conductivity κ

Thermal conductivity κ measures a material's ability to allow (conductor) or resist (insulator) the flow of heat. κ, especially at elevated temperatures, is essential in many areas of physics:

1. Barrier coating [9]

2. Electric materials with an emphasis on renewable energy [22]

3. Potential materials for electronic devices like Boron Arsenide [53]

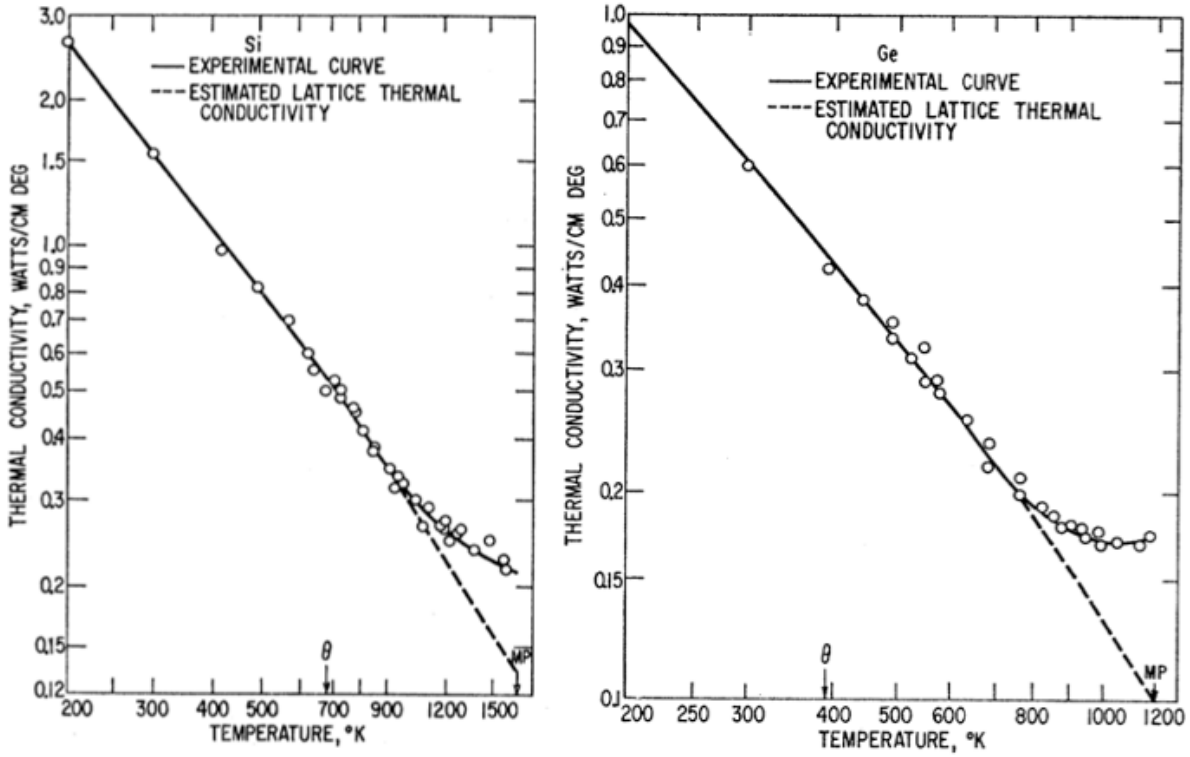

Figure 1.1: Experimentally measured thermal conductivity of (left) Silicon and (right) Germanium by Glassbrenner & Slack [17]. (dotted line) predicted κ_L by extrapolation. Debye (θ) and melting point (MP) temperatures are label.

4. Earth core and heat cycle [49]

κ is a macroscopic transport property that follows Fourier's Law :

$$\vec{J} = -\kappa \nabla T \tag{1.1}$$

in a material with a temperature gradient ∇T and heat flux $\vec{J}$. On a microscopic level, κ consists of a lattice contribution κ_L, from lattice vibrations (or phonons) and an electrical contribution κ_E, from electron/hole transport. The lattice thermal conductivity κ_L is the dominant term in solid insulators and semiconductors [2] with Silicon, a common material in microchips and electronics, being the focus of this work.

Harmonic behavior is governed by a restoring force (e.g. Hooke's law with spring motion) while anharmonicity (discussed in detail in Chapter 2) captures all the non-harmonic behavior and governs κ_L. A small perturbation of the lowest order anharmonicies, 3^{rd} order, leads to a $\kappa_L \propto \frac{1}{T}$ temperature (T) dependence at elevated temperatures (defined as perturbation theory in

this work). [10] However, this $\frac{1}{T}$ temperature dependence is not consistent with experimentally measured Silicon [16, 43, 17] (and Germanium) diamond lattice structures with Glassbrenner & Slack results [17] shown in Fig 1.1. While the electronic thermal conductivity κ_E was calculated in these measurements to account for some of the saturation, these κ_E calculations had uncertainties upwards of $\pm 20\%$ at the melting point. Two experimental equations to extrapolate κ_L (in W/(cm-K)) at all temperatures T are shown below[16, 17]:

$$\begin{aligned} \frac{1}{\kappa_L} &= 1.583 \times 10^{-6} T^2 + 1.532 \times 10^{-3} T + 0.1598 \\ \frac{1}{\kappa_L} &= 1.65 \times 10^{-6} T^2 + 1.56 \times 10^{-3} T + 0.03 \end{aligned} \tag{1.2}$$

With these equations also deviating from a $\frac{1}{T}$ prediction, a non-perturbative approach to the temperature dependence is needed to fully understand κ_L as higher order anharmonicity has shown to become non-negligible these temperatures [15, 14].

1.2 Theoretical Approaches

Two main theoretical approaches to thermal conductivity involve calculations utilizing quantum mechanics or classical dynamics. While quantum calculations will be the more accurate, the results should converge to those of classical dynamics above the Debye temperature. This Debye temperature, from the Debye model [11], establishes a temperature at which all the lattice vibrations are excited and the heat capacity, the heat required to change the temperature of a material by one degree, converges to a constant value. With the saturation and emphasis of κ_L well above the Debye temperature of Silicon, 640K [26], either a quantum or classical approach would suffice.

1.2.1 Quantum Accuracy

First principle (or ab-initio) calculations utilizes quantum mechanics and quantum chemistry by including electronic structures and interactions. The exact solution to an electronic system's

evolution $|\psi\rangle$ in time t can be solved with the Schrödinger equation:

$$H|\psi\rangle = (-\frac{\hbar^2}{2m}\nabla^2 + V_{total})|\psi\rangle = i\hbar\frac{\partial|\psi\rangle}{\partial t} \tag{1.3}$$

where H is the Hamiltonian defining the energy of the system, $\hbar$ is Planck's constant, m is the mass, ∇ is the derivative in space, and V_{total} is the total potential energy of all interactions. This becomes analytically and numerically impossible to solve for a many-body system as physics would have been mostly (if not fully) complete. As such, the commonly used Kohn-Sham density function theory (DFT) [29] reduces the many-body electron system Schrödinger equation to a single electron equation of motion:

$$H_{eff}|\psi\rangle = (-\frac{\hbar^2}{2m}\nabla^2 + V_{eff})|\psi\rangle = e_j|\psi_j\rangle \tag{1.4}$$

with an effective Hamiltonian H_{eff} based on an effective potential V_{eff} that requires an electron density. While DFT has quantum accuracy, it is limited to system sizes of 100s of atoms.

1.2.2 Classical Regime

Alternatively, molecular dynamics (MD) simulations (discussed in more detail in Chapter 3) solve for the evolution of a classical system in time t with a Newtonian equation of motion:

$$\vec{F} = \frac{d\vec{p}}{dt} \tag{1.5}$$

where $\vec{F}$ is the force and $\vec{p}$ is the momentum of particles. While MD simulations have been done utilizing DFT time evolution, it was limited in size to 100s of atoms and used a size extrapolation to converged the results [7]. Unfortunately, MD has a finite size effect, with a higher severity for non-equilibrium MD simulations [41], that contribute to the numerical uncertainty. Also, MD requires an inter-atomic potential (IAP), defining the atomic interactions or forces between the atoms. This varies the numerical accuracy depending on the potential model and demands over 100s of ensembles for reasonable convergence[18].

Empirical potentials, e.g. Tersoff[50], and Stillinger and Weber[45], use observed data to approximate the atomic system energies of different materials while recent machine-learning inter-atomic potentials (MLIAP), e.g. Gaussian Approximation Potential[3] (GAP) and Spectral Neighbor Analysis Potential (SNAP) [52], have being developed using DFT calculations and different kernel (basis) functions. Discussed in detail later, the GAP and SNAP potential both include quantum accuracy while the GAP potential has been shown to be more accurate in exchange for higher computational cost[57]. While thermal conductivity has been calculated MD using GAP [40], not much work has been done at elevated temperatures.

While lattice thermal conductivity is an intrinsic transport property that can be directly assessed using Non-Equilibrium Molecular Dynamics simulations (NEMD), it has been demonstrated that, for equivalent numerical convergence, NEMD typically necessitates significantly larger simulation models and/or longer simulation times than Equilibrium MD (EMD) simulations. Despite the substantial reduction in numerical load achieved through the development of accurate machine-learning interatomic potentials (MLIP), the computation of dynamical properties crucial for robustly modeling anharmonicity-regulated thermal transport processes remains computationally expensive, particularly for low-frequency and long-wavelength acoustic phonons. Consequently, in this study, we first focus on adopting systematic EMD simulations to capture the fluctuation and dissipation dynamics within a perfect yet anharmonic crystal. We then extrapolate non-equilibrium transport properties based on statistical transport theories.

In this study, two distinct types of EMD techniques have been employed. First, we utilize time auto-correlation functions (ACFs) of atomic displacement or velocity to investigate thermal excitations at the one-phonon level, i.e. within the phonon gas approximation. The primary outcomes of these EMD simulations include temperature-dependent renormalized phonon frequencies and phonon lifetimes. We conduct a comprehensive assessment of phonon modes throughout the entire Brillouin Zone in reciprocal q-space, employing finite q-sets that are commensurate with the employed supercell models. In principle, enlarging the size of MD simulation models allows us to sample a finer commensurate q-set, achieving numerical convergence. Notably, these phonon-based EMD simulations enable the isolation of specific contributions from individual phonon modes. However, a significant limitation lies in the adopted

approximation for the lattice heat flux at the Peierls' kinetic model of phonon heat currents. To address effects beyond the kinetic phonon models, a parallel EMD simulation is conducted for the ACF of lattice heat flux, employing an approximate Hardy's lattice model of heat flux. As a first step, we utilize a Taylor expansion of the anharmonic interatomic potentials based on atomic displacements. The atomic forces expressed in the Hardy's model are truncated at three levels: FC_2 only, FC_2+FC_3, and FC_2+FC_3+FC_4, where FC_2, FC_3, and FC_4 refer to the second-, third-, and fourth-order of force constant matrices.

The goal of this work is to use large scale MD simulations through the Large-scale Atomic/Molecular Massively Parallel Simulator (LAMMPS)[51] modeling program with the highly accurate GAP MLIAP to achieve the following: 1) reduce the numerical uncertainty of ordered systems (specifically Silicon) and 2) study high order anharmonicity at elevated temperatures with a non-perturbative temperature dependence for the study of lattice thermal conductivity.

1.3 Outline of Thesis

Fig 1.2 presents a visual overview of this dissertation, whose organizational structure is outlined as follows:

Chapter 2 consists of two parts. The initial part focuses on the computational methodologies utilized for computing harmonic and anharmonic phonon properties, incorporating damp harmonic oscillator theory and equilibrium molecular dynamics (MD) simulation. The subsequent part delves into the kinetic transport theory of phonons, explaining how the harmonic and anharmonic properties serve as the basis for defining microscopic heat fluxes in crystals. This includes the application of Peierls or Hardy formalism and the calculation of lattice thermal conductivity (κ_L) using the Boltzmann Transport Equation (BTE) or Green-Kubo theory.

Chapter 3 offers a comprehensive overview of the theoretical foundations underlying Non-Equilibrium MD (NEMD) and Equilibrium MD (EMD) simulations. Implementation details, particularly with the MD packages LAMMPS, and the adoption of machine-learning interatomic potentials (MLIAP), such as the GAP potential, are discussed.

Chapter 4 discusses some critical aspects of numeric algorithms developed in this dissertation research, for example q-space based algorithm for the reduction of numerical noise in

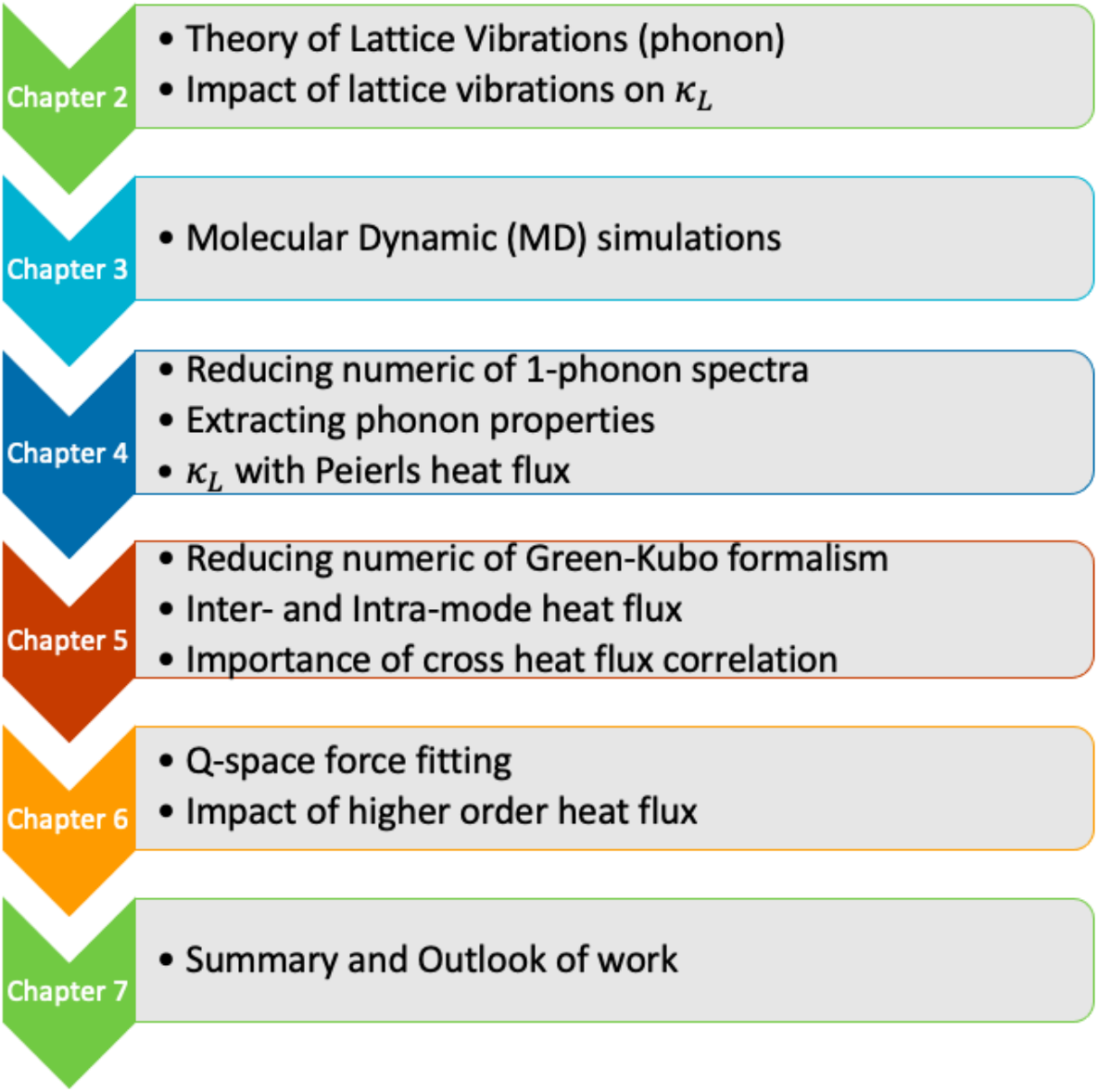

Figure 1.2: Outline of the rest of the chapters in this dissertation

1-phonon spectra, and a robust fitting algorithm for the calculations of renormalized phonon frequencies and lifetimes. The successes of the noise reduction in MD simulations and the enhanced robustness of the fitting algorithm justify the accuracy of the simulated phonon properties at elevated high-temperature conditions. The fitted spectra are subsequently employed to predict κ_L with the BTE, enabling a comparative analysis against perturbation theory and experimental findings.

Chapter 5 presents the simulation data beyond the kinetic phonon transport theory, with a focus to presenting an analytical solution aimed at improving the convergence of the Green-Kubo formalism. This chapter also delves into the individual contributions of the two distinct terms in second-order Hardy heat flux, i.e. the intra-model heat flux, which is comparable to the Peierl's heat flux in the kinetic phonon transport theory, and the inter-mode heat flux, which is omitted in the kinetic phonon transport theory. The numeric robustness of the data analysis reveals the significance of the cross-correlation between intra-mode and inter-mode heat fluxes. This is a crucial aspect largely overlooked in the existing theoretical literature.

Chapter 6 extends the discussion on the Hardy heat flux, exploring higher-order contributions and introducing an innovative approach involving temperature-dependent force constant matrices.

Finally, Chapter 7 provides a concise summary of the findings and suggests potential avenues for future research.

Chapter 2

Phonon Theory

This chapter serves as the theoretical framework of this work with emphasis on phonons and their application to the lattice thermal conductivity κ_L. While κ_L is inherently a non-equilibrium transport property, we show that κ_L can be calculated with equilibrium atomic dynamics (force, velocity, displacement). We begin with the Peierls' kinetic model of phonon heat currents. Then, we go beyond the Peierls heat flux with an approximate Hardy heat flux and showcase how we implemented mathematical techniques to project various orders of the approximate Hardy heat flux into q-space.

2.1 Lattice Vibrations and Phonons

At thermal equilibrium, atoms at the lattice sites will oscillate about an equilibrium point (shown later in this chapter). This movement is similar to that of a ball and spring model. With a model as shown in Fig 2.1, the normal modes define a basis of movement of a N-ball system with $1\times$N normal modes corresponding to the single degree of freedom in the x-direction. The entire system can be modeled as a superposition of these normal modes with an eigenvalue and eigenvector being the frequency of movement of the atoms and the direction of movement, respectively. When comparing phonons to the ball and spring model, phonons are quasi-particles representation of lattice vibrations. The dynamical properties of lattice vibrations can be modeled in terms of phonon dynamics with each phonon mode α characterized by its wave vector $\vec{q}$, oscillation frequency ω, and lifetime τ.

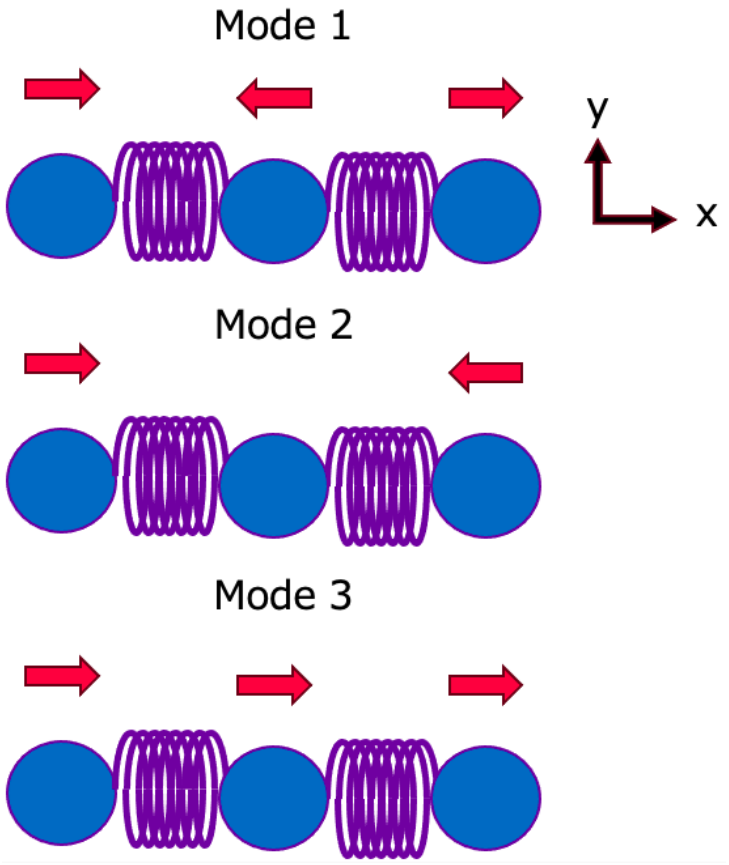

Figure 2.1: Normal modes of a 3-body ball and spring system restricted to movement in the x-direction

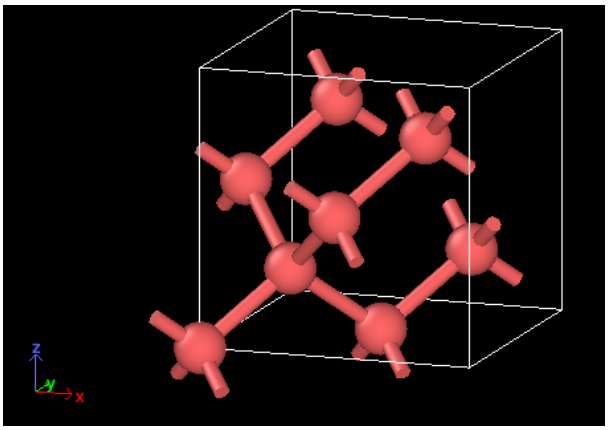

Figure 2.2: 8-atom diamond unit cell with nearest neighbor bonds visualized with OVITO [46]

2.2 Crystal Momentum in Reciprocal Space

Due to characterization with quantized frequencies, phonons are naturally represented in a frequency domain through reciprocal space. Perfect crystals with periodic lattices, e.g. diamond, clathrate, can utilize its real space periodicity to Fourier transform the basis from real-space to reciprocal space. The work in this dissertation focuses on the diamond lattice structure. Diamond is a face centered cubic (FCC) structure with a two basis atoms shown in Fig 2.2. The basis vectors of a diamond cell with lattice length,L, in real-space can be conventional cubic in the x,y,z:

$$\begin{aligned} \vec{a}_1' &= L(\hat{x}) \\ \vec{a}_2' &= L(\hat{y}) \\ \vec{a}_3' &= L(\hat{z}) \end{aligned} \tag{2.1}$$

where $\hat{x}$ is a unit distance in the x-direction or primitive unit vectors:

$$\begin{aligned} \vec{a}_1 &= \frac{L}{2}(\hat{y} + \hat{z}) \\ \vec{a}_2 &= \frac{L}{2}(\hat{x} + \hat{z}) \\ \vec{a}_3 &= \frac{L}{2}(\hat{x} + \hat{y}) \end{aligned} \tag{2.2}$$

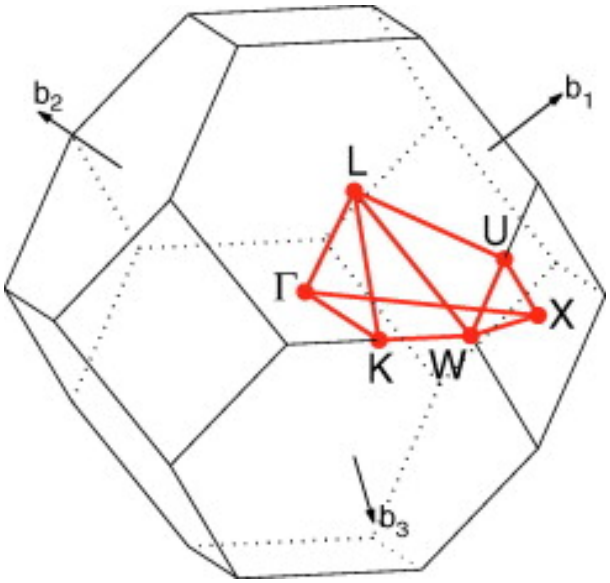

Figure 2.3: Brillioun zone of a FCC/Diamond lattice labeled with high symmetry points [42]

,which is the smallest vectors that can represent a cell. Due to the periodicity of an FCC cell, a translation of one unit vector in any direction from one atom will overlap with another atom. Bisecting all first nearest neighbor atoms makes a reciprocal unit cell, or Brillouin zone, with basis vectors:

$$\begin{pmatrix} \vec{b}_1 \\ \vec{b}_2 \\ \vec{b}_3 \end{pmatrix} = \frac{2\pi}{V} \begin{pmatrix} \vec{a}_2 \times \vec{a}_3 \\ \vec{a}_3 \times \vec{a}_1 \\ \vec{a}_1 \times \vec{a}_2 \end{pmatrix} \tag{2.3}$$

with volume, $V = |\vec{a}_1 \cdot (\vec{a}_2 \times \vec{a}_3)| = |\vec{a}_2 \cdot (\vec{a}_3 \times \vec{a}_1)| = |\vec{a}_3 \cdot (\vec{a}_1 \times \vec{a}_2)|$. By definition, the Brillouin zone has a periodic boundary with vectors of units of frequency called q-points where a translation of $\vec{G}$, an integer number in reciprocal lattice units, yields $\vec{Q} = \vec{q} + \vec{G} = \vec{q}$. The q-point boundaries of the Brillouin zone range from (-0.5,0.5], where either 0.5 or -0.5 is used but not both due to periodicity. The FCC Brillouin zone shown in 2.3 has various high symmetry q-points like Γ-point, which is the zone center point and L-point, which is a zone boundary point. q-points have other q-points equivalent to it by either rotation in reciprocal space or a translation of $\vec{G}$ beyond the boundary of the Brillouin zone.

All equivalent q-points are expected to have the same properties and phonon information for each mode. This makes it ideal to convert certain properties to reciprocal space by folding

atoms with translational symmetry to the basis atoms. This folding will decompose the N atom system of 3N modes to a set of q-points where each q-point has 3 $\times$ (# of basis atoms) modes, which totals to 6 modes per q-point in diamond.

2.3 Harmonic and Anharmonic Forces

Crystal dynamics can be categorized by harmonic and anharmonic behavior. Harmonic behavior describes motions controlled by a restoring force, F,:

$$F = -kx \tag{2.4}$$

where x is the displacement from equilibrium and k is a spring constant. The stronger the spring constant, the larger the force pulling the object back to equilibrium. The potential energy, U, for harmonic motion quantifies the amount of energy the storied by the system that can potentially move the object:

$$U = \frac{1}{2}kx^2 \tag{2.5}$$

For the system to be stable and oscillating about an equilibrium point, the potential must be at a local minimum. A realistic system will not be perfectly harmonic and deviations from this quadratic potential gives rise to anharmonic forces. As seen in Fig 2.4, higher order potential terms provides more terms to accurately capture the complexity of the system and oscillation about equilibrium. Without the inclusion of dissipative forces, the force is conserved (no net change in energy over a closed loop) which results in $F = -\nabla U = -\sum_i \sum_I \frac{\partial U}{\partial u_i^I}$, where I represents the Cartesian directions, x, y, z , and u_i is the displacement of the i^{th} atom from equilibrium. A Taylor expansion, or polynomial expansion, of U about an equilibrium position r_{eq} gives:

$$\begin{aligned} U = U(r_{eq}) + \sum_i \sum_I \frac{\partial U}{\partial u_i^I} u_i^I + \frac{1}{2!} \sum_{i,j} \sum_{I,J} \frac{\partial^2 U}{\partial u_i^I \partial u_j^J} u_i^I u_j^J \\ + \frac{1}{3!} \sum_{i,j,k} \sum_{I,J,K} \frac{\partial^3 U}{\partial u_i^I \partial u_j^J \partial u_k^K} u_i^I u_j^J u_k^K + \frac{1}{4!} \sum_{i,j,k,l} \sum_{I,J,K,L} \frac{\partial^4 U}{\partial u_i^I \partial u_j^J \partial u_k^K \partial u_l^L} u_i^I u_j^J u_k^K u_l^L + ... \end{aligned} \tag{2.6}$$

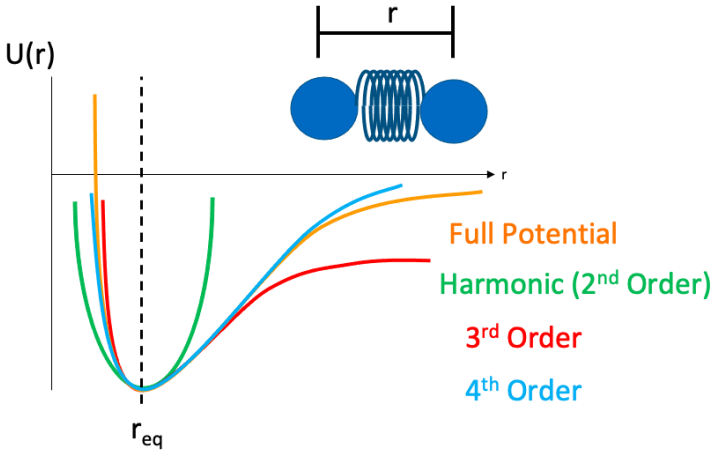

Figure 2.4: Decomposition of a generic potential energy between two atoms to the harmonic approximation, 3^{rd} order, and 4^{th} order approximation

where $\frac{\partial^2 U}{\partial u_i^I \partial u_j^J}$, $\frac{\partial^3 U}{\partial u_i^I \partial u_j^J \partial u_k^K}$, and $\frac{\partial^4 U}{\partial u_i^I \partial u_j^J \partial u_k^K \partial u_l^L}$ are called the 2^{nd}, 3^{rd}, and 4^{th} order force constants (FC) matrices, respectively. Bare phonon FC matrices are FC matrices calculated independent of the system temperature while renormalized phonons FC matrices account for the system temperature. From the 'Full Potential' curve in Fig 2.4 , it can be shown that the 1^{st} order force term, $\frac{\partial U}{\partial u_i^I}$, must be zero since the slope is zero at r_{eq}. The term with the 2^{nd} force constants (FC^2) is the harmonic term while all other higher order terms are anharmonic terms. Typically, the FC^4 or FC^3 terms are the highest order anharmonicity considered and the rest are truncated due to the computational intensity of those calculation (cite some examples maybe). Another "trick" (that will be discussed later) involved folding higher order terms to even (2^{nd} and/or 4^{th}) and odd (3^{rd}) terms.

A FC^2 matrix define a matrices of spring constants, $FC^2_{ij} = \left(k_{ij}\right)$ between the i^{th} atom and the j^{th} atom. Dividing by the mass creates a dynamical matrix, D :

$$\begin{aligned} D_{ij} &= \left(\frac{k_{ij}}{\sqrt{m_i}\sqrt{m_j}}\right) \\ &= \left(\omega_{ij}^2\right) \end{aligned} \tag{2.7}$$

where the frequency $w = \sqrt{\frac{k}{m}}$. $D_{ij}(l_i, l_j)$ represents D_{ij} as a function of the equilibrium distance between atom i to the origin and atom j to the origin. Any point can be the reference

point and using atom i as the reference point yields an invariant D_{ij}:

$$D_{ij}(\vec{l_i}, \vec{l_j}) = D_{ij}(0, \vec{h}) \tag{2.8}$$

where $h = l_j - l_i$. This invariance makes D easy to fold to reciprocal space at q-points, $\vec{q_1}$ and $\vec{q_2}$:

$$\begin{aligned} D_{i'j'}(\vec{q_1}, \vec{q_2}) &\equiv \sum_h \sum_{l_i} D(0, \vec{h}) e^{i\vec{l_1}\cdot(\vec{q_1}+\vec{q_2})} e^{i\vec{q_1}\cdot\vec{r_{i'}}} e^{i\vec{q_2}\cdot(\vec{r_{j'}}+\vec{h})} \\ &= \sum_h D(0, \vec{h}) e^{i(\vec{q_2}\cdot(\vec{r_{j'}}+\vec{h})+\vec{q_1}\cdot\vec{r_{i'}})} \sum_{l_i} e^{i\vec{l_1}\cdot(\vec{q_1}+\vec{q_2})} \end{aligned} \tag{2.9}$$

where i' and j' are the basis atom indices, and $\vec{r_{i'}}$ and $\vec{r_{j'}}$ are the equilibrium distance of the basis atoms to the origin. The $\sum_{l_i}$ term reduces to:

$$\sum_{l_i} e^{i\vec{l_1}\cdot(\vec{q_1}+\vec{q_2})} = N\Delta(\vec{q_1} + \vec{q_2}) \tag{2.10}$$

where N is the total q-points of the system. This leads to the selection rule, for 2 q-points, restricting the allowed values of $\vec{q_1}$ and $\vec{q_2}$:

$$\vec{q_1} + \vec{q_2} = \vec{G} \tag{2.11}$$

Since a single $\vec{q}$ ranges from (-0.5,0.5], the only way for Eq 2.11 to remain valid is for $\vec{G} = 0$ thus, $\vec{q_1} = -\vec{q_2} = \vec{q}$. Combining the implications of Eq 2.11 to Eq **??** gives:

$$\begin{aligned} D_{i'j'}(\vec{q}) &= m \sum_h D_{ij}(0, \vec{h}) e^{i\vec{q}\cdot(\vec{r_j}+\vec{h}-\vec{r_j})} \\ &\approx \sum_h D_{ij}(0, \vec{h}) e^{i\vec{q}\cdot(\vec{r_j}+\vec{h}-\vec{r_j})} \end{aligned} \tag{2.12}$$

The total modes m can be dropped if $D_{i'j'}(\vec{q})$ is normalized per q-point. For a diamond lattice, $D_{i'j'}(\vec{q})$ will always be a square matrix of shape (6,6) that makes it a unique indicator for comparing different system sizes. Also, the phonon characteristics, ω^α and $\vec{v_g^\alpha}$, can be calculated

by finding the eigenvalues and eigenvectors of $D_{i'j'}(\vec{q})$. The eigenvalues λ and eigenvectors $\vec{e_\lambda}$ are coupled parameters of a linear transformation:

$$A\vec{e_\lambda} = \lambda\vec{e_\lambda} \tag{2.13}$$

that extracts the normal mode vectors and frequencies from a square matrix A of shape $n \times n$. Moving the terms of Eq 2.13 to the left side and factoring out $\vec{e_\lambda}$ gives:

$$(A - \lambda I)\vec{e_\lambda} = 0 \tag{2.14}$$

where I is the identity matrix with diagonal elements of 1 and all off diagonals elements of 0. A Kronecker delta:

$$\delta_{ij} \equiv \begin{cases} 1 & if \quad i = j \\ \\ 0 & elsewhere \end{cases} \tag{2.15}$$

is another representation of the identity matrix that will be used later on. Eq 2.14 implies:

$$\left| A - \lambda\delta_{ij} \right| = 0 \tag{2.16}$$

where $||$ is the determinant of a matrix. From Cramer's rules in linear algebra, the determinant solves a system of equation if the matrix is a matrix of coefficients like Eq 2.16. This will give a list of eigenvalues λ_n corresponding to the shape of A. $D_{i'j'}(\vec{q})$ is a coefficient matrix of square frequencies ω^2 so $\sqrt{\lambda_\alpha} = \omega_\alpha$ and $\omega_\alpha > 0$ for the phonon modes α. Plugging each individual λ_α into Eq 2.14 and solving for $\vec{e_\lambda}$, gives a unique $\vec{e_{\lambda,\alpha}}$ for each phonon mode.

Phonopy, an open-source phonon calculation package [54], illustrates how $\vec{e_\lambda}$, ω_α, and $D_{i'j'}(\vec{q})$ can derive the group velocity $\vec{v_{g_\alpha}} = \frac{\partial\omega_\alpha}{\partial\vec{q}}$. The chain rule for derivatives:

$$\frac{\partial f(g(\vec{q}))}{\partial\vec{q}} = \frac{\partial f(\vec{q})}{\partial\vec{q}}\frac{\partial g(\vec{q})}{\partial\vec{q}} \tag{2.17}$$

where f and g are a function of $\vec{q}$. For a square function like ω_α^2, the derivative with respect to $\vec{q}$ is:

$$\frac{\partial \omega_\alpha^2}{\partial \vec{q}} = 2\omega_\alpha \frac{\partial \omega_\alpha}{\partial \vec{q}} \tag{2.18}$$

Rearranging Eq 2.18 and applying it to the definition of group velocity gives:

$$\begin{aligned} \vec{v_{g}}_\alpha &= \frac{\partial \omega_\alpha}{\partial \vec{q}} \\ &= \frac{1}{2\omega_\alpha} \frac{\partial \omega_\alpha^2}{\partial \vec{q}} \end{aligned} \tag{2.19}$$

The derivative of $D_{i'j'}(\vec{q})$, as defined by Eq 2.12, with respect to $\vec{q}$ using the chain rule is:

$$\frac{\partial D_{i'j'}(\vec{q})}{\partial \vec{q}} = \sum_h i(\vec{r_j} + \vec{h} - \vec{r_j}) D_{ij}(0, \vec{h}) e^{i\vec{q}\cdot(\vec{r_j}+\vec{h}-\vec{r_j})} \tag{2.20}$$

Building a square matrix η_α, with columns being $\vec{e_{\lambda,\alpha}}$, creates a change of basis matrix that transforms a matrix or vector from one basis to the normal mode basis. For $D_{i'j'}(\vec{q})$, this transformation gives:

$$\eta_\alpha^\dagger D_{i'j'}(\vec{q}) \eta_\alpha = \omega_\alpha^2 \tag{2.21}$$

where † is the conjugate transpose of a matrix and the derivative becomes:

$$\begin{aligned} \frac{\partial \eta_\alpha^\dagger D_{i'j'}(\vec{q}) \eta_\alpha}{\partial \vec{q}} &= \frac{\partial \omega_\alpha}{\partial \vec{q}} \\ \eta_\alpha^\dagger \frac{\partial D_{i'j'}(\vec{q})}{\partial \vec{q}} \eta_\alpha &= \frac{\partial \omega_\alpha}{\partial \vec{q}} \end{aligned} \tag{2.22}$$

Combining Eq 2.22 and Eq 2.23 an equation for the group velocity:

$$\vec{v_{g}}_\alpha = \frac{1}{2\omega_\alpha} \eta_\alpha^\dagger \frac{\partial D_{i'j'}(\vec{q})}{\partial \vec{q}} \eta_\alpha \tag{2.23}$$

,which can be entirely computed from a dynamical matrix.

2.4 Phonon-Phonon Scattering

Phonon-phonon scattering occurs when phonons transition from an initial state $|i\rangle$ to a final state $|f\rangle$ with energies E_i and E_f, respectively, based on a probability distribution. Other scattering mechanisms occur in a lattice, i.e. phonon-electron and phonon-defect, but phonon-phonon scattering are the dominant mechanism in lattice thermal conductivity and the focus of this dissertation. Multiple scattering rates τ combine by Matthiessen's rule:

$$\frac{1}{\tau_{total}} = \frac{1}{\tau_{phonon}} + \frac{1}{\tau_{defect}} + \frac{1}{\tau_{electron}} + ... \tag{2.24}$$

From this point, phonon-phonon scattering will be referred to as phonon scattering unless specified otherwise. In the harmonic approximation, phonons will never scatter because the oscillation never changes in time. This means all phonon scattering is due to anharmonic behavior with the lowest order being 3^{rd}. Using a first-order perturbation, Fermi's golden rule defines the scattering rate $S_{i\to f}$:

$$\begin{aligned} S_{i\to f} &= \frac{2\pi}{\hbar}|\langle f|\Delta\hat{V}|i\rangle|^2\delta(E_i - E_f) \\ &= \frac{2\pi}{\hbar}|\langle f|\Delta\hat{V}|i\rangle|^2\delta_{E_i,E_f} \end{aligned} \tag{2.25}$$

where $\Delta\hat{V}$ is the difference between the full potential energy and harmonic term, and $\hbar$ is Planck's constant. The delta function δ_{E_i,E_f} in Eq 2.25 implies the transitions must conserve energy since $\delta_{E_i,E_f} = 0$ unless $E_f = E_i$, where the energy of a phonon mode is $E_\alpha = \hbar\omega_\alpha$.

Similar to conservation of momentum, phonons scatter one of two ways: (1) one mode splitting into multiple modes, or (2) multiple modes combining to a single mode. 3-phonon scatter involves scattering involving 3 separate modes, 4-phonon scattering involves 4 separate modes, etc as shown in Fig 2.5 a). When a phonon scatters the second way by combining, the resulting mode can sometimes be larger than the boundary of the reciprocal lattice. This resultant mode can be folded back to the reciprocal boundary by a $\vec{G}$ translation. This folding along with conservation of energy gives the governing conservation constraints for 3-phonon

scattering:

$$Method\ 1: \begin{cases} \hbar\vec{q}_\alpha &= \hbar\vec{q}_\beta + \hbar\vec{q}_\beta \\ \hbar\vec{\omega}_\alpha &= \hbar\vec{\omega}_\beta + \hbar\vec{\omega}_\beta \end{cases} \tag{2.26}$$

$$Method\ 2: \begin{cases} \hbar\vec{q}_\beta + \hbar\vec{q}_\beta &= \hbar\vec{q}_\alpha + \hbar\vec{G} \\ \hbar\vec{\omega}_\beta + \hbar\vec{\omega}_\beta &= \hbar\vec{\omega}_\alpha \end{cases} \tag{2.27}$$

where the momentum of a phonon mode is $\hbar\vec{q}$. By factoring the $\hbar$ out of Eq 2.26 and Eq 2.27, the conservation constraints reduce to:

$$Method\ 1: \begin{cases} \vec{q}_\alpha &= \vec{q}_\beta + \vec{q}_\beta \\ \vec{\omega}_\alpha &= \vec{\omega}_\beta + \vec{\omega}_\beta \end{cases} \tag{2.28}$$

$$Method\ 2: \begin{cases} \vec{q}_\beta + \vec{q}_\beta &= \vec{q}_\alpha + \vec{G} \\ \vec{\omega}_\beta + \vec{\omega}_\beta &= \vec{\omega}_\alpha \end{cases} \tag{2.29}$$

When $\vec{G} = 0$, this is called a Normal process scattering (or N-process). N-process scatterings conserve both energy and momentum. When $\vec{G} \neq 0$, this is called an Umklapp process scattering (U-process). The resultant mode of an U-process is folded by into the reciprocal lattice and becomes inverted as shown in Fig 2.5. This flipping of the mode causes momentum not to be conserved as the resultant mode will be in the opposite direction of combined modes in at least one direction. This is a consequence of the translational invariance of the reciprocal lattice due to the Fourier transformation and it is important to note that crystal momentum is not equal to real space momentum.

While not computationally impossible, accounting for all possible scattering arrangements ($3-^+$ phonon) would require an immense amount of computer resources for even a small crystal. Typically, only 3-phonon (and sometimes 4-) scatterings are computed. ShengBTE and phono3py utilize symmetry and other operations to compute 3-phonon scattering with only

bare phonon FC^2 and FC^3 [31, 54]. FourPhonon calculates 4-phonon scattering by using expanding upon ShengBTE's 3-phonon methodology [20]. Due to only using the bare phonon, these rely on perturbation theory as a predictor for higher temperatures.

2.5 Phonon Gas Model

The phonon gas model (PGM) treats the behavior of complex anharmonic lattice vibration as that of a gas consisting of weakly interacting phonons, which travels at their group velocities over some distance (mean free path) without any scattering. This gives rise to a more intuitive understanding of phonon group velocity as the speed of the phonon modes. Unfortunately, a highly disordered material like amorphous glass has no rigorous definition of phonon velocities in these modes and invalidates the phonon gas model [32].

The theoretical foundation of the PGM is that the Hamiltonian (or total energy of system) of an anharmonic lattice can be described as:

$$H = H_0 + H' \tag{2.30}$$

where H_0 is the Hamiltonian of non-interacting (bare) phonons and H' encompasses the interactions among bare phonons. H_0 will be a summation of harmonic oscillators (HO) of the form:

$$H_{HO} = \frac{p^2}{2m} + \frac{m\omega^2 x^2}{2} \tag{2.31}$$

with momentum p, mass m, displacement x, and frequency ω. The perturbation can be approximated to the anharmonic potential terms if the anharmonic potential is sufficiently smaller than the harmonic potential term. A Green's function corresponds to the propagation of an impulse or shock through a system in a given time interval. Thus, the 1-phonon Green's function $G_q(\omega)$ can be seen as the response of a system to a single-phonon propagation with momentum $\hbar\vec{q}$ and energy $\hbar\omega$. The Dyson equation:

$$G_q(\omega)^{-1} = G_q^0(\omega)^{-1} - \Sigma_q(\omega) \tag{2.32}$$

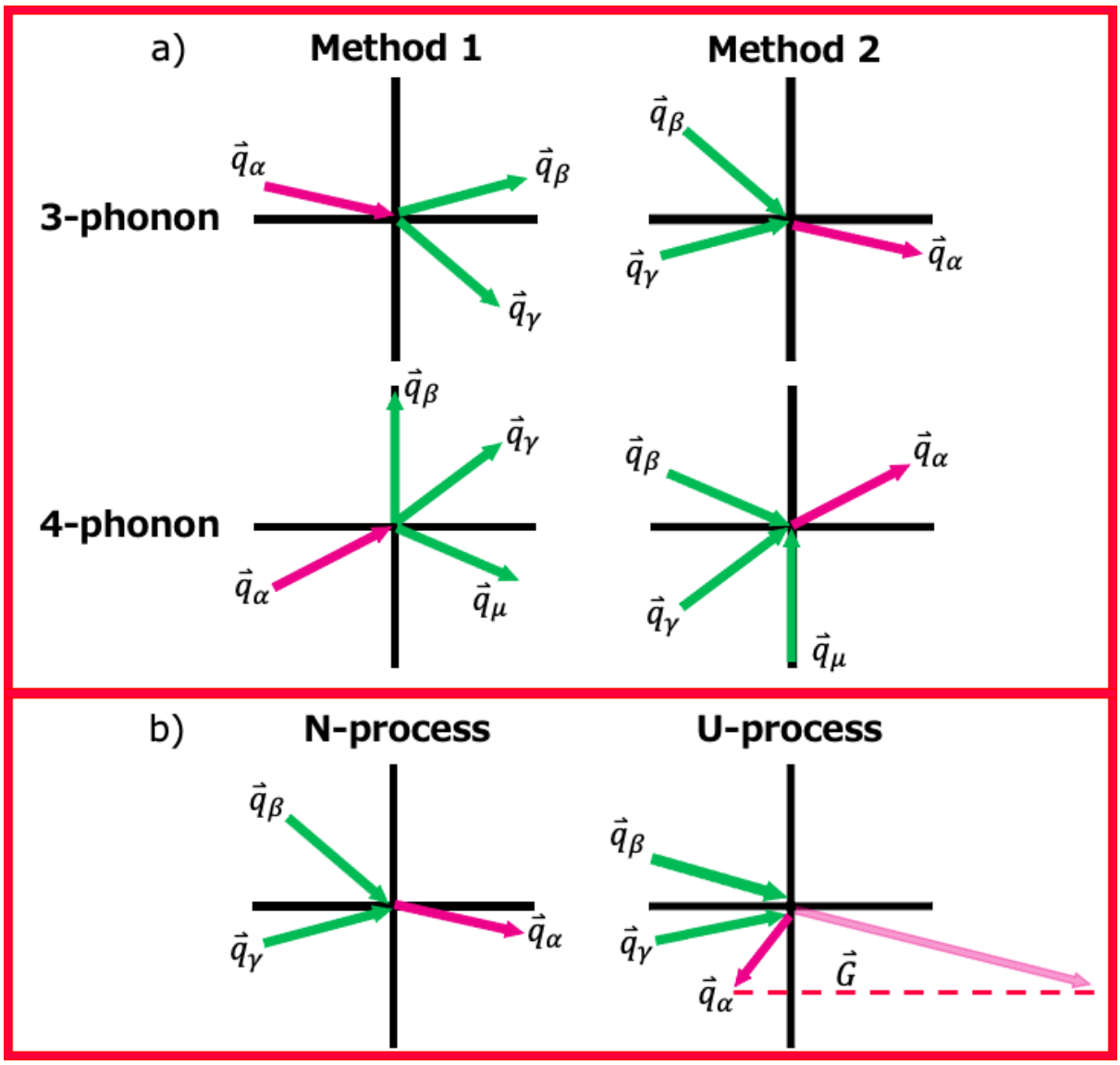

Figure 2.5: Different methods of scattering for a) 3-phonon and 4-phonon interactions and b) types of processes for phonon combination

gives the relation of the 1-phonon Green's function, Green's function from the non-interacting Hamiltonian, and self energy Σ. The self-energy defines the anharmonic phonon interactions that can be represented with Feynman diagrams. With weakly interacting phonons and $\hbar\omega_q \gg |\Sigma_q(\omega_q, T)|$, the temperature dependent frequency shifts $\Delta_q(T)$ and broadening $\Gamma_q(T)$ are:

$$\begin{aligned} \Delta_q &= \text{Re}(\Sigma_q(\omega_q)) \\ \Gamma_q &= \text{Im}(\Sigma_q(\omega_q)) \end{aligned} \tag{2.33}$$

where Re and Im are the real and imaginary components, respectively. With the non-interacting Green's function $G_q^0(\omega)$ as:

$$G_q^0(\omega) = \frac{2\omega_0}{\omega^2 - \omega_0^2} \tag{2.34}$$

then $G_q(\omega)$, based on Eq 2.35, becomes:

$$G_q(\omega) = \frac{2\omega_0}{\omega^2 - \omega_0^2 - 2\omega_0\Sigma(\omega, T)} \tag{2.35}$$

The phonon spectra $A_q(\omega, T)$ defines the probability of finding a particle with energy $\hbar\omega$ and momentum $\hbar\vec{q}$, at a temperature T:

$$A_q(\omega, T) = -\frac{1}{\pi}\text{Im}(G_q(\omega)) \tag{2.36}$$

Expanding $\Sigma(\omega, T) = (\Delta(\omega) + i\Gamma(\omega))$ and taking the imaginary component, Eq 2.35 becomes to:

$$A_q(\omega, T) = -\frac{1}{\pi}\frac{2\omega^2\Gamma}{(\omega^2 - \Omega_0^2)^2 + 4\omega^2\Gamma^2} \tag{2.37}$$

where $\Omega_0(T) = \omega_0 + \Delta(T)$ is the renormalized frequency and $\Omega_0^2 = \omega_0^2 - \Delta^2 - 2\omega_0\Delta \approx \omega_0^2 - 2\omega_0\Delta$ given $\omega \gg \Delta$. Treating w a constant, the Taylor series expansion of $(\omega^2 - \Omega_0^2)^2$ as Ω_0 approaches ω is $4\omega^2(\Omega_0 - \omega)^2 = 4\omega^2(\omega - \Omega_0)^2$. Combining the Taylor series expansion to Eq 2.37 and factoring out a ω^2, the 1-phonon spectrum:

$$A_q(\omega, T) = -\frac{1}{2\pi}\frac{\Gamma}{(\omega - \Omega_0)^2 + \Gamma^2} \tag{2.38}$$

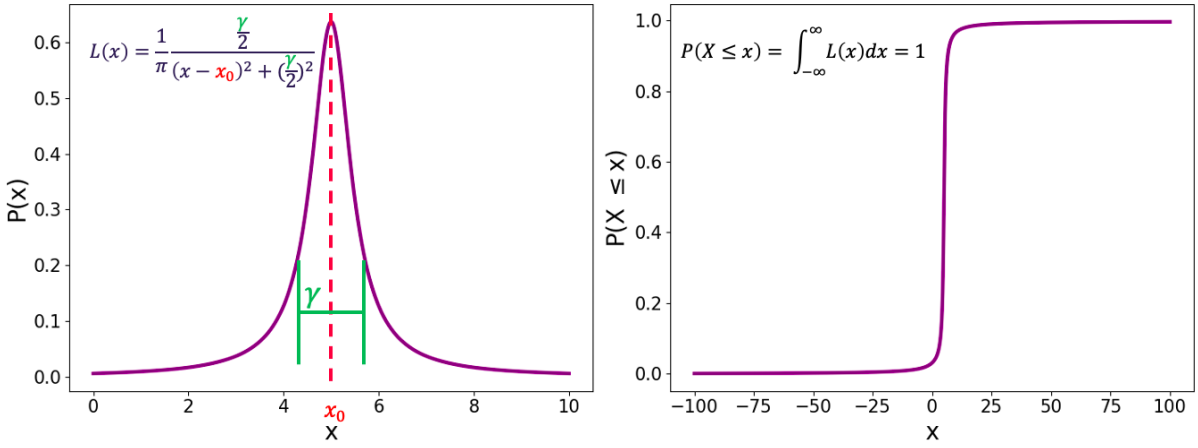

Figure 2.6: (left) Lorentzian distribution function and (right) the integral over all space

has the form of a Lorentzian function, shown in Fig 2.6,:

$$\begin{aligned} L(x) &= \frac{1}{\pi}\frac{\frac{1}{2}\gamma}{(x-x_0)^2+(\frac{1}{2}\gamma)^2} \\ P(X \leq x) &= \int_{-\infty}^{\infty} L(x)dx = 1 \end{aligned} \tag{2.39}$$

centered at the renormalized frequency location $\Omega_0(T)$ and broadening $2\Gamma(T)$. γ defines the full width half maximum (FWHM) of the Lorentzian function, which is double the broadening Γ. The phonon lifetime τ is inversely proportional to the FWHM such that:

$$\tau = \frac{1}{2\Gamma} \tag{2.40}$$

This means the temperature-dependent frequency, and phonon lifetime can be extracted from the 1-phonon spectra. The full $A_q(\omega, T)$ will not be perfectly Lorentzian and the deviations from the ideal Lorentzian fit gives insights to 3^+-phonon scattering.

Experimentally, the phonon spectrum has been observed by Raman spectroscopy and inelastic neutron scattering (INS) [34, 55, 5]. Both methods vibrate the nucleus of a crystal by

energizing the nucleus with either photons (Raman) or neutrons (INS), then measure the structure factor S:

$$S(\vec{q},\omega) = \frac{1}{2\pi}\sum_{ll'} e^{-i\vec{q}\cdot(\vec{x}(l)-\vec{x}(l'))}\int_{-\infty}^{\infty} e^{i\omega t}\langle e^{-i\vec{q}\cdot\vec{u}(l,t)}|e^{i\vec{q}\cdot\vec{u}(l',0)}\rangle dt \tag{2.41}$$

where $\vec{u}$ is the displacement of atom about the equilibrium position $\vec{x}(l)$ and $\langle|\rangle$ denotes the auto-correlation function (ACF). The ACF defines the similarity of a random process f with itself in τ for a continuous case:

$$C(\tau) = \int_{-\infty}^{\infty} f(t+\tau)f^*(t)dt \tag{2.42}$$

or discrete case:

$$C(\tau) = \sum_{n} f(n+\tau)f^*(n) \tag{2.43}$$

where $f^*(t)$ is the complex conjugate of $f(t)$.

This structure factor describes how a material scatters based on an interference pattern and can be seen as mirroring the phonon spectrum. Raman spectroscopy uses photons to scatter the nucleus. This leads to issues of measurement due to the electron interactions which limits the measurements to the zone-center point (Γ-point). The restriction on the q-point resolution has made INS data more appealing for a full Brillouin zone analysis. By firing the nucleus with neutral atoms, the phonon-electron and other scattering mechanisms are undisturbed. Unfortunately, INS measurements are expensive calculations since they require neutron collisions, utilize a large facility to run, and highly sensitive to instrument resolution. Regardless, recent INS data has provided new avenues to study the phonon spectrum [28]. A Taylor series expansion of Eq 2.41 to the first order is the 1-phonon spectrum:

$$S(\vec{q},\omega) = \frac{e^{-2W}}{2\pi}\frac{1}{2\pi}\sum_{ll'} e^{-i\vec{q}\cdot(\vec{x}(l)-\vec{x}(l'))}\int_{-\infty}^{\infty} e^{i\omega t}\langle\vec{q}\cdot\vec{u}(l,t)\ \vec{q}\cdot\vec{u}(l',0)\rangle \tag{2.44}$$

where W represents the Debeye-Waller factor. The 1-phonon approximation scales linearly with $\vec{q}$. This allows for q-points to be sampled outside the first Brillouin zone to be folded back to inside the reciprocal lattice.

A third approach to finding the 1-phonon spectrum is by approximating the phonon modes as non-interacting damped harmonic oscillators (DHO). The non-interacting Hamiltonian $\hat{H}$:

$$\hat{H} = \frac{\hat{p}^2}{2m} + \frac{1}{2}m\omega^2\hat{x}^2 \tag{2.45}$$

is the addition of the kinetic energy with a momentum operator $\hat{p}$ and potential energy with position operator $\hat{x}$. $\hat{H}$ results in discrete energy values E_n such that:

$$\begin{aligned} E_n &= \hbar\omega(n + \frac{1}{2}) \\ n &= 0, 1, 2, 3, ... \end{aligned} \tag{2.46}$$

An annihilation $a^\dagger$ and creation a operator:

$$\begin{aligned} a^\dagger|n\rangle = E_{n-1}|n\rangle = \hbar\omega(n - 1 + \frac{1}{2})|n\rangle \\ a|n\rangle = E_{n+1}|n\rangle = \hbar\omega(n + 1 + \frac{1}{2})|n\rangle \end{aligned} \tag{2.47}$$

of a state $|n\rangle$ lowers and raises, respectively, the energy E_n by one stage. When the position operator $\hat{x}$ is written in terms of the raising and lower operators:

$$\hat{x} = \sqrt{\frac{\hbar}{2m\omega}}(a^\dagger + a) \tag{2.48}$$

then the non-interacting, 1-phonon Green's function under the DHO approximation becomes:

$$G_q^0 \propto i\langle\hat{x}(\omega, t)\hat{x}^*(\omega, 0)\rangle \tag{2.49}$$

which leads to the 1-phonon spectrum A_q^0 as:

$$A_q^0 = -\frac{1}{\pi}\text{Im}(G_q^0) \propto -\frac{1}{\pi}\text{Re}(\langle\hat{x}(\omega, t)|\hat{x}^*(\omega, 0)\rangle) \tag{2.50}$$

Only the real part of the Fourier transformation of the displacement's ACF needs to be evaluated to get the 1-phonon Green's function in the classical regime.

The particles, with position $\hat{x}$ and momentum $\hat{p}$, can be treated as moving in the presence of a fluid-like random force ξ. This system is modeled with a Langevin equation of motion:

$$\begin{aligned} \frac{dQ(t)}{dt} &= P(t) \\ \frac{dP(t)}{dt} &= -\Omega_0^2 Q(t) - 2\Gamma P(t) + \xi(t) \end{aligned} \tag{2.51}$$

where Ω is a characteristic frequency, Γ is the positive non-zero damping constant, and Q and P are a transformation:

$$\begin{aligned} Q &= \left(\frac{\hbar}{m\omega}\right)^{-1/2} \hat{x} \\ P &= \left(m\omega\hbar\right)^{-1/2} \hat{p} \end{aligned} \tag{2.52}$$

By letting $X(t)$ represent the correlation of Q with itself in time, $\langle Q(t)|Q(0)\rangle$ with $t \geq 0$, multiplying by $Q(0)$, and taking the correlation, then Eq 2.51 can be rewritten as:

$$\begin{aligned} \frac{dX(t)}{dt} &= \langle P(t)|Q(0)\rangle \\ \frac{d^2X(t)}{dt^2} &= -\Omega_0^2 X(t) - 2\Gamma\frac{dX(t)}{dt} + \langle \xi(t)|Q(0)\rangle \end{aligned} \tag{2.53}$$

$\xi(t)$ is random in time such that it has no correlation with $Q(0)$ (or $\langle \xi(t)|Q(0)\rangle = 0$). Therefore, Eq 2.53 reduces to:

$$\frac{d^2X(t)}{dt^2} = -\Omega_0^2 X(t) - 2\Gamma\frac{dX(t)}{dt} \tag{2.54}$$

Eq 2.54 has the solution of a harmonic oscillator. In the under-damped condition $\Omega_0 > \Gamma$, a harmonic oscillator will oscillate multiple times while the maximum amplitude weakens as time proceeds as shown in Fig 2.7. The general solution for an under-damped harmonic oscillator is:

$$X(t) = e^{-\Gamma t}(Acos(\Omega_D t) + Bsin(\Omega_D t)) \tag{2.55}$$

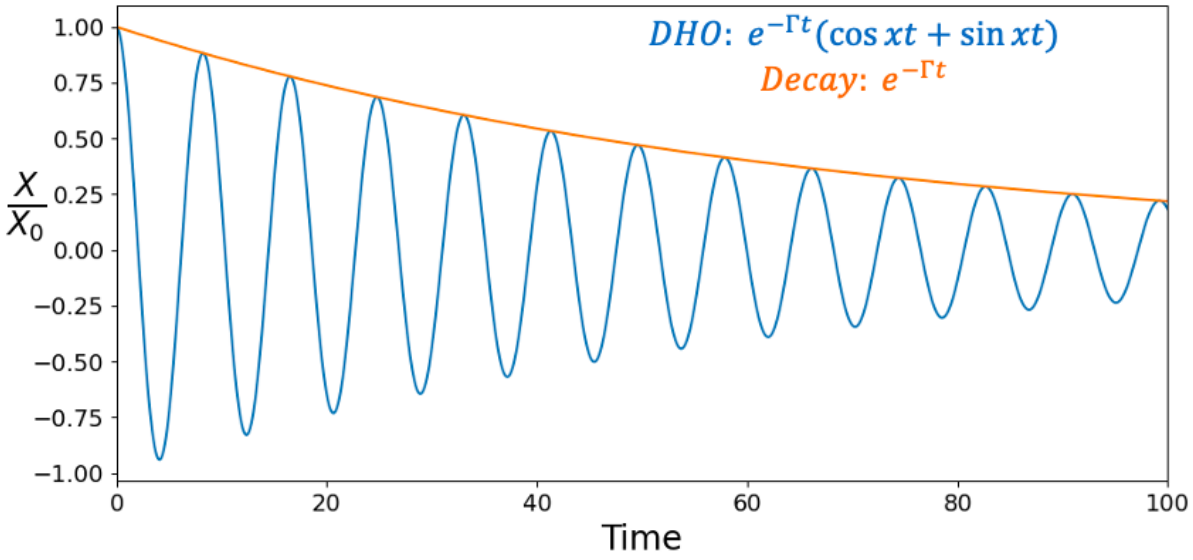

Figure 2.7: Damp harmonic oscillator in the under-damped condition

where the frequency of oscillation $\Omega_D = \sqrt{\Omega_0^2 - \Gamma^2}$, and A/B are constants that will be evaluated based on the initial conditions. From Fig 2.7, the correlation will be the maximum value at $t = 0$ while the derivative will be zero at $t = 0$, which gives the following set of initial condition:

$$\begin{aligned} X(0) &= \langle Q(0)Q(0)\rangle = \langle Q^2\rangle \\ \frac{dX(0)}{dt} &= 0 \end{aligned} \tag{2.56}$$

where $\langle Q^2\rangle$ is a statistical property called the variance of Q. Using the general solution Eq 2.55 in Eq 2.56 yields:

$$\begin{aligned} X(0) &= e^{-\Gamma 0}(Acos(0) + Bsin(0)) = e^0(A+0) = A \\ \frac{dX(0)}{dt} &= -\Gamma e^{-\Gamma 0}(Acos(0) + Bsin(0)) + e^{-\Gamma 0}(-\Omega_D Asin(0) + \Omega_D Bcos(0)) \\ &= -\Gamma e^0(A+0) + e^0(-\Omega_D B) = -\Gamma A - \Omega B = 0 \end{aligned} \tag{2.57}$$

such that $A = \langle Q^2 \rangle$ and $B = -\frac{\Gamma}{\Omega_D} A = -\frac{\Gamma}{\Omega_D} \langle Q^2 \rangle$. The unique solution for the correlation of Q becomes:

$$\begin{aligned} X(t) = \langle Q(t)Q(0) \rangle &= \langle Q^2 \rangle e^{-\Gamma t} (cos(\Omega_D t) - \frac{\Gamma}{\Omega_D} sin(\Omega_D t)) \\ \frac{dX(t)}{dt} = \langle P(t)Q(0) \rangle &= -\langle Q^2 \rangle e^{-\Gamma t} \frac{\Omega_0^2}{\Omega_D} sin(\Omega_D t) \end{aligned} \tag{2.58}$$

This solution can be used in Eq 2.54 to find the momentum P correlation in time,$\langle P(t)P(0) \rangle$ as:

$$\begin{aligned} \langle P(t)P(0) \rangle &= -\Omega_0^2 X - 2\Gamma \frac{dX}{dt} \\ &= \langle Q^2 \rangle \Omega_0^2 e^{-\Gamma t} (cos(\Omega_D t) - \frac{\Gamma}{\Omega_D} sin(\Omega_D t)) \\ &= \langle P^2 \rangle e^{-\Gamma t} (cos(\Omega_D t) - \frac{\Gamma}{\Omega_D} sin(\Omega_D t)) \end{aligned} \tag{2.59}$$

with $\frac{d^2X}{dt^2} = \frac{d\langle P(t)Q(0) \rangle}{dt} = -\frac{d\langle Q(t)P(0) \rangle}{dt} = -\langle P(t)P(0) \rangle$.

Both the time correlation of position X and momentum P are DHO and are related by $\langle Q^2 \rangle \Omega_0^2 = \langle P^2 \rangle$. Either can be used to calculate the 1-phonon spectrum. The real component of the Fourier transformation of the momentum correlation $F(\omega)$:

$$\text{Re}(F(\omega)) = \frac{2\omega^2 \Gamma}{(\omega^2 - \Omega_0^2)^2 + 4\omega^2 \Gamma^2} \tag{2.60}$$

reduces to a Lorenzian function when ω approaches Ω_0 as discussed earlier. In a later section, the importance of choosing the q-projected momentum correlation compared to the q-projected displacement correlation will be discussed.

2.6 Phonon Relation to Thermal Conductivity

Thermal conductivity κ is the rate of heat transfer in a material, such that:

$$\vec{J} = -\kappa \vec{\nabla}_{\vec{x}} T(x) \tag{2.61}$$

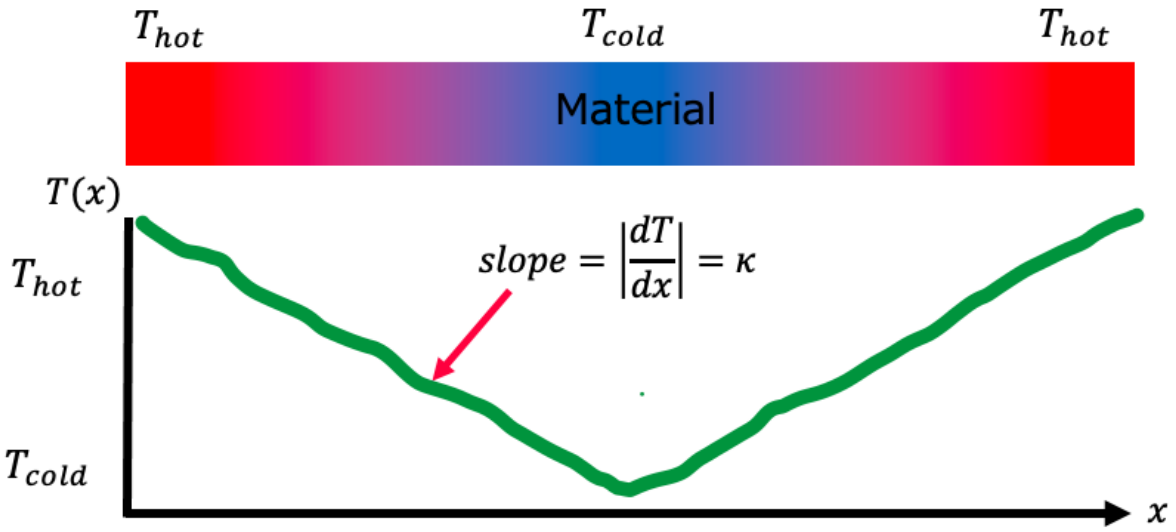

Figure 2.8: A material with a temperature gradient and the expected change of temperature as a function of distance

where $\vec{J}$ is the heat flow rate, and T is the temperature gradient inside a material, and $\vec{\nabla}_{\vec{x}}$ is the derivative with respect to $\vec{x}$. This can be measured with non-equilibrium molecular dynamics (NEMD) by creating a temperature difference in a material, then measuring the temperature change as a function of distance, shown in Fig 2.8. This comes with various sources for error including length between heat source and sink, interfacial effects, and rate of heat extraction.

As quantized carriers of energy, phonons play a vital role in the lattice component of the thermal conductivity. Other components of the thermal conductivity include the electron conductivity but the lattice component is the dominant term at moderate temperatures in crystal lattices. At higher temperatures, the electronic contribution may be upwards of 40% of the total thermal conductivity [17] but the focus of this dissertation is to quantify all the effects of the lattice contribution.

To contrast non-equilibrium dynamics, the two theories, used in this work, correlate equilibrium dynamics ACF to non-equilibrium properties. The first theory, Boltzmann transport equation with the relation time approximation, calculates the thermal conductivity with self-mode phonon heat flux at every q-point. The thermal conductivity comes solely from intra-mode transport. The second theory, Green-Kubo formalism, is a fluctuation-dissipation relation of statistical mechanics that relates the ACF of the heat current fluctuation to the transport

property, thermal conductivity. This is analogous to the dissipative relation of Brownian motion. Green-Kubo formalism is a more general equation including both intra-mode transport and inter-mode transport.

2.6.1 Phonon Bolzmann Transport Equation

The phonon Bolzmann transport equation (BTE) is widely used theory for thermal transport due the direct implementation with first-principle calculations. The generalized BTE:

$$\frac{df(p,r,t)}{dt} = \frac{\partial f}{\partial t} + \vec{\nabla}_{\vec{p}} f \cdot \frac{d\vec{p}}{dt} + \vec{\nabla}_{\vec{r}} \cdot \frac{d\vec{r}}{dt} \tag{2.62}$$

gives the probability density f that a particle can occupy a given state as a function of momentum, p, position r, and time t. As phonons scatter in time, the ensemble-averaged number density of that phonon mode f_α follows Bose-Einstein distribution:

$$f_{\alpha,eq} = \frac{1}{e^{\frac{\hbar\omega_\alpha}{k_b T}} - 1} \tag{2.63}$$

given $\hbar$ and k_b are Planck constant and Boltzmann constant, respectively. Under the steady state condition:

$$\frac{\partial f_\alpha}{\partial t} = 0 \tag{2.64}$$

the phonon number constant is in time. Applying the assumption that there are no creation or annihilation of phonons, all phonons change by scattering. Combining no net forces on phonons ($\frac{d\vec{p}}{dt} = 0$), Eq 2.64, and Eq 2.62, the phonon BTE equation becomes:

$$(\frac{df_\alpha}{dt})_{scattering} = \vec{\nabla}_{\vec{r}} f_\alpha \cdot \vec{v_{g_\alpha}} \tag{2.65}$$

where $\vec{v_{g_\alpha}}$ is the group velocity of a phonon mode α. In a near equilibrium condition, the probability density has small changes about equilibrium, such that $f_\alpha = f_{\alpha,eq} + \Delta f_\alpha$ where $|f_{eq}| \gg |\Delta f_\alpha|$. The right hand side of Eq 2.65 can be replaced with $\vec{\nabla}_{\vec{r}} f_{\alpha,eq} \cdot \vec{v_{g_\alpha}}$. Based on Eq 2.65, the diffusion of phonons are direct results of phonon scattering. The scatterings matrix is a complex mechanic that is too computationally intensive to get the full matrix. The

single-mode Relaxation Time Approximation (smRTA) approximates the scattering matrix

$$(\frac{df_\alpha}{dt})_{scattering} \approx \frac{f_\alpha - f_{\alpha,eq}}{\tau_\alpha} = -\frac{\Delta f_{\alpha,rta}}{\tau_\alpha} \tag{2.66}$$

with a relaxation constant (or phonon lifetime), τ. Solving for f_α with Eq 2.66 and Eq 2.65,:

$$\begin{aligned} f_\alpha &= f_{\alpha,eq} + \Delta f_{\alpha,rta} = f_{\alpha,eq} - \tau \vec{\nabla}_{\vec{r}} f_{\alpha,eq} \cdot \vec{v_{g_\alpha}} \\ &= f_{\alpha,eq} - \frac{\tau_\alpha c_{v,\alpha}}{\hbar\omega_\alpha} \vec{\nabla}_{\vec{r}} T \cdot \vec{v_{g_\alpha}} \end{aligned} \tag{2.67}$$

where:

$$c_{v,\alpha} = \vec{\nabla}_T E_\alpha = \hbar\omega_\alpha \vec{\nabla}_T f_{\alpha,eq} = \frac{\frac{\hbar\omega_\alpha}{k_b T^2} e^{\frac{\hbar\omega_\alpha}{k_b T}}}{(e^{\frac{\hbar\omega_\alpha}{k_b T}} - 1)^2} \tag{2.68}$$

is defined as the heat capacity and $\vec{\nabla}_{\vec{r}} f_\alpha = \vec{\nabla}_T f_\alpha \vec{\nabla}_{\vec{r}} T$.

The phonon heat flux $\vec{J}$ in a lattice of volume V as stated by the Peierls equation[38] as:

$$\vec{J} = \frac{1}{V} \sum_\alpha f_\alpha \hbar\omega_\alpha \vec{v_{g_\alpha}} \tag{2.69}$$

The group velocity $\vec{v_{g_\alpha}}$ is anti-symmetric in all of space, thus making the total equilibrium component equating to zero, $J_{eq} \equiv \frac{1}{V} \sum_\alpha f_{\alpha,eq} \hbar\omega_\alpha \vec{v_{g_\alpha}} = 0$, leaving the phonon heat flux as:

$$\vec{J} = \frac{1}{V} \sum_\alpha f_{\alpha,rta} \hbar\omega_\alpha \vec{v_{g_\alpha}} \tag{2.70}$$

. Using Eq 2.61 in the smRTA, the thermal conductivity:

$$\kappa_{IJ} = \frac{1}{V} \sum_\alpha \tau_\alpha c_{v,\alpha} \vec{v_{g_{\alpha,I}}} \vec{v_{g_{\alpha,J}}} \tag{2.71}$$

where I, J ranges over the basis direction. If the off-diagonal components of the thermal conductivity are small, $\kappa_{IJ} \approx \kappa_{IJ}\delta_{IJ}$, the bulk lattice thermal conductivity κ_{bulk} reduces to:

$$\kappa_{bulk} = \frac{1}{3}(\kappa_{xx} + \kappa_{yy} + \kappa_{zz}) = \frac{1}{3V} \sum_\alpha \tau_\alpha c_{v,\alpha} \vec{v_{g_\alpha}}^2 \tag{2.72}$$

With Eq 2.72, thermal conductivity calculations require three components: 1) mode frequencies ω_α, 2) lifetime τ_α, and 3) group velocity $\vec{v_{g_\alpha}}^2$ of all the phonon modes. The first two can be found with the 1-phonon spectra while the third can be found with the dynamical matrix.

2.6.2 Green-Kubo Formalism

Another common approach for solving thermal conductivity is the Green-Kubo equation:

$$\kappa = \frac{V}{k_b T^2} \int_0^\infty \langle \vec{J}(t) | \vec{J^*}(0) \rangle dt \tag{2.73}$$

with the ACF of the heat flux at temperature T , volume V, and Boltzmann constant, k_b. With current methodologies, this calculation requires a long simulation time length ($\sim$100s of ps or a few ns) as well as $\sim$100s of ensembles [18]. Currently, there is no universal definition of heat flux. The Peierls heat flux, definition by Eq 2.70 , can be used but is not derived from a general foundation. Implementation of a general heat flux has been shown to be nonphysical for 3+ body potentials with the current adoption in some simulations[4]. Corrections to particular 3- and 4-body potentials, e.g. Tersoff, have been developed to account for this error [13]. Another definition proposed by Hardy [21] derives heat flux through a volume V:

$$\vec{J} = \frac{1}{2V} \left\{ \sum_i \frac{\vec{p_i}}{m} \left(\frac{p_i^2}{2m_i} + U_i\right) + \sum_{ij} (\vec{R_i} - \vec{R_j}) \frac{1}{i\hbar} \left[\frac{p_i^2}{2m_i}, U_j \right] \right\} \tag{2.74}$$

with momentum $\vec{p_i}$, position $\vec{R_i}$, and potential energy U of the atom i with mass m_i, and [,] is the commutation operator such that $[A, B] = AB - BA$. The first term of Eq 2.74 describes the heat transported by the total energy. With this equating to the movement of the transport by the center of mass, this term is negligible for equilibrium solid dynamics. The remainder of this section treats the heat flux as the second term or lattice contribution.

A perturbation of the Hamiltonian, $H = H_0 + \lambda H'$, splits the Hamiltonian of a harmonic term and anharmonic term with a strength metric λ. Similarly, the heat flux split as $\vec{J} = \vec{J_0} + \lambda \vec{J'} + \lambda^2 \vec{J"}$. The heat flux a rising from the force constant matrices $\vec{J}_{FC}$ becomes:

$$\vec{J}_{FC} = \vec{J_2} + \lambda \vec{J_3} + \lambda \vec{J_4} \tag{2.75}$$

where J_n is the heat from the n^{th} order FC matrix. The heat flux from the harmonic force constant matrix is:

$$\vec{J_2} = -\frac{1}{2mV}\sum_{ij}\sum_{\alpha\beta}(\vec{R_i} - \vec{R_j})A_{\alpha\beta}(\vec{l_i}, \vec{l_j})Q_\beta(\vec{l_j})P_\alpha(\vec{l_i}) \tag{2.76}$$

with α and β ranging over the three coordinate directions, $\vec{l}$ is the lattice site distances, A is the 2^{nd} order FC matrix, P is the momentum of the phonon mode, and Q is the displacement from equilibrium. Separating the distance with an equilibrium position $\vec{r} + \vec{l}$, and displacement $\vec{Q}$,

$$\begin{aligned}\vec{J_2} =& -\frac{1}{2mV}\sum_{ij}\sum_{\alpha\beta}(\vec{r_i} + \vec{l_i} - \vec{r_j} - \vec{l_j})A_{\alpha\beta}(\vec{l_i}, \vec{l_j})Q_\beta(\vec{l_j})P_\alpha(\vec{l_i}) \\ &- \frac{1}{2mV}\sum_{ij}\sum_{\alpha\beta}(\vec{Q_i} - \vec{Q_j})A_{\alpha\beta}(\vec{l_i}, \vec{l_j})Q_\beta(\vec{l_j})P_\alpha(\vec{l_i}) \\ &= J_{2,lattice} + J_{2,displacement}\end{aligned} \tag{2.77}$$

This can be seen as the heat transfer between atoms at lattice sites compared to the actual distance between atoms. When the displacement from equilibrium is small compared to the equilibrium distance, $\vec{J}_{2,lattice} \gg \vec{J}_{2,displacement}$ but this is not true at higher temperatures. Higher temperatures give larger oscillation amplitudes that make the displacement term non-negligible. It can be shown with the inclusion of the annihilation and creation operators that $\vec{J}_{2,lattice} = \vec{J}_{2,diagonal} + \vec{J}_{2,off-diagonal}$ such that:

$$\vec{J}_{2,diagaonal} = \frac{1}{V}\sum_\alpha f_\alpha \hbar\omega_\alpha \vec{v_g}_\alpha \tag{2.78}$$

or the diagonal component reduces to that of the Peierls heat flux of Eq 2.69 while the off-diagonal term becomes a series of oscillating functions based on the frequency difference $\omega_\alpha - \omega_{\alpha'}$.

Both terms of Eq 2.77 can be converted into q-space, which will be the key to fixing the convergence and other numerical issues with the Green-Kubo formalism. The symmetry of FC matrices, ($A(\vec{l_i}, \vec{l_j}) = A(0, \vec{h}_{ji})$ where $\vec{h}_{ji} \equiv \vec{l_j} - \vec{l_i}$ for FC_2), implies that FC matrices are

independent of the reference point. This invariant with an inverse Fourier transformation:

$$\begin{aligned} Q_{i\alpha}(\vec{l}_i) &= \frac{1}{\sqrt{N}} \sum_{\vec{q}} Q_{i\alpha}(\vec{q}) e^{i\vec{q}\cdot(\vec{l}_i+\vec{r}_i)} \\ P_{i\alpha}(\vec{l}_i) &= \frac{1}{\sqrt{N}} \sum_{\vec{q}} P_{i\alpha}(\vec{q}) e^{i\vec{q}\cdot(\vec{l}_i+\vec{r}_i)} \end{aligned} \tag{2.79}$$

makes:

$$\begin{aligned} \vec{J}_{2,lattice} &= -\frac{1}{2mV} \sum_{ij} \sum_{\alpha\beta} \sum_{\vec{h}_{ji}} \sum_{\vec{l}_i} (\vec{r}_i - \vec{r}_j - \vec{h}_{ji}) A_{\alpha\beta}(0, \vec{h}_{ji}) \frac{1}{N} Q_\beta(\vec{l}_i + \vec{h}_{ji}) P_\alpha(\vec{l}_i) \\ &= -\frac{1}{2mV} \sum_{ij} \sum_{\alpha\beta} \sum_{\vec{h}_{ji}} \sum_{\vec{l}_i} \sum_{\vec{q}_1\vec{q}_2} (\vec{r}_i - \vec{r}_j - \vec{h}_{ji}) A_{\alpha\beta}(0, \vec{h}_{ji}) \frac{1}{N} Q_\beta(\vec{q}_2) P_\alpha(\vec{q}_1) e^{i\vec{q}_1\cdot(\vec{r}_i+\vec{l}_i)} e^{i\vec{q}_2\cdot(\vec{r}_i+\vec{l}_i+\vec{h}_{ji})} \end{aligned} \tag{2.80}$$

The exponential term:

$$\begin{aligned} &\sum_{\vec{l}_i} e^{i\vec{q}_1\cdot(\vec{r}_i+\vec{l}_i)} e^{i\vec{q}_2\cdot(\vec{r}_i+\vec{l}_i+\vec{h}_{ji})} \\ =&e^{i\vec{q}_1\cdot\vec{r}_i + i\vec{q}_2\cdot(\vec{r}_i+\vec{h}_{ji})} \sum_{\vec{l}_i} e^{i(\vec{q}_2+\vec{q}_2)\cdot\vec{l}_i} \end{aligned} \tag{2.81}$$

reproduces the selection rule, by Eq 2.10, such that $\vec{q}_1 = -\vec{q}_2 = \vec{q}$. Finally,

$$\vec{J}_{2,lattice} = \frac{1}{2mV} \sum_{ij} \sum_{\alpha\beta} \sum_{\vec{q}} \vec{\nabla}_{\vec{q}} A_{\alpha\beta}(\vec{q}) Q_\beta(\vec{q}) P^*_\alpha(\vec{q}) \tag{2.82}$$

where:

$$\vec{\nabla}_{\vec{q}} A_{\alpha\beta}(\vec{q}) \equiv \sum_{\vec{h}_{ji}} (\vec{r}_j + \vec{h}_{ji} - \vec{r}_i) A_{\alpha\beta}(0, \vec{h}_{ji}) e^{i\vec{q}\cdot(\vec{r}_j+\vec{h}_{ji}-\vec{r}_i)} \tag{2.83}$$

only requires the derivative of FC_2 (or dynamical matrix), q-projected velocity, and q-projected displacement. With product terms:

$$\begin{aligned} \vec{\Theta}_i &\equiv \vec{Q}(\vec{l}_i) P_\alpha(\vec{l}_i) \\ \vec{\Upsilon}_j &\equiv \vec{Q}(\vec{l}_j) Q_\alpha(\vec{l}_j) \end{aligned} \tag{2.84}$$

similar steps can be done with $\vec{J}_{2,displacement}$ to show:

$$\vec{J}_{2,displacement} = -\frac{1}{2mV}\sum_{ij}\sum_{\alpha\beta}\sum_{\vec{q}} A_{\alpha\beta}(\vec{q})\left\{\vec{\Theta}^{*}_{i}(\vec{q})Q_{\beta}(\vec{q}) + P^{*}_{\alpha}(\vec{q})\vec{\Upsilon}_{j}(\vec{q})\right\} \tag{2.85}$$

The heat flux by anharmonic FC terms can be defined in real space as:

$$\begin{aligned}\lambda\vec{J}_3 =& -\frac{1}{3mV}\sum_{ijk}\sum_{\alpha\beta\gamma}\sum_{\vec{h}_{ji}\vec{h}_{ki}}\sum_{\vec{l}_i}(\vec{r}_i - \vec{r}_j - \vec{h}_{ji})B_{\alpha\beta\gamma}(0,\vec{h}_{ji},\vec{h}_{ki})Q_{\beta}(\vec{l}_i+\vec{h}_{ji})Q_{\gamma}(\vec{l}_i+\vec{h}_{ki})P_{\alpha}(\vec{l}_i)\\ &-\frac{1}{3mV}\sum_{ijk}\sum_{\alpha\beta\gamma}\sum_{\vec{h}_{ji}\vec{h}_{ki}}\sum_{\vec{l}_i}(\vec{Q}_i - \vec{Q}_j)B_{\alpha\beta\gamma}(0,\vec{h}_{ji},\vec{h}_{ki})Q_{\beta}(\vec{l}_i+\vec{h}_{ji})Q_{\gamma}(\vec{l}_i+\vec{h}_{ki})P_{\alpha}(\vec{l}_i)\end{aligned} \tag{2.86}$$

and:

$$\begin{aligned}\lambda\vec{J}_4 =& -\frac{1}{4mV}\sum(\vec{r}_i - \vec{r}_j - \vec{h}_{ji})C_{\alpha\beta\gamma\rho}(0,\vec{h}_{ji},\vec{h}_{ki},\vec{h}_{li})Q_{\beta}(\vec{l}_i+\vec{h}_{ji})Q_{\gamma}(\vec{l}_i+\vec{h}_{ki})Q_{\rho}(\vec{l}_i+\vec{h}_{li})P_{\alpha}(\vec{l}_i)\\ &-\frac{1}{4mV}\sum(\vec{Q}_i - \vec{Q}_j)C_{\alpha\beta\gamma\rho}(0,\vec{h}_{ji},\vec{h}_{ki},\vec{h}_{li})Q_{\beta}(\vec{l}_i+\vec{h}_{ji})Q_{\gamma}(\vec{l}_i+\vec{h}_{ki})Q_{\rho}(\vec{l}_i+\vec{h}_{li})P_{\alpha}(\vec{l}_i)\end{aligned} \tag{2.87}$$

where B and C are the FC_3 and FC_4 matrices, respectively. Only the $\vec{J}_{3,lattice}$ and $\vec{J}_{4,lattice}$ are used for this work since $\vec{J}_{2,displacement}$ will be shown to be small compared to $\vec{J}_{2,lattice}$ later on and it can be reasonable argued that $\vec{J}_{4,displacement}$ and $\vec{J}_{4,displacement}$ would be significantly smaller. After converting to q-space,

$$\begin{aligned}\lambda\vec{J}_{3,lattice} &= \frac{1}{3mV\sqrt{N}}\sum_{ijk}\sum_{\alpha\beta\gamma}\sum_{\vec{q}_1\vec{q}_2\vec{q}_3}\vec{\nabla}_{\vec{q}}B_{\alpha\beta\gamma}(\vec{q}_1,\vec{q}_2,\vec{q}_3)Q_{\beta}(\vec{q}_2)Q_{\gamma}(\vec{q}_3)P_{\alpha}(\vec{q}_1)\Delta(\vec{q}_1+\vec{q}_2+\vec{q}_3)\\ \lambda\vec{J}_{4,lattice} &= \frac{1}{4mVN}\sum_{ijkl}\sum_{\alpha\beta\gamma\rho}\sum_{\vec{q}_1\vec{q}_2\vec{q}_3\vec{q}_4}\vec{\nabla}_{\vec{q}}C_{\alpha\beta\gamma\rho}(\vec{q}_1,\vec{q}_2,\vec{q}_3,\vec{q}_4)Q_{\beta}(\vec{q}_2)Q_{\gamma}(\vec{q}_3)Q_{\rho}(\vec{q}_4)P_{\alpha}(\vec{q}_1)\Delta(\vec{q}_1+\vec{q}_2+\vec{q}_3+\vec{q}_4)\end{aligned} \tag{2.88}$$

with:

$$\vec{\nabla}_{\vec{q}} B_{\alpha\beta\gamma}(\vec{q}_1,\vec{q}_2,\vec{q}_3) \equiv e^{i(\vec{q}_1+\vec{q}_2+\vec{q}_3)\cdot\vec{r}_i} \sum_{\vec{h}_{ji}\vec{h}_{ki}} (\vec{r}_j+\vec{h}_{ji}-\vec{r}_i) e^{i\vec{q}_2\cdot(\vec{r}_j+\vec{h}_{ji}-\vec{r}_i)} e^{i\vec{q}_3\cdot(\vec{r}_k+\vec{h}_{ki}-\vec{r}_i)}$$

$$\vec{\nabla}_{\vec{q}} C_{\alpha\beta\gamma\rho}(\vec{q}_1,\vec{q}_2,\vec{q}_3,\vec{q}_4) \equiv e^{i(\vec{q}_1+\vec{q}_2+\vec{q}_3+\vec{q}_4)\cdot\vec{r}_i} \sum_{\vec{h}_{ji}\vec{h}_{ki}\vec{h}_{li}} (\vec{r}_j+\vec{h}_{ji}-\vec{r}_i) e^{i\vec{q}_2\cdot(\vec{r}_j+\vec{h}_{ji}-\vec{r}_i)} e^{i\vec{q}_3\cdot(\vec{r}_k+\vec{h}_{ki}-\vec{r}_i)} e^{i\vec{q}_4\cdot(\vec{r}_l+\vec{h}_{li}-\vec{r}_i)} \tag{2.89}$$

Due to the resource limitations, $\vec{J}_{4,lattice}$ is reduced in q-space to

$$\lambda \vec{J}_{4,lattice} = \frac{1}{4mVN} \sum_{ij} \sum_{\alpha\beta} \sum_{\vec{q}} \vec{\nabla}_{\vec{q}} A^{eff}_{\alpha\beta}(\vec{q}) Q_\beta(\vec{q}) P^*_\alpha(\vec{q}) \tag{2.90}$$

by creating an effective time-dependent FC_2 matrix:

$$A^{eff}_{\alpha\beta}(\vec{l}_i,\vec{l}_j) \equiv \sum_{kl} \sum_{\gamma\rho} C_{\alpha\beta\gamma\rho}(\vec{l}_i,\vec{l}_j,\vec{l}_k,\vec{l}_l) Q_\gamma(\vec{l}_k) Q_\rho(\vec{l}_l) \tag{2.91}$$

This reduces the selection rule imposed on the $\vec{J}_{4,lattice}$ from $\Delta(\vec{q}_1+\vec{q}_2+\vec{q}_3+\vec{q}_4)$ to $\Delta(\vec{q}_1+\vec{q}_2)$. The possible implications of this selection rule reduction will be expanded upon later.

The heat flux used:

$$\begin{aligned} \vec{J} &\approx \vec{J}_{2,lattice} + \vec{J}_{2,displacement} + W^1_{34}\lambda\vec{J}_{3,lattice} + W^2_{34}\lambda\vec{J}_{4,lattice} \\ &= \vec{J}_{2,diagonal} + \vec{J}_{2,off-diagonal} + \vec{J}_{2,displacement} + W^1_{34}\lambda\vec{J}_{3,lattice} + W^2_{34}\lambda\vec{J}_{4,lattice} \end{aligned} \tag{2.92}$$

now requires weights W^1_{34} and W^2_{34}. These weights will account for the renormalization of both the FC_3 and FC_4 and will be determined using a linear regression model of the q-projected force:

$$\begin{aligned} f_{i\alpha}(\vec{q}) &= \frac{1}{\sqrt{N}} \sum_{\vec{l}_i} f_{i\alpha}(l) e^{-i\vec{q}\cdot(\vec{l}_i+\vec{r}_i)} \\ &\approx \sum_{j\beta} A_{\alpha\beta}(\vec{q}) Q_{j\beta}(\vec{q}) + W^1_{34}\frac{1}{2!} \sum_{j\beta}\sum_{k\gamma} B_{\alpha\beta\gamma}(-\vec{q},\vec{q}_2,\vec{q}_3) Q_{j\beta}(\vec{q}_2) Q_{k\gamma}(\vec{q}_3) + W^2_{34}\frac{1}{2}\sum_{j\beta} A^{eff}_{\alpha\beta}(\vec{q}) Q_{j\beta}(\vec{q}) \end{aligned} \tag{2.93}$$

and Taylor series expansion up to the 4^{th} order. The linear regression model will predict the best weights in the series expansion to fit the full q-projected force. For this model to be accurate, approximation of 2.93 must be valid and the dependent variable (full q-projected force) has to be correlated to the independent variable (series expansion with weights). This model is included in the machine-learning package scikit-learn [37] in python. The coding implentation of these heat flux components utilize and expand upon many functions developed in Phono3py [54]. Other perturbation contributions to the heat flux include lattice defects, boundaries, etc. Due to the simulations being a periodic crystal with low defects, these other perturbations are not discussed.

Chapter 3

Molecular Dynamic Simulations

This chapter explains how Large-scale Atomic/Molecular Massively Parallel Simulator (LAMMPS) with a machine-learning based Gaussian Approximation Potential (GAP) is utilized to extract the equilibrium atomic dynamics (force, velocity, displacement) necessary to predict the lattice thermal conductivity κ_L. We use a finite displacement method to get the force constant (FC) matrices. Lastly, we discuss projecting the atomic dynamics into q-space and the implicit commensurate grid from the system size.

3.1 Governing Equation

Molecular dynamics (MD) simulations provide a numerical solution to all atomic trajectories providing the evolution of a micro-system throughout time given initial conditions. Classical MD only considers the interactions between multiple atoms while ab-inito MD includes internal contributions to the atomic evolution i.e. electronic-ion interactions. These extra interactions of the internal interactions require solving the quantum Schrödinger equation of motion. Classical MD typically uses an empirical force field to define the atom-atom interactions. Newtonian equations of motion drives the atomic dynamics with the requirement of an interatomic potential. Conservation of force using interatomic potentials dictates a Newtonian equation of motion of a system with N atoms as:

$$F_i = -\nabla V(\mathbf{r}_i), i = 1, 2, 3..N \tag{3.1}$$

where F is the force, V is the potential energy, and $\mathbf{r}$ is the atomic coordinates. Expanding Eq. 3.1 becomes:

$$m\frac{d^2\mathbf{r}_i}{dt^2} = -\nabla V(\mathbf{r}_i), i = 1, 2, 3..N \tag{3.2}$$

with m being the mass of the particle. Since all other variables are a constant as a function of time, the atomic coordinates describes the evolution of a MD system.

3.2 Interatomic Potential

Due to the necessity of an interatomic potential, the numerical accuracy of MD simulations rely heavily on the supplied potential energy (or force-field) and initial constraints. Commonly used empirical potentials, e.g. Tersoff [50], and Stillinger and Weber [45], approximates the surface energy of the system from observed data. This improves the computational cost but comes with a penalty on accuracy compared to ab-inio density functional theory (DFT) calculations. These potentials use a qualitative approach to a potential and lack quantum accuracy. Recent advances in machine-learning (ML) has provided new potentials for molecular dynamic simulations with near quantum mechanics accuracy in Gaussian Approximation Potential (GAP) and Spectral Neighbor Analysis Potential (SNAP)[3, 52]. Of these two, GAP is shown to have the lower error with respect to DFT calculations across various testing properties while versions of SNAP have significantly lower computational costs shown in Fig 3.1[57]. This work focused on GAP due to the lower error to test the limits of molecular dynamic accuracy.

Machine-learning potentials aim to build a general interatomic potential by fitting their kernel functions with DFT calculations. The kernels functions are means of mapping data or basis function for atomistic potentials. Including different atomic configurations, e.g. isotopes, defects, atomic structures, creates a more general purpose potential for uses of a material. This prevents over-fitting by not focusing on particular aspects of a material but rather the predicted pattern of a material. The GAP model uses a smooth overlap of atomic positions (SOAP) kernel function with a Gaussian process regression (GPR) model to solve for the fitting parameters[3].

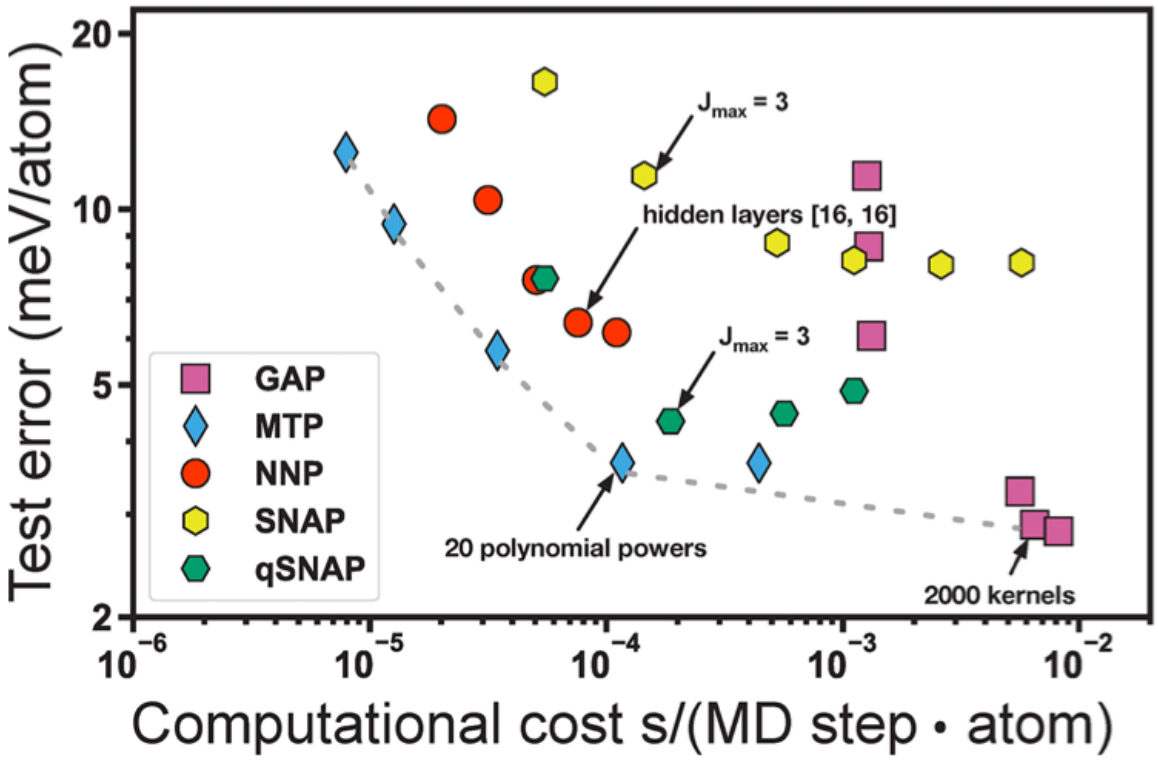

Figure 3.1: Accuracy of various ML interatomic potentials and the corresponding computational cost by a 2020 study from Zuo et. al. [57]

The basis functions for the SOAP kernel maps environments based on their neighbor density:

$$\rho_i(\mathbf{r}) = \sum_{'} f_{cut}(r_{ii'}) e^{\frac{\mathbf{r}-\mathbf{r}_{ii'}}{2\sigma^2_{atom}}} \tag{3.3}$$

where σ is a smearing parameter, f_{cutt} is a cutoff function, and i' are neighbors of atom i in a given cutoff radius. The neighbor density can be defined with spherical harmonic basis:

$$\rho_i(\mathbf{r}) = \sum_{nlm} c^i_{nlm} Y_{lm}(\hat{\mathbf{r}}) g_n(r) \tag{3.4}$$

with the corresponding power spectrum:

$$\tilde{\rho}^i_{nn'l} = \sum_{m=-1}^{l} c^{i*}_{nlm} c^i_{n'lm} \tag{3.5}$$

This power spectrum has rotation and permutation invariant necessary to create a unique basis. The SOAP kernel mapping environments R_i and R_j becomes:

$$K(R_i, R_j) = 3|\mathbf{p}^i \cdot \mathbf{p}^j|^4 eV \tag{3.6}$$

with $\mathbf{p}^i$ being the normalized power spectrum. The total energy of a system,E, can be decomposed to a pair and many-body potential terms:

$$E = \sum_{i<j} V_{pair}(r_{ij}) + \sum_i \sum_s^M \alpha_s K(R_i, R_j) \tag{3.7}$$

where r_{ij} is the distance between atoms i,j, M is all atomic sets from selected data, and α is the fitting parameters of a set. Using a database of DFT calculation, the GAP model uses GPR to solve for the fitting parameters, α, in Eg 3.7 as:

$$\alpha^* = [\mathbf{K}_{MM} + (\mathbf{L}\mathbf{K}_{NM})^T \Lambda^{-1} \mathbf{L}\mathbf{K}_{NM}]^{-1} (\mathbf{L}\mathbf{K}^T_{NM} \Lambda^{-1} \mathbf{y}) \tag{3.8}$$

where M is an atomic set within N environments of a testing set, Λ is a diagonal matrix of weights given to the input data, $\mathbf{L}$ is a linear operator connecting a vector, $\mathbf{y}$, of input data to an unknown vector of atomic energies [3].

3.3 Solving Newtonian Equations

Solving for the Newtonian equation provides an evolution of the system at each time step. Shown in Eq 3.2, this requires a description of the position at each time step. A common technique for this is the Stoermer-Verlet time integration. Following kinematics for an object with constant acceleration a, position as of function of time is:

$$\mathbf{r}(t) = \mathbf{r}_0 + \mathbf{v}_0 t + \frac{1}{2}\mathbf{a}_0 t^2 + \frac{1}{6}\mathbf{b}_0 t^2 + O(\Delta t^4) \tag{3.9}$$

or

$$\mathbf{r}(t) = \mathbf{r}_0 + \frac{d\mathbf{r}}{dt}t + \frac{1}{2}\frac{d^2\mathbf{r}}{dt^2}t^2 + \frac{1}{6}\frac{d^3\mathbf{r}}{dt^3}t^3 + O(\Delta t^4) \tag{3.10}$$

where v is velocity, b is jerk, and $O(\Delta t^4)$ are all higher order terms. A Taylor-series expansion about time t with a small time step Δt gives:

$$\mathbf{r}(t+\Delta t) = \mathbf{r}_0 + \frac{d\mathbf{r}}{dt}\Delta t + \frac{1}{2}\frac{d^2\mathbf{r}}{dt^2}\Delta t^2 + \frac{1}{6}\frac{d^3\mathbf{r}}{dt^3}\Delta t^3 + O(\Delta t^4) \tag{3.11}$$

Due to reversibility of time, a time step backwards means:

$$\mathbf{r}(t-\Delta t) = \mathbf{r}(t) - \frac{d\mathbf{r}}{dt}\Delta t + \frac{1}{2}\frac{d^2\mathbf{r}}{dt^2}\Delta t^2 - \frac{1}{6}\frac{d^3\mathbf{r}}{dt^3}\Delta t^3 + O(\Delta t^4) \tag{3.12}$$

Adding Eq 3.11 and 3.12, yields:

$$\mathbf{r}(t+\Delta t) = 2\mathbf{r}(t) - \mathbf{r}(t-\Delta t) + \frac{\mathbf{f}}{m}\Delta t^2 + O(\Delta t^4) \tag{3.13}$$

with $\mathbf{f} = m\mathbf{a}$. Any subsequent time step of position is dependent only on the previous position, and current position and force. By dropping the higher order terms, this gives error of the position as $O(\Delta t^4)$. With positions at new time steps, solving for velocity at a subsequent time

steps follows similar steps as the position by subtracting Eq 3.11 and 3.12. Velocity becomes:

$$\mathbf{v}(t+\Delta t) = \frac{\mathbf{r}(t+\Delta t) - \mathbf{r}(t-\Delta t)}{2\Delta t} + \frac{\mathbf{b}\Delta t^3}{3\Delta t} \tag{3.14}$$

Dropping the jerk term gives a velocity error of $O(\Delta t^2)$

3.4 Running EMD Simulations

Discussed earlier, thermal conductivity can be expressed from thermal equilibrium dynamics and statistical mechanics. Statistical mechanical systems have microscopic states that are controlled by macroscopic properties. Three main thermal equilibrium ensembles are canonical (NVT), isothermal-isobaric (NPT), and micro-canonical (NVE). A system of N particles and volume V, in contact with a heat bath at temperature T makes an NVT ensemble. With constant pressure P, a NPT ensemble allows a system to expand to a natural size. NVT and NPT are useful for driving the system to thermal equilibrium at a given temperature. Temperature is maintained by adding constraints to the velocity, thus fixing the temperature while altering the system dimensions controls the pressure. These add extra constraints to the system and may lead to unwanted manipulations to the system. With only conservation of energy E due to a non-interacting system, NVE ensembles produces dynamics with Stoermer-Verlet time integration algorithm. Systems that undergone thermal equilibrium will have varying energies at different time steps. Ensembles averages of these varying energy states reduce the numerical uncertainty.

All molecular dynamics simulations for this works was done using the Large-scale Atomic/Molecular Massively Parallel Simulator (LAMMPS) program [51] on Auburn's Easley super-computing cluster. The workflow for getting atom dynamics are shown in Fig 3.2. GAP must be ran with the command:

```
units metal
```
(3.15)

where time is measured in picoseconds with a default timestep (dt) of .001 ps. Although LAMMPS has built-in commands for crystal lattices, the diamond lattices used were built with

an auxiliary code called Latgen for consistency[30]. The following commands:

```
variable T equal 300
velocity all create $T 456783 mom yes rot yes dist gaussian
```
(3.16)

creates a temperature variable and initializes the velocity with a Gaussian distribution given a random seed (456783) at that temperature. The total translational and rotational symmetry is zeroed out to prevent any initial center of mass (COM) or rotational movement. With an initial velocity configuration and Stoermer-Verlet algorithm, positions, velocity, and forces can be updated at each time step. A thermalization allows the system to relax to a particular temperature for 40,000 timesteps with a drag coefficient of (100×timestep) by the following commands:

```
fix NVT all nvt temp $T $T $(100*dt)
run 40000
```
(3.17)

Restart files are outputted every 1000 timesteps after NVT to create up to 10 unique ensembles with:

```
restart 1000 restart.*
run 1000
```
(3.18)

Prior to running the NVE ensembles, the command

```
unfix NVT
```
(3.19)

stops the NVT command and velocities are scaled to guarantee the NVE starts at the given temperature with:

```
velocity all scale $T
```
(3.20)

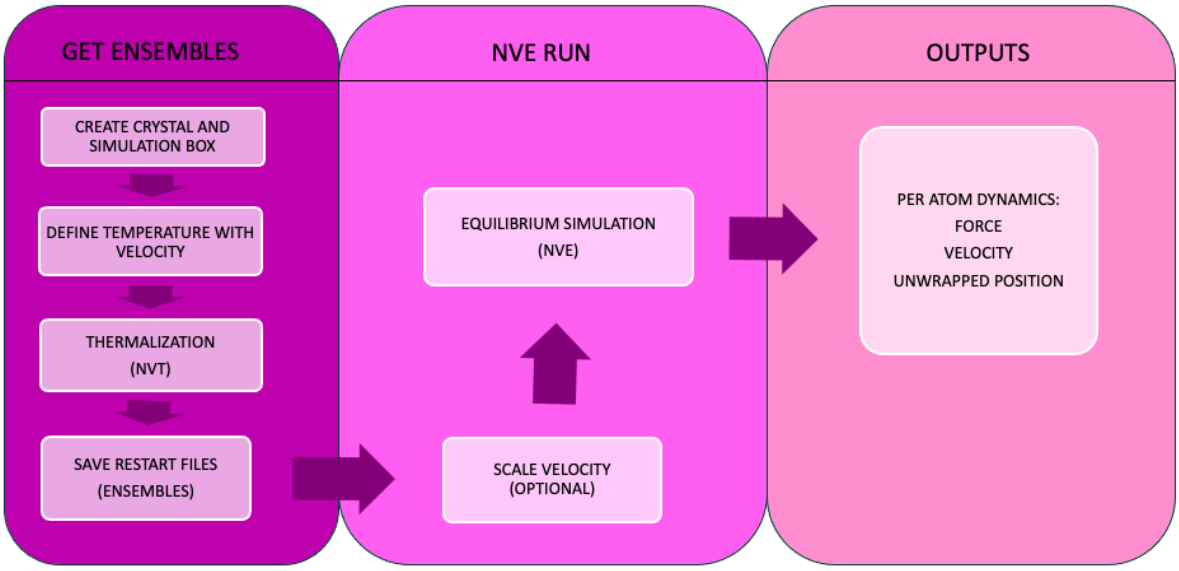

Figure 3.2: Workflow used to create various ensembles of the atomic dynamics

Lastly, the per atom force, velocity, and unwrapped position is outputted per integer time step during the NVE simulation with:

$$\begin{aligned} &\text{fix NVE all nve} \\ &\text{run 100000} \end{aligned} \tag{3.21}$$

and multiple dump commands. The unwrapped positions are the positions of the atoms without accounting for the periodicity of the simulation box. This is more useful than outputting the raw displacement or position values since the reference position for the displacement used for calculations can be adjusted as needed.

A simulation time step varies depending on the timescale of the system dynamics. For lattice vibrations and similarly physical properties, a typical time step is on the order of 1 femtoseconds with a total run-time on the order of 1 nanoseconds (or 1 million fs). With parallelization, a computer cluster can handle upwards of 1 million atoms depending on the complexity of the interatomic potential. In comparison, first-principle calculations is restricted to $\sim$100s of atoms. This number of atoms are significantly less than realistic number of atoms in bulk systems. The limited size will create an inherent boundary effect in simulations since many atoms will be at the boundary of the simulation box. To offset the size effect, a periodic

boundary condition was used with the command:

$$\text{boundary p p p} \tag{3.22}$$

on large atomic cells, supercells. The periodic boundary condition 1) adds virtual image atoms outside the boundary, and 2) creates a continues pathway between ends of a simulation box.

A priority of this work was to achieve high accuracy with an efficient use of computational resources. For reference, this 100000 NVE run-time with 4096 atoms and the GAP potential takes about 8 hrs to finish with 480 cores of 3.00GHz processing power on the Easley super-computing cluster. The selected NVE run-time was chosen to prevent any simulations from terminating early due to lack of dedicated nodes. The simulation parameters to get the dynamical properties are in Table 3.4. The GAP interatomic potential has a computational cost of 10^2 s/(MD step * atoms), which is order of magnitudes larger than some other ML potentials[57]. With non-dedicated node for parallelization on the super-computing cluster, a limit of $\sim$1000s of atoms and $\sim$100s of ps simulation time was used for a reasonable run-time and storage space. The choice of 4096 atoms allows for the commensurate q-point grid, discussed in the next section, to sample all the high symmetry q-points to compare to other experimental results while avoiding possible edge effects. The experimental lattice constant used for each temperature was based on the experimental lattice expansion at constant atmospheric pressure [36]. This should reduce any lattice expansion contributions to the thermal conductivity. Since the temperature is never changed throughout this process, the NVT ensemble does not need to have a long simulation time and serves to provide different starting energies for unique NVE ensembles. 5 ensembles are used per temperature/lattice constant pairing by saving the restart files of the last (n-1)$\times$1,000 time-steps of the NVT run-time. This has been shown to give better ensemble average convergence for Green-Kubo calculations as compared to dividing a single long run into multiple ensembles [18].

Simulation Parameters					
time-step	1 fs				
# of steps	50,000 (NVT)			100,000 (NVE)	
Crystal size	4096 atoms				
Steps per output	1				
Temperatures (Kelvin)	300	600	900	1200	1500
Lattice Constants (Angstroms)	5.431	5.437	5.443	5.450	5.458

Table 3.1: Simulation parameters for NVE and NVT runs for dynamical output

3.5 Getting Force Constants

The force constant matrices are the n-th order displacement derivative of the potential:

$$FC_n = \frac{\partial^n U}{\partial u^n} \tag{3.23}$$

With a conservative force $F = -\nabla U$, the force constants can be rewritten with the force:

$$FC_n = \frac{\partial^{n-1} f}{\partial u^{n-1}} \tag{3.24}$$

The partial derivative can be approximated using the finite displacement method by evaluating the change in the n-1 force constant matrix after a small displacement Δr in opposite directions:

$$FC_n \approx \frac{FC_{n-1}(\Delta r) - FC_{n-1}(-\Delta r)}{2\Delta r} \tag{3.25}$$

For example, the second order force constant matrix, FC_2, is solved by displacing an atom in one direction and measuring the change in the 0-th order FC matrix i.e. the force on the atom. A reasonable value for the finite displacement is on the order of .01 Å.

The higher order FC matrix calculations will require all previous order FC matrices. With a full FC calculation requiring two displacements in all 3 Cartesian directions for N atoms, the next order FC matrix will have a computational time of $6N$ times the time of the previous FC order. This restricts the number of atoms since the size of a full FC_n matrix is $(3N)^n$ and needs $(6N)^n$ calculations. All FC matrices can be represented in a reduced form since a basis atom will have identical force constants with a basis atom in another position with shape

$(3N_{basis})(3N)^{n-1}$. A FC_2 matrix for a 4096 atom supercell has the shape $(4096 \times 3)^2$ with $\sim$1 GB of storage space and $\sim$1 hr computational wall-time on 480 Intel Xeon Gold 6248R 3.00GHz nodes with LAMMPS. FC_3 and FC_4 use a 216- and 64-atom supercell, respectively, with storage of $\sim$ 2 GB for the full FC_3 and 300 MB for the reduced FC_4. The 216 FC_3 takes $\sim$26 hrs to compute with LAMMPS while there is no built-in modules for computing FC_4. Without parallelzing each 64-atom FC_3 displacement calculation, a 64-atom FC_4 only takes about $\sim$12 hrs to compute.

3.6 Post-processing

LAMMPS can output the N_a atom dynamical trajectories (force, velocity, position) any interval t time-steps. These can be converted to a $(t, N_a, 3)$ dimensional array with the NumPy python package. The atomic dynamics do not need to be output every time-step to preserve storage space but this can be adjusted in future work. The time-step and total time will have a direct impact on the frequency resolution of the 1-phonon spectra but the techniques shown later will alleviate some of the resolution issues. With 100,000 fs time-steps, the dynamical trajectories of a 4096 atoms supercell utilize $\sim$ 9 GB of storage.

These trajectories can be converted to q-space mesh of size N_q with a Fourier transformation:

$$v_{i\alpha}(\vec{q}) = \frac{1}{\sqrt{N_q}} \sum_{\vec{l_i}} v_{i\alpha}(\vec{l_i}) e^{-i\vec{q}\cdot(\vec{l_i}+\vec{r_i})} \tag{3.26}$$

where i is the basis atom in the primitive cell and $\vec{l_i}$ ranges over all the atoms of the supercell that maps to the i-th basis atom by translation and α is a Cartesian direction. In q-space, the q-projected trajectory at a particular $\vec{q}$ is a superposition of normal modes b and eigenvectors e_b, such that for velocity v and displacement d:

$$\begin{aligned} v_{i\alpha}(\vec{q}) &= \sum_b P_{\vec{q},b} e_{i\alpha}(\vec{q}, b) \\ d_{i\alpha}(\vec{q}) &= \sum_b Q_{\vec{q},b} e_{i\alpha}(\vec{q}, b) \end{aligned} \tag{3.27}$$

There is no rigid definition for the eigenvectors beyond the bare phonon approach. The eigenvectors will naturally vanish in the auto-correlation function (ACF) with a summations over the primitive atoms:

$$\begin{aligned} g_{\vec{q}}(t) &\equiv \sum_{i\alpha,j\beta} \sqrt{m_i m_j} \langle v_{\vec{q},i,\alpha}(t) v^*_{\vec{q},j,\beta}(0) \rangle \\ &= \sum_{b,b'} \langle P_{\vec{q},b}(t) P^*_{\vec{q},b'}(0) \rangle \sum_{i\alpha,j\beta} e_{i\alpha}(\vec{q},b) e^*_{j\beta}(\vec{q},b') \\ &= \sum_{b,b'} \langle P_{\vec{q},b}(t) P^*_{\vec{q},b'}(0) \rangle \delta_{b,b',i,j} \\ &= \sum_{b} \langle P_{\vec{q},b}(t) P^*_{\vec{q},b}(0) \rangle \end{aligned} \tag{3.28}$$

Due to the supercell being a finite size, the q-projected trajectories only sample particular q-points in the N_q mesh called commensurate points.

A particular q-point can be represented by reciprocal lattices from conventional $\vec{b}_c$ or primitive $\vec{b}$ lattice vectors:

$$\begin{aligned} \vec{q} &= u_c \vec{b}_{c,1} + v_c \vec{b}_{c,2} + w_c \vec{b}_{c,3} \\ &= \frac{v_c + w_c}{2} \vec{b_1} + \frac{u_c + w_c}{2} \vec{b_2} + \frac{u_c + v_c}{2} \vec{b_3} \end{aligned} \tag{3.29}$$

such that:

$$\begin{aligned} u &= \frac{v_c + w_c}{2} \\ v &= \frac{u_c + w_c}{2} \\ w &= \frac{u_c + v_c}{2} \end{aligned} \tag{3.30}$$

With a $N1 \times N2 \times N3$ integer replication of the cubic cell,

$$\begin{aligned} u_c &= \frac{n_1}{N_1}, \quad n_1 \in [0, N_1] \\ v_c &= \frac{n_2}{N_2}, \quad n_2 \in [0, N_2] \\ w_c &= \frac{n_3}{N_3}, \quad n_3 \in [0, N_3] \end{aligned} \tag{3.31}$$

which makes:

$$\begin{aligned} u &= \frac{1}{2}(\frac{n_2}{N_2} + \frac{n_3}{N_3}), \quad 0 \leq u \leq 1 \\ v &= \frac{1}{2}(\frac{n_1}{N_1} + \frac{n_3}{N_3}), \quad 0 \leq v \leq 1 \\ w &= \frac{1}{2}(\frac{n_1}{N_1} + \frac{n_2}{N_2}), \quad 0 \leq w \leq 1 \end{aligned} \tag{3.32}$$

For a $(8 \times 8 \times 8) \times 8$ atom diamond supercell model (4096 atoms), the commensurate $\vec{q}$-points, $\vec{q_0}$, are:

$$\vec{q_0} \Rightarrow \begin{cases} u_0 = \frac{1}{16}(n_2 + n_3), & n_1 \in [0, 8] \\ v_0 = \frac{1}{16}(n_1 + n_3), & n_2 \in [0, 8] \\ w_0 = \frac{1}{16}(n_1 + n_3), & n_3 \in [0, 8] \end{cases} \tag{3.33}$$

with 2048 total q-points in the N_q mesh. The full q-projected trajectories will be complex values of shape $(t, N_q, N_{basis}, 3)$ and consequently requiring more space ($\sim$ 18 GB).

Contrary to the sampling of q-projected trajectories, the FC matrices can be projected to any q-point. This makes the mapping the smaller sized FC_3 and FC_4 to the trajectories possible. The q-projected FC matrices are bound by the selection rule. As discussed before, the selection rule for $FC_2(\vec{q_1}, \vec{q_1})$ dictates $\vec{q_1} = -\vec{q_2}$. By selecting two q-points from the commensurate grid and searching for the last to satisfy the 3-phonon selection rule, $\vec{q_1} + \vec{q_1} + \vec{q_1} = \vec{G}$, a pattern was found. If two q-points are chosen at random from the grid and then there is only one unique q-point in the commensurate grid to satisfy the condition. This logic hold for the 4-phonon selection rule as well. Thus, a q-projected FC_n to have the shape $(N_q^{n-1}, N_{basis}^n, 3^n)$. This shape is manageable for a q-projected FC. Discussed later, the size will become an issue for any q-projected calculations that require the FC_4 and the reasoning behind the effective time-dependent force constant matrix A^{eff}.

Inside the commensurate grid, there are many q-points that are equivalent to each other by rotational transformation matrices. For example, the X-point $(0.0, 0.5, 0.5)$ as two equivalent

q-points:

$$\begin{bmatrix} 0.5 \\ 0 \\ 0.5 \end{bmatrix} = \begin{bmatrix} 0 & -1 & 0 \\ 1 & 0 & 0 \\ 0 & 0 & 1 \end{bmatrix} \begin{bmatrix} 0.0 \\ 0.5 \\ 0.5 \end{bmatrix} \tag{3.34}$$

and

$$\begin{bmatrix} 0.5 \\ 0.5 \\ 0.0 \end{bmatrix} = \begin{bmatrix} 0 & 0 & -1 \\ 0 & 1 & 0 \\ 1 & 0 & 0 \end{bmatrix} \begin{bmatrix} 0.0 \\ 0.5 \\ 0.5 \end{bmatrix} \tag{3.35}$$

The rotation transformations are not unique and two equivalent q-points can have multiple transformation matrices. Symmetry of the cell determines all the possible rotations and libraries like phonopy and spglib can output these transformations. The 2048 commensurate grid can be reduced to an irreducible grid of 85 unique q-points by rotation with unique values of [1, 3, 4, 6, 8, 12, 24, 48], and a mean value of 24 equivalent q-points. The lowest equivalent q-points are high symmetry points with the lowest 3 (1, 3, 4) belong to the Γ-, X-, and L-point, respectively. Equivalent q-points will have similar information that can be averaged over to be used in lieu of more ensemble runs. This work will show that combining results from equivalent q-points while enforcing orthogonality between q-points and/or fitting the results with an equation can make MD simulations viable as a primary source for phonon research.

Chapter 4

MD Simulated Phonon Properties at Finite Temperatures

Since the early stage of quantum mechanics, researchers have sought to interpret experimental lattice thermal conductivity data of crystals using the phonon-based kinetic Boltzmann Transport Equation (BTE). At the single-model level (sm-BTE), the lattice thermal conductivity (κ_L) can be expressed through terms derived from phonon dispersions (c_v and $\vec{v_g}$) and phonon lifetimes (τ). However, in practice, the sm-BTE approach's applicability is restricted only to moderate temperature ranges due to two commonly employed numeric approximations: the use of bare phonon dispersions and perturbative evaluations of tau. Although some previous studies have reported molecular dynamics (MD) simulations to determine phonon frequencies and lifetimes, the limited size of simulation cells (typically a few hundred atoms) and the relatively short simulation times (less than 10 picoseconds) introduce significant numerical uncertainties into the simulated data. Currently, there exists a notable gap in the literature concerning robust simulation studies on renormalized phonon frequencies and lifetimes at very high temperatures, specifically those just below the melting point. This chapter addresses this gap by presenting three key contributions: 1) demonstrating how q-space symmetry can mitigate numerical noise in 1-phonon spectra, 2) introducing a reliable fitting algorithm for extracting temperature-dependent frequency (ω) and lifetime (τ) values across a range from room temperature to near the melting point, and 3) reconstructing temperature-dependent force constant (FC) matrices to obtain group velocity ($\vec{v_g}$). Finally, the chapter delves into a discussion of the implications of simulation parameters and the sensitivity of τ, drawing comparisons to perturbation theory results

4.1 Validating Phonon Gas Model

The temperature-dependent phonon properties of a crystal can be directly evaluated using molecular dynamics (MD) simulated 1-phonon spectra. The underlined assumption is that the phonon gas model remains valid even at high temperatures, i.e. the damp harmonic oscillator theory still holds. As stated previously, either the displacement or velocity auto-correlation function (ACF) can be used to get the 1-phonon spectra. The displacement or velocity must be zero-mean stochastic variables in time while the corresponding ACF should be a superposition of under-damped harmonic oscillators.

The major numerical issue with calculating displacement ACFs in EMD simulations is the reference point to subtract unwrapped position. Ideally, the time-averaged position that an atom oscillates about, and the equilibrium lattice positions should be identical. The displacement will be defined as the distance from the time-averaged position. The displacement and velocity give similar results for the ACF shown in Fig 4.1. Discussed in Chapter 3, the displacement has an error of $O(\Delta t^4)$ while the velocity had an error of $O(\Delta t^2)$ with a timestep of Δt using a Stoermer-Verlet time integration. The remainder of the section will use the velocity ACF by Eq 3.28 for the 1-phonon spectra although either would suffice. The damp harmonic oscillator theory is a classical approach to phonons. At ambient pressure, the Debye temperature of Silicon is roughly 650K, where the quantum effects of lattice vibration are usually negligibly small. Unless specified otherwise, the adopted temperatures in our EMD simulations are 300K, 600K, 900K, 1200K, and 1500K. Except at 300K, our simulations are within the classical regime, where the damped harmonic oscillator theory is a reasonable classical approximation. While we also include 300K in our MD simulation, we are aware that quantum corrections might be needed at this temperature even though the EMD with GAP calculations has been shown to have relatively good agreement to experimental results up to 500K [40]. The highest simulated temperature is 1500K with the melting point of Silicon being around 1700K. Even near melting, the damp harmonic theory holds (Fig 4.2). There is no breakdown of the sm-RTA approximation and should give reliable results even near melting. The peaks are mostly Lorentzian with slightly more noise occurring at 1500K. The anharmonic effects

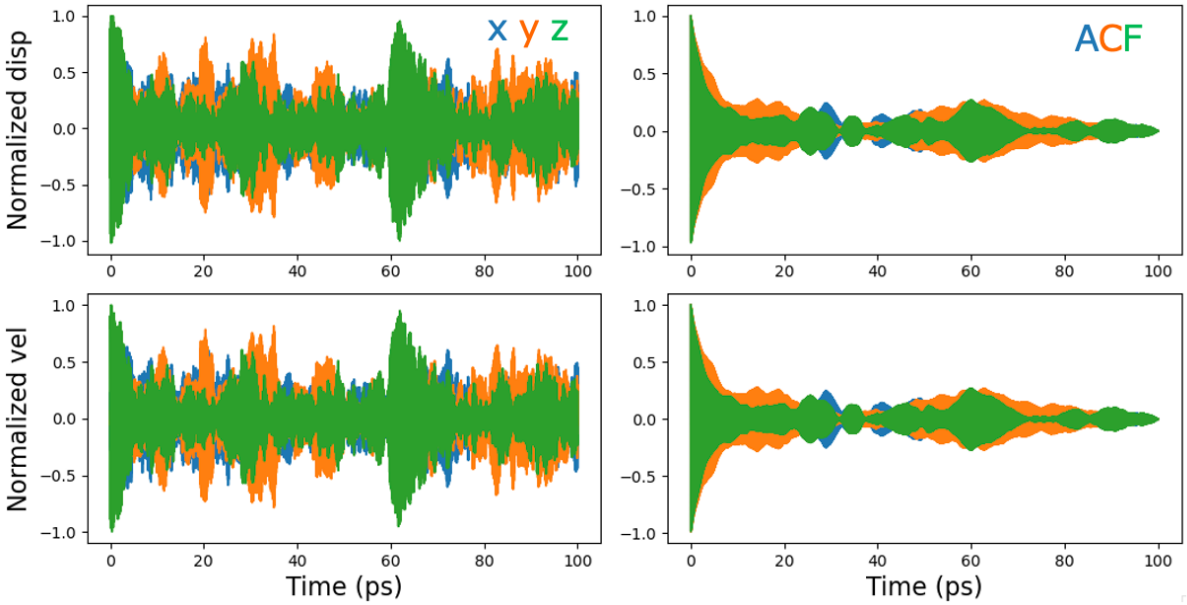

Figure 4.1: The displacement, velocity, and corresponding ACF of the first basis atom at the Γ-point (0,0,0) at 300K of one ensemble

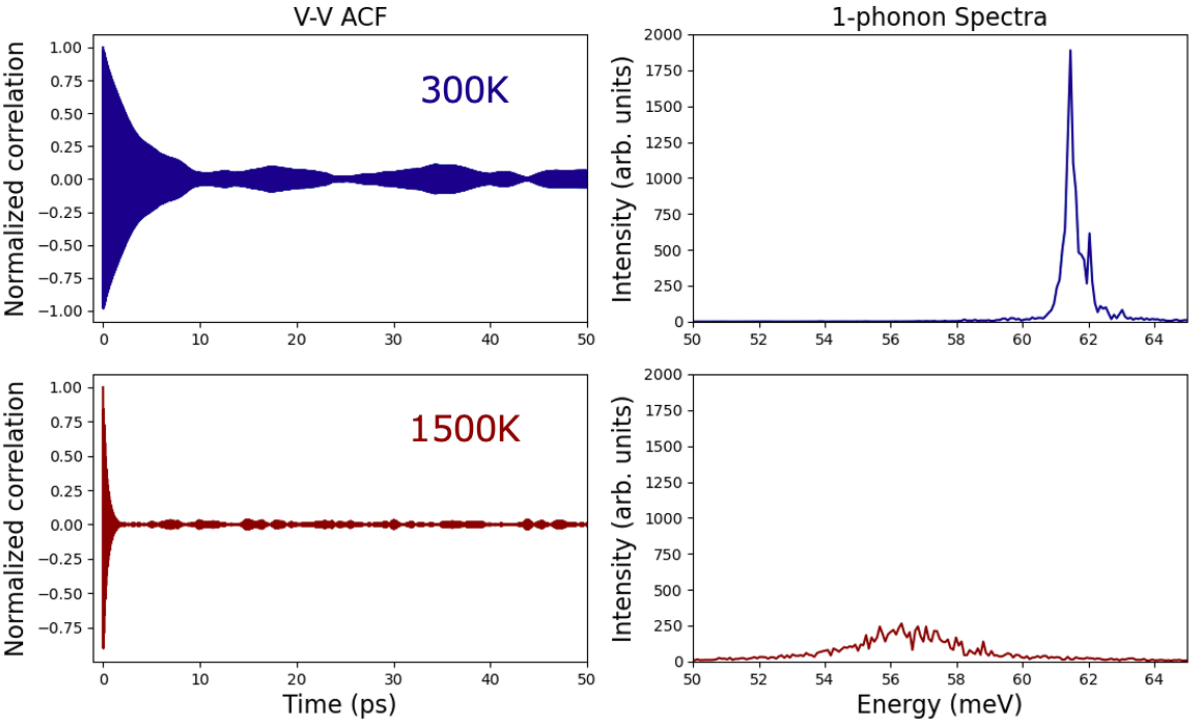

Figure 4.2: Velocity-velocity (v-v) ACF and corresponding Fourier transformation (1-phonon spectra) at 300K and 1500K with the Γ-point

cause the spectra to slightly deviate from the DHO/Lorentzian shape. As expected, the shorter lifetime (quicker decay) in the v-v ACF is inversely proportional to the broadening value of the Lorentzian peak with a frequency downshift with increasing temperatures which occurs for most q-points (excluding L-point). The only option to reduce the noise specifically for the Γ-point is to have more ensembles since it is the zone-center with zero equivalent q-points. Luckily, this point is easy to fit being a single peak while also having a very low impact on the sm-RTA thermal conductivity (discussed later).

4.2 Equivalent q-point Averaging

Typically, the primary numerical noise reduction for MD simulations is averaging over a large number of ensembles. Instead, an average over equivalent q-points can replicate an ensemble average. For particular calculations, equivalent q-points are expected to give similar results so an average over those calculations will reduce the numerical uncertainty. The v-v ACF of equivalent q-points should give identical results by summing over all the basis atoms. Although subtle, splitting the results by q-points enforces $\delta_{q,q'}$ between the ACF and there is no interactions between q-points. This will have a larger implications in the Green-Kubo approach. The shape of the v-v ACF reduces from all commensurate q-points to 85 irreducible q-points. This average can mimic (# of ensembles)$\times$(# of equivalent q-points) for each irreducible q-point with an average equivalent count of 24.

The q-point $\vec{Q} = (\frac{1}{16}, \frac{1}{8}, \frac{3}{16})$ has 3 unique acoustic branches (lower frequency modes) and at most 3 unique optical branches with 24 total equivalent q-points. Shown in Fig 4.3, the equivalent averaging over 4 ensembles greatly reduces the noise in both the DHO and 1-phonon spectrum at 1500K. Parts of the early time-steps of the DHO are smoothed out while there is a stronger decay in the long tail. This ends up effecting both the 3 acoustic branches and optical. The base of the peaks become more smooth and have a more defined Lorentzian shape to it. For the optical modes ($\sim$55 meV range), the amplitude of the wiggles reduces as well.

Another approach to noise reduction is convolution the DHO by multiplying an exponential $e^{-t/\tau_{smooth}}$. While this will reduce the wiggles of the graph, it adds an intrinsic broadening

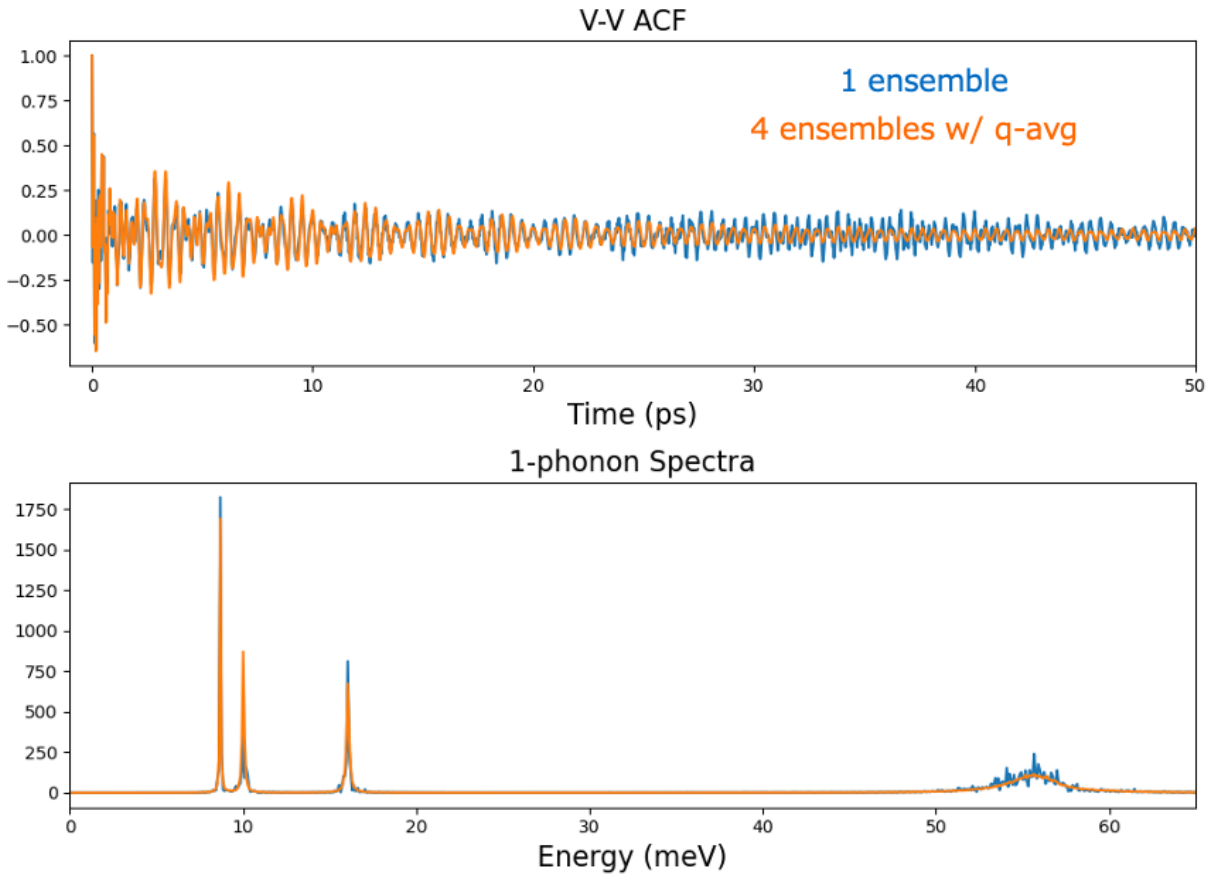

Figure 4.3: v-v ACF (top) and 1-phonon spectra (bottom) of single ensemble vs average of 4 ensembles and q-points equivalent to $\vec{q} = (\frac{1}{16}, \frac{1}{8}, \frac{3}{16})$ at 1500K

to the spectra such that $\frac{1}{\tau_{graph}} = \frac{1}{\tau_{conv}} + \frac{1}{\tau_{true}}$. Methods can be done to de-convolute the intrinsic broadening but the broadening will be shown to be a highly sensitive parameter. Unlike the broadening, the convolution and equivalent averaging has little affect on the peak location. This means that the methodology for extracting the peak locations (frequency), and broadening (or lifetime) should use the least manipulated phonon spectra which the equivalent averaging gives.

4.3 Fitting Algorithm

A fitting algorithm was used to extract the renormalized frequencies and lifetimes from the 1-phonon spectra at every irreducible q-point. A time domain fitting fits a superposition of the DHO equation [48] while a frequency domain fitting fits a superposition of Lorentzian functions. Ideally, an infinitesimally small resolution (or infinitely long run-time) would dictate that both would yield the same results. The time domain resolution is the simulation time-step or 1 fs while a 100 ps run time produces a 50 ps time period correlation functions resulting in a $\frac{1}{50}$THz (0.0825 meV) frequency resolution. Also, any noise or intrinsic broadening from the DHO gets added into the Lorentzian shapes. This means the time domain fitting have more flexibility in the fitting algorithm while also giving less convoluted results by adjusting the range of time to be fitted.

Each averaged irreducible v-v ACF was fitted as a superposition of DHO:

$$\langle v(t)|v(0)\rangle = \sum_{\lambda} W_{\lambda} e^{-g_{\lambda} t}(cos(p_{\lambda} t) - \frac{g_{\lambda}}{p_{\lambda}} sin(p_{\lambda} t)) \tag{4.1}$$

where d_{λ} is the weight of each mode λ, p is the peak location (frequency), and g is the decay constant (half width half max) where $\tau_b = \frac{1}{2g}$. LMFIT, the Non-Linear Least-Squares Minimization and Curve-Fitting python package, was used to fit these equations[35]. LMFIT is a parameter based fitting tool that allows mathematical constraints as well as conditionals to be considered while finding the least error between the fitting parameters and the data. For a particular q-point, a minimum of 18 parameters are needed with a p_{λ}, g_{λ},, and W_{λ} for each 6

λ modes. The constraints and conditionals will invoke necessary physics to the fitting parameters. The following physical constraints: 1) peaks are of ascending order, 2) degenerate peaks have identical fitting parameters, 3) all the weights should sum to 1, and 4) all parameters are non-zero, can be converted to the following equations:

$$\begin{cases} p_{\lambda+1} - p_\lambda > 0 \\ p_\lambda = p_{\lambda'},\ g_\lambda = g_{\lambda'},\ W_\lambda = W_{\lambda'} \quad \text{if degenerate} \\ 1 - \sum_\lambda d_\lambda = 0 \\ p_\lambda > 0,\ g_\lambda > 0,\ W_\lambda > 0 \end{cases} \tag{4.2}$$

Strictly fitting with these conditions with upper bounds of ∞,∞, and 1, for p, g, and d, respectively, a few problems will arise: 1) there is no information on if peaks are degenerate, 2) fitting can take too long without a more confined upper (and lower) bounds, 3) a fitted peak may have a weight that is too small compared to surrounding peaks.

The first issue requires getting insights on degeneracy of peaks. This can be done with the bare phonon frequency. As shown preciously, the bare phonon frequency can be derived from the q-projected FC_2 matrix. Any repeated frequency values will be degenerate and can use the same values as the previous fitting parameter. Since the bare phonon FC_2 is calculated from MD, the frequencies will have some numerical uncertainty. A cutoff of .05 meV was used where any frequencies that are within .05 meV of each other are considered degenerate. This value was chosen based off the general distance between peaks and frequencies of the bare phonon. Having the right number of unique peaks to fit is crucial for both the peak parameter and broadening parameter. With too many peaks, the peaks that are close to each other will have inconsistent peak location and broadening as a function of temperature, especially for the optical branches.Too little peaks will over estimate the broadening values with close peaks forming one large Lorentzian. To counteract this, the bare phonon frequencies are only used for the lowest temperature calculation (300K) and the outputted parameters will be recycled into the 300K fitting until the degeneracy issue is finalized. Then, the 300K degeneracy will be added to the next temperature value.

The upper and lower limits (as well as a good initial guess) help reduce the number of iterations that LMFIT must perform by restricting the allowed parameter values. Although the broadening is highly sensitive, the accuracy of both the peak location and broadening relies on having a good initial guess on the peak location. If the bounds of the peak location is far from the 'true' location, then there will be no ideal broadening and it will be fitted with the largest possible broadening since that will equate to a peak with no impact to the superposition. Because the bare phonon frequency can represent a zero-temperature with infinite lifetime (zero broadening), it can be reasoned the frequency differences between the adjacent temperature runs should be closer than the bare phonon frequencies and 300K frequencies. This means the upper and lower limit set on the lowest temperature range will have to be larger than those of subsequent temperatures. The [upper, lower, guess], and initial guess for 300K are set as the bare phonon frequency $+[2, -3, -0.5]$ meV, respectively, while subsequent temperature takes the previous temperature $+[1.5, -3, -0.5]$ meV.

Lastly, the weights determines the relative heights of all the peaks. Ideally, all peaks should have the same weight or $\frac{1}{6}$ for the size total phonon modes. When only accounting for unique peaks, degenerate peaks will have a weight of $\frac{N_d}{6}$ where N_d is the number of degenerate peaks. In reality, the peaks do not equally distribute the weight. Using a lower bound of half an equally distributed weights, the [upper, lower, guess] for the weights are $[\frac{1}{12}, 1, \frac{1}{6}]$.

After getting fitting parameters for all the temperatures (300K, 600K, 900K, 1200K, 1500K), this process can be done again. Instead of starting with the bare phonon frequencies, the peak locations and broadening for each temperature are now available. In the second run, the [upper, lower, guess] for all temperatures are reduced to that temperature peak location from the first run $+[1.5, -1.5, 0]$. For 300K, the [upper, lower, guess] broadening scales the previous 300K broadening by $[1e^{-1}, 2, 1]$. Other temperatures keeps the same upper limit broadening but changes the [lower, guess] broadening to $[1, 1.5]\times$(previous temperature broadening). With restricted bounds from the first run information, the second run is much quicker and serves to add a physical constraint that broadening increases with temperature $\frac{d\Gamma}{dT} > 0$.

The last issue of peaks having huge discrepancies in the weight comes from the fitting parameter prioritizing the matching the data. Even with reasonable bounds and degeneracy,

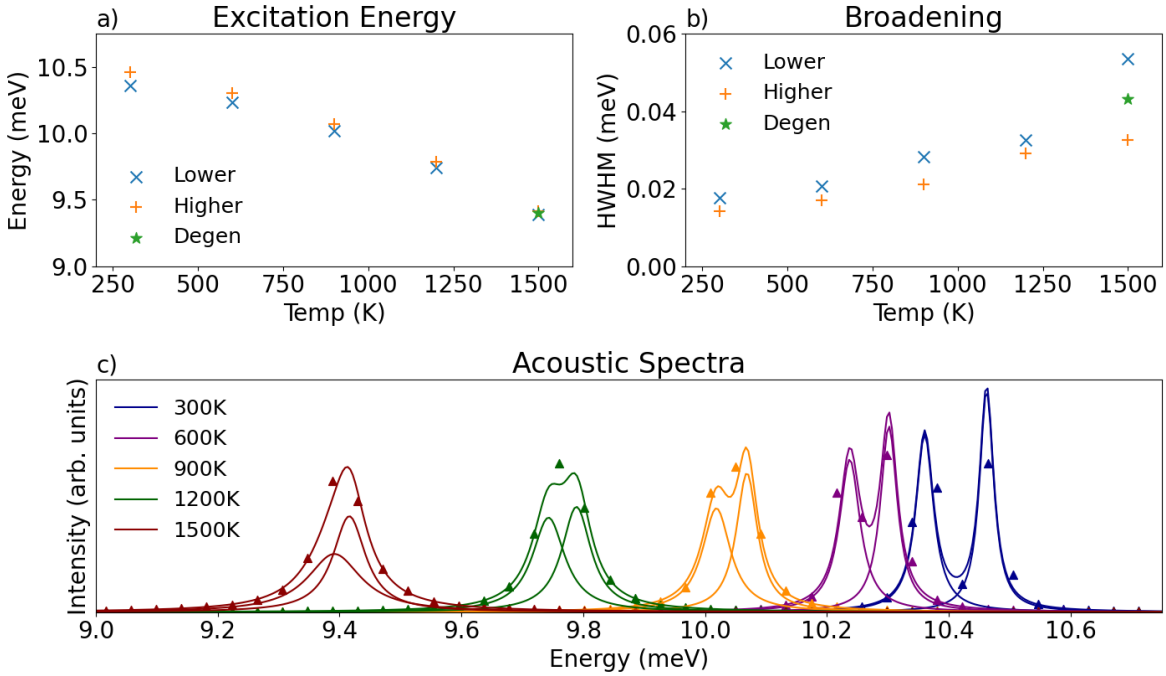

Figure 4.4: a) Energy excitation (frequency), b) half-width half-max broadening, and c) 1-phonon spectra of the neighboring acoustic branches with individual modes from .01 frequency/degeneracy fitting and raw MD spectra (triangle) at various temperatures and $\vec{q} = (\frac{1}{8}, \frac{3}{16}, \frac{3}{16})$

the best fit parameters may come to the conclusion that the fitting is better if one peaks had a much larger importance (weight) than the other. To counter unbalanced distribution, the number of unique weights were independent of the number of unique peaks/broadening. The total unique number of weights were determined by the distance between peaks. Similar to the peak cutoff, the weight cutoff defines the distance between peaks for them to have a unique weight parameter. This forces peaks that are close to each other to have identical weights, thus, no highly unbalanced peak heights with surrounding peaks. Two weight cutoffs were used: one for acoustic branches and another for optical branches with peaks higher than 45 meV being considered optical branches. The acoustic weight cutoff was 1 meV with a slightly higher optical cutoff of 1.5 meV. Although the same weight cutoff could be used, the optical weight had a higher cutoff since the optical branches are less localized.

With this current implementation, an issue will occur with peaks that get too close to either. If peaks start at some distance apart, they may downshift at different rates as a function of

temperature. When the higher peak has a larger downshift, there may be a theoretical crossing of the modes based on the patterns of the frequencies and broadening. A theoretical crossing has an impact on both the frequencies and broadening. This happens more for acoustic branches since they are much closer together but this can also be seen in some optical modes of the irreducible q-points shown in Fig 4.4 c). For the q-point in Fig 4.4, there is a theoretical crossing around 1200K. The final 1500K broadening for the lower mode takes an odd jump compared to the previous temperatures which diverges from the visual pattern of the peaks.

When looking at the 1-phonon spectra, this behavior might be explained with a swapping or 'collision' of modes. The reasoning for swapping comes from the broadening and peak height pattern of the peaks. The right peaks starts higher than the left then looks to decreases at a faster rate than the left. After 1200K, it would reason that the faster decline would lead to the right being lower than the left so the peaks must have swapped locations. With the assumption of swapping, the higher mode (+ on Fig 4.4 b)) broadening would follow an exponential function with the lower mode ($\times$ Fig 4.4 b)) being more linear. If mode swapping is seen as unphysical, then the modes might have 'collided' instead of crossing. An 'elastic' collision may cause the peaks to increase their separation while 'pushing' one of the peaks to a higher broadening value. For some optical branches, the peak increasing peak separation can be seen during a theoretical crossing. With the 'elastic' collision assumption, the swapping can be determined by fitting the peak locations and broadening (with a 2^{nd} order polynomial) and finding with configuration gives the lowest error value. An 'inelastic' collision would mean that the peaks collide then stick together for the rest of the temperatures which will be called 'accidental' degeneracy. With accidental degeneracy enforcement, a new best fit states that the data would fit better as a superposition of degenerate peaks at 1500K instead of two lopsided peaks. Although the frequency does not change much, this causes a noticeable change in the broadening where the accidental degeneracy broadening is in-between the two previous broadening values.

The concept of accidental degeneracy in LMFIT takes the form of an if-else statement constraint:

$$\begin{aligned} \text{if } d_{\lambda+1} < \Delta \rightarrow \text{ then } p_{\lambda+1} &= p_{\lambda} \\ \text{else} \rightarrow p_{\lambda+1} &= p_{\lambda} + d_{\lambda+1} \end{aligned} \tag{4.3}$$

by adding 5 new parameters $d_{\lambda+1} \equiv p_{\lambda+1} - p_{\lambda}$ and Δ is a degeneracy cutoff similar to the frequency cutoff. While fitting, all peak locations are determined by the distance to the previous peak such that p_0 is the lowest reference point. This means that while fitting any peak location after the first $p_{1,2,3,4,5}$ can be replaced with the distances to the previous peak $d_{1,2,3,4,5}$ when determining the best fit. Thus, the total parameters to fit remains unchanged at 18. Then, the actual peak location can be determined with $p_{\lambda+1} = p_{\lambda} + d_{\lambda+1}$

The degeneracy cutoff can vary but it was chosen to be .05 meV to coincide with the frequency cutoff. While iterating, if two peak parameters are within that threshold, the best fitting will be based on a superposition of the lower peak location while the broadening and weights are unchanged. After the best fits are determined and if accidental degeneracy occurs, the fitting will rerun with the new frequencies as inputs to make the broadening degenerate. Both the degeneracy (and frequency) cutoff is an adjustable parameter that can be used to also account for the precision of MD 1-phonon spectra. With the precision of the MD simulation as 0.0825 meV, the 0.05 meV cutoff is slightly less than the resolution of spectra which should not greatly affect the fitted peak broadening. Accidental degeneracy is implemented during the second fitting run with the workflow shown by Fig 4.5

With the best fit parameters of the 1-phonon spectra, each 6 modes in the spectra can be decoupled at each q-point. The temperature dependent spectra, seen in Fig 4.4, are well represented by the decoupled independent modes. The amount of noise from the MD tail is reduced by fitting over the first 20 ps of the v-v ACF. The amount of time can become an adjustable parameter to account for the relative decays per temperature or q-points. Also, the time fitting allows for the DHO to be arbitrarily lengthened prior to Fourier transformation which increases

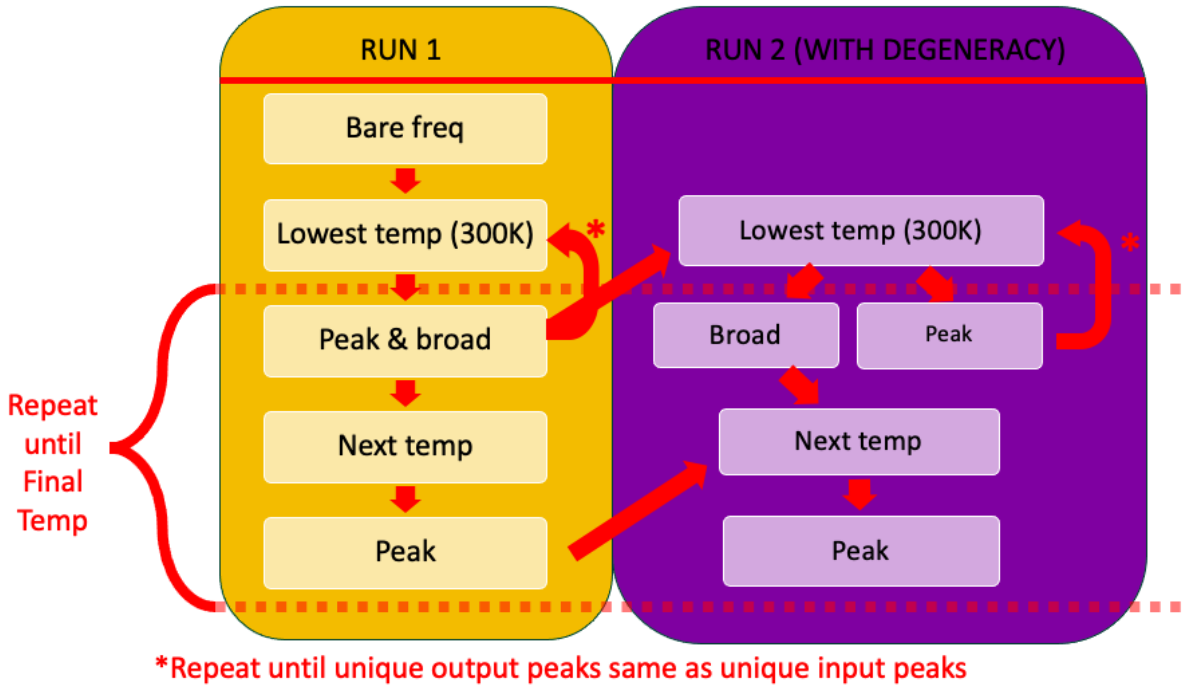

Figure 4.5: Workflow for the fitting algorithm with LMFIT on the 1-phonon spectra

the resolution of the frequency domain. A frequency domain may cause discrepancies with fitting the Lorentzian especially in acoustic peaks yet the lengthened DHO has excellent matches to the sampled points of the raw MD spectra.

4.4 Experimental Comparison

With decoupled modes, the frequencies, lifetimes, dispersion curves, and temperature dependency can be compared to both experimental inelastic neutron scattering (INS) and Raman spectroscopy results. The frequencies and lifetimes are direct outputs of the fitting algorithm while the dispersion can be derived through the eigenvectors and frequency values.

One of the most recent INS data (2020) gives the frequency and lifetime results of various q-points at different of temperatures. [28]. Due to the limited nature of the commensurate q-points, only 1-phonon spectra of the L-point and $\vec{q}_c \equiv (\frac{3}{4}, \frac{1}{4}, \frac{1}{4})$, which is equivalent to $\vec{q} = (\frac{1}{4}, \frac{1}{2}, \frac{1}{2})$, at 300K are available for comparison. From in Fig 4.6, the general peak locations match while the fitted spectra has much lower broadening. The difference in broadening mostly comes from the intrinsic broadening of the experimental equipment. To remove the intrinsic

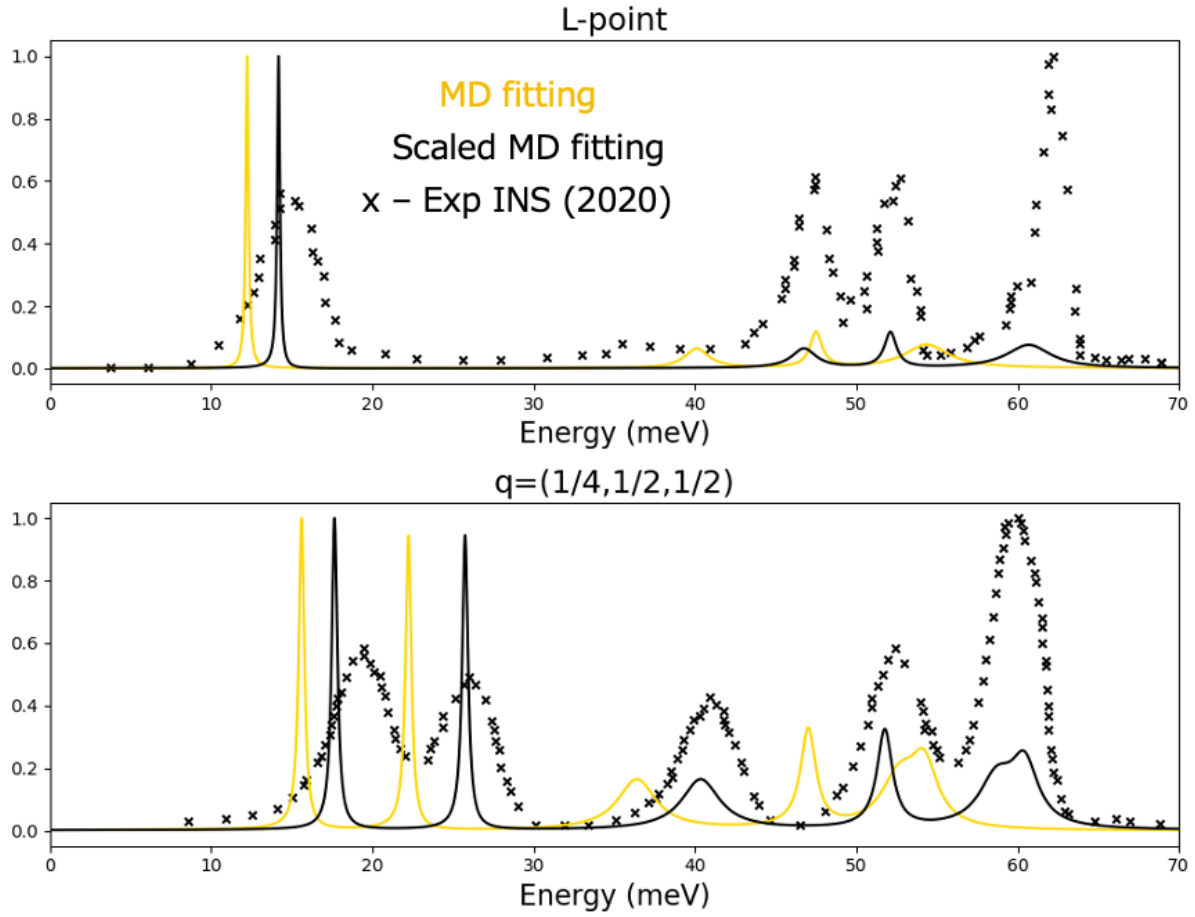

Figure 4.6: Normalized 1-phonon spectra from the fitting algorithm, scaled peaks, and 2020 INS results (top) at the L-point, and (bottom) $\vec{q}_c = (\frac{1}{4}, \frac{1}{2}, \frac{1}{2})$ [28]

broadening, a measurement of the spectra is done at the lowest possible temperature with the assumption that all the broadening at this temperature comes from instrument broadening and subtracting this calibration broadening from higher temperature broadening. For this INS data, this calibration temperature was set to 100K. Even at 100K, the instrument broadening cannot identify the two unique peaks of the highest optical branches at $\vec{q}_c$. This means that when the instrument broadening is greater than the separation distance between peaks, it would be impossible to decouple these peaks without prior information on the peak degeneracy. With the implemented fitting algorithm logic, bare phonon frequency could be used as a 'guess' to the degeneracy prior to fitting and the degeneracy constraint would clarify unique peak number. Afterwards, the subtraction would still be viable assuming that the broadening are additive.

The agreement of the frequencies is dependent multiple factors including the accuracy of the ML potential. Like all potentials, the accuracy depends on the values fitted and interested material properties. The GAP potential is a general purposed potential with quantum accuracy by adding DFT calculations. Any deviations between the type of DFT will translate to the ML potential. Even so, the general patterns and behaviors are captured well while the absolute values may differ. When fitting, the peak locations were fairly rigid especially at lower temperatures due to the localization of the phonon modes. Without having a potential specifically catered to phonons and phonon frequencies, it would be difficult to improve the accuracy of the peak locations in the 1-phonon spectra. These frequency values are within reason to the experimental INS data but it will be shown later that the difference in frequencies will have an impact on the group velocity $\vec{v_g}$ term of the sm-RTA thermal conductivity.

It is possible to improve the frequency locations post-fitting though a boundary condition approach using experimental results. 1963 experimental neutron data by Dolling provides a dispersion curve or frequencies along different q-point paths called band-paths [12]. Band-paths go from one q-point to another with the dispersion curve usually going between high symmetry points. The irreducible commensurate grid samples many of the points on the dispersion curve and their points can be used as a boundary condition. With the help of Dr. Peng Zeng from Auburn University, an iterative methodology was implemented that determined the scale factors between the MD fitting frequencies and experimental frequencies. This iterative method

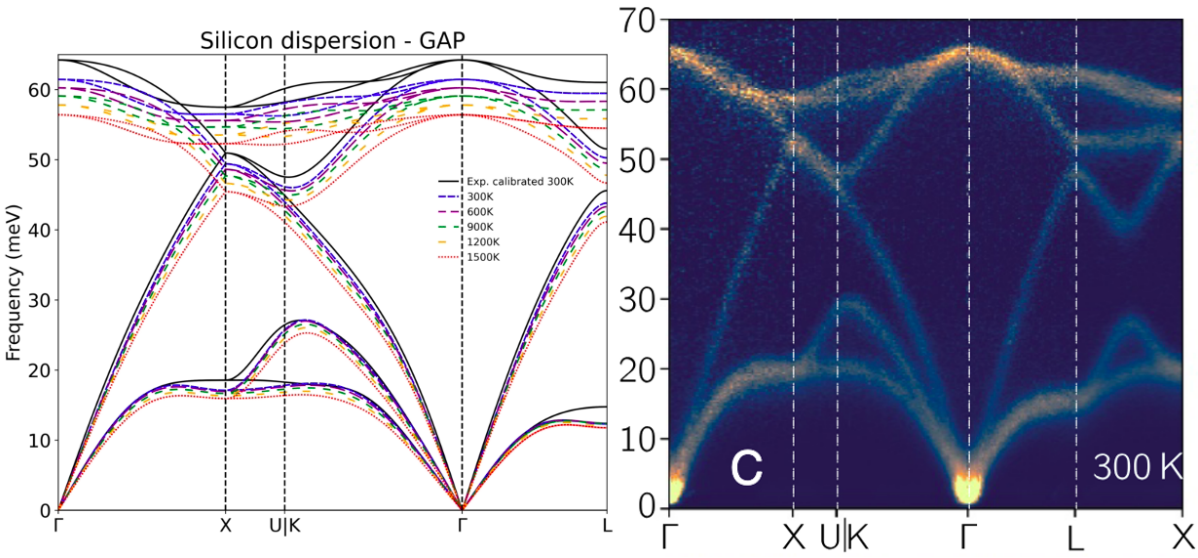

Figure 4.7: Dispersion curve (left) by rebuilding the FC_2 matrix from the fitted peak locations and scaled (experimental calibrated) peak locations, and (right) experimental dispersion curve by INS [27]

uses the known scaled factors and predicts the rest of the irreducible q-point scale factors based on the distance to an unknown q-point scale factor. This scale factors can be folded by out to the entire commensurate grid to give a frequency comparison to other experimental results. With the included scale factor shown in Fig 4.6, the calibrated frequencies have an excellent agreement with more recent (2020) neutron results.

The frequencies from the commensurate grid only provides a discrete dispersion curve. By rebuilding the FC_2 matrix with the help of David Crawford, it is possible to use the fitted frequencies and bare phonon eigenvectors to get a continuous dispersion curve to compare with experimental dispersion curves. By rearranging Eq 2.21, dynamical matrix can be rewritten as $D_{i'j'}(\vec{q}) = \eta_\alpha \omega_\alpha^2 \eta_\alpha^\dagger$ with eigenvectors η_α and eigenvalues ω_α^2 of phonon mode α. The full 4096 atom FC_2 can be rebuilt by combining the dynamical matrix at every commensurate q-point. As shown previously, the full FC_2 can be turned to a dynamical matrix which can be projected to any q-point. Programs like phonopy can enforce symmetry operations and use this projection to create the continuous renormalized dispersion curve of Fig 4.7. The symmetry enforced FC_2 becomes the renormalized FC_2 at that temperature with the diagonalization of this matrix giving the renormalized eigenvalues and eigenvectors. Ideally, the eigenvalues will be

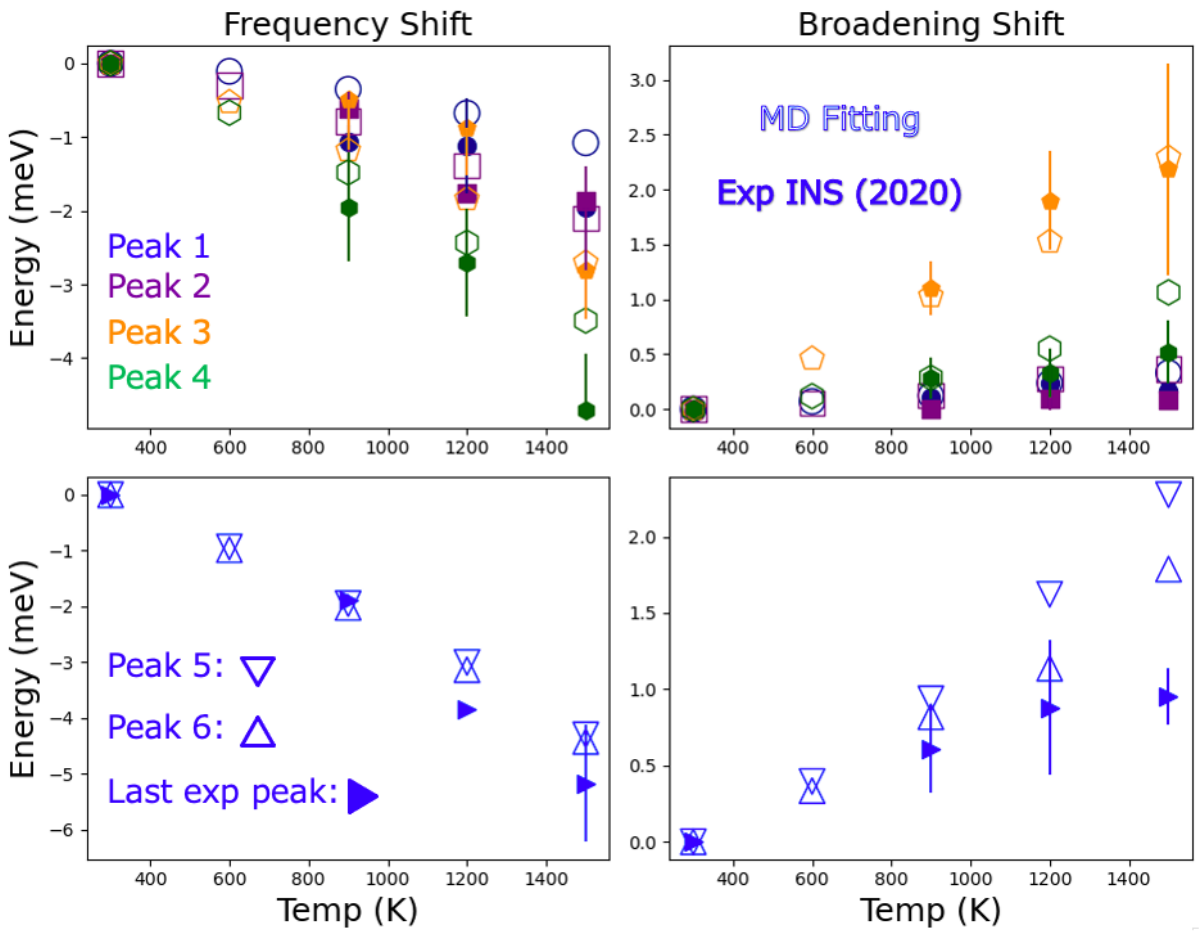

Figure 4.8: Frequency and broadening temperature shifts from 300K of MD fitting and 2020 INS data at $\vec{q}_c = (\frac{1}{4}, \frac{1}{2}, \frac{1}{2})$ [28]

nearly identical to the fitted MD frequencies with new orthogonal eigenvectors. The dispersion curve calibrated with 1964 experimental neutron data has excellent agreement with 2018 INS dispersion curves. The iterative technique mainly corrects the shape of the curve especially the dips around the X-point and L-point. Also, the maximum height (Γ-point) matches better with the calibrated dispersion as compared to the original (blue) dispersion curve at 300K. The maximum frequency shows the contrast of frequencies even between similar experimental procedures so typically, only the frequency (and sometimes broadening) shifts with temperature are used for comparison in both experimental and theoretical results.

To account for the instrument broadening, an INS measurement at 100K is subtracted from the broadening. Comparing the shifted broadening and peak from 300K by Fig 4.8, the MD fitting slightly overestimates the broadening shift while underestimating the frequency shift yet

mostly fall within the range of the error bars in the first 4 peaks. The resolution of the last experimental peak, that combined two optical peaks, has a minor effect on the frequency shifts but no the broadening shift. By fitting, the two highest optical modes become degenerate at 1200K. The conglomerate peaks has a broadening shift of about half of the mean separated peaks shifts. This may arise from the sensitivity of 100K reference broadening since the reference broadening was already comparable to the absolute broadening at higher temperatures. While the peak comparison remains promising, the lifetime comparisons may remain troublesome to compare to INS data without further breakthroughs in resolution or intrinsic broadening. Over convoluted data provides a valuable resource to determine peak locations especially with MD fitting in the frequency (and time) domain while gives major issues for clarifying the broadening/lifetime. Even MD may include intrinsic broadening due to finite size effect and non-harmonic correlation that can be difficult to decouple. The low temperature reference broadening reference point could be implemented into MD calculations of the sm-RTA with either a lower temperature MD simulation or a DFT/experimental reference point.

4.5 sm-RTA Thermal Conductivity

With a renormalized eigenvalues and eigenvectors, the heat capacity c_v is derived by the Eq 2.68 and substituting in the Bose-Einstein distribution while the group velocity $\vec{v_g}$ comes from Eq 2.23 with the renormalized eigenvectors and derivative of the renormalized dynamical matrix. Lastly, with the lifetime τ inversely proportional to the 1-phonon spectra broadening, the impact of c_v, $\vec{v_g}$, and τ on the lattice thermal conductivity $\kappa_{lattice}$ is shown in Fig 4.9. An overall slightly higher frequencies, for the calibrated FC_2 than the original renormalized FC_2 at 300K, translated to both higher heat capacity and group velocity values. While calibration has noticeable change in the frequency shifts, the relative effect on the $\kappa_{lattice}$ is minor. The largest impact on a difference between similar $\kappa_{lattice}$ calculations is the phonon lifetimes τ.

To understand the reasoning behind the low predicted κ_{MD} value (45 $\frac{W}{m-K}$), two perturbation calculations, on a $32 \times 32 \times 32$ mesh grid, were performed to compare the lifetime values. A minimum mesh size of $\sim 11 \times 11 \times 11$ converges the κ results with sufficient irreducible

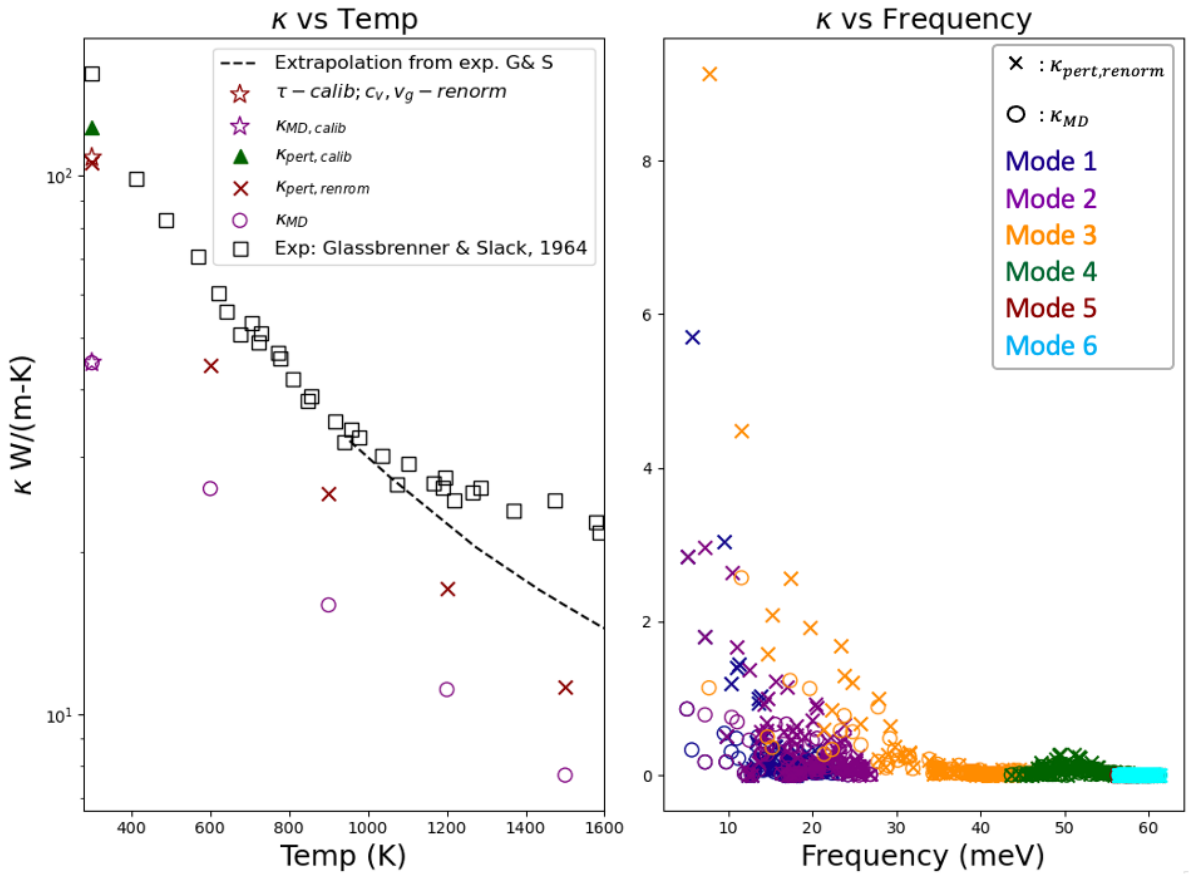

Figure 4.9: Lattice thermal conductivity (left) vs temperature using the sm-RTA approximation with perturbation theory, and MD compared to full thermal conductivity measurements by Glassbrenner & Slack [17] (black square) with an estimated lattice component by extrapolation (dotted line). (right) Contribution to the total lattice thermal conductivity at each irreducible q-point from MD and perturbation theory at 300K.

Thermal conductivity (κ) W/(m-K)			
	Perturbation		MD
300K	125.51 (calibrated)	105.51(renorm)	44.90
600K	44.26		25.11
900K	25.46		15.83
1200K	16.89		10.99
1500K	11.08		7.59

Table 4.1: κ using the 1-phonon spectra and smRTA on the 2048 commensurate grid

q-points. The commensurate grid is a subset of this mesh grid but is not converged. The perturbation calculations requires two force constants to calculated τ at a given temperature with Fermi's golden rule (Eq 2.25) : 1) an FC_2 and FC_3. The third order force constant matrix FC_3 remained unchanged as the bare phonon values while the calibrated and un-calibrated FC_2 were applied for the two calculations, respectively. Calibrated FC_2 are defined as FC_2 rebuilt with the calibrated frequencies $\omega_{calibrated}$ at 300K and temperature dependent shift from MD such that:

$$\omega_{calibrated}(T) = \omega_{300,calibrated} + \omega_{MD,300} - \omega_{MD}(T) \tag{4.4}$$

Table 4.1 is a comparison of the perturbation and MD results at each temperature. The difference in FC_2 frequencies will change the energy values of the delta function in the scattering calculations with $E = \hbar\omega$. The thermal conductivity $\kappa_{pert,calib}$, by the lifetime values from the calibrated perturbated calculations, are 16% higher than the non-calibrated $\kappa_{pert,renorm}$. It is plausible that adjusting the calibrating the ML potential similarly to the frequency calibration will increase the predicted lifetime values without any other available experimental lifetimes for calibration.

The acoustic branches have the highest contribution to κ as they typically have larger group velocities (slope of dispersion curve), and lifetimes. With the same c_v and v_g from the renormalized FC_2 at 300K, most of the underestimation from MD occurs at the acoustic branches with the difference of the 3 highest modes contributions accounting for $\sim$13 $\frac{W}{m-K}$. The lower predicted conductivity translates to a lower predicted lifetime of the acoustic modes as shown in Fig 4.10 (a)-(b). The lower predicted lifetime could arise from an intrinsic broadening of MD, sampling/fitting issues, or stronger anharmonicity (even at 300K).

Two quick solutions can test the impact of any intrinsic broadening similar to experimental instrument broadening. The first solution assumes the peaks are delta functions (of zero broadening) at 0K. The $\frac{1}{T}$ prediction of κ comes from a $\frac{1}{T}$ prediction of τ as a function of temperature. By Matthiessen's rule, the lifetime is approximated as:

$$\tau = \frac{1}{2(\Gamma_{intrinsic} + \Delta\Gamma_{MD,0})} \tag{4.5}$$

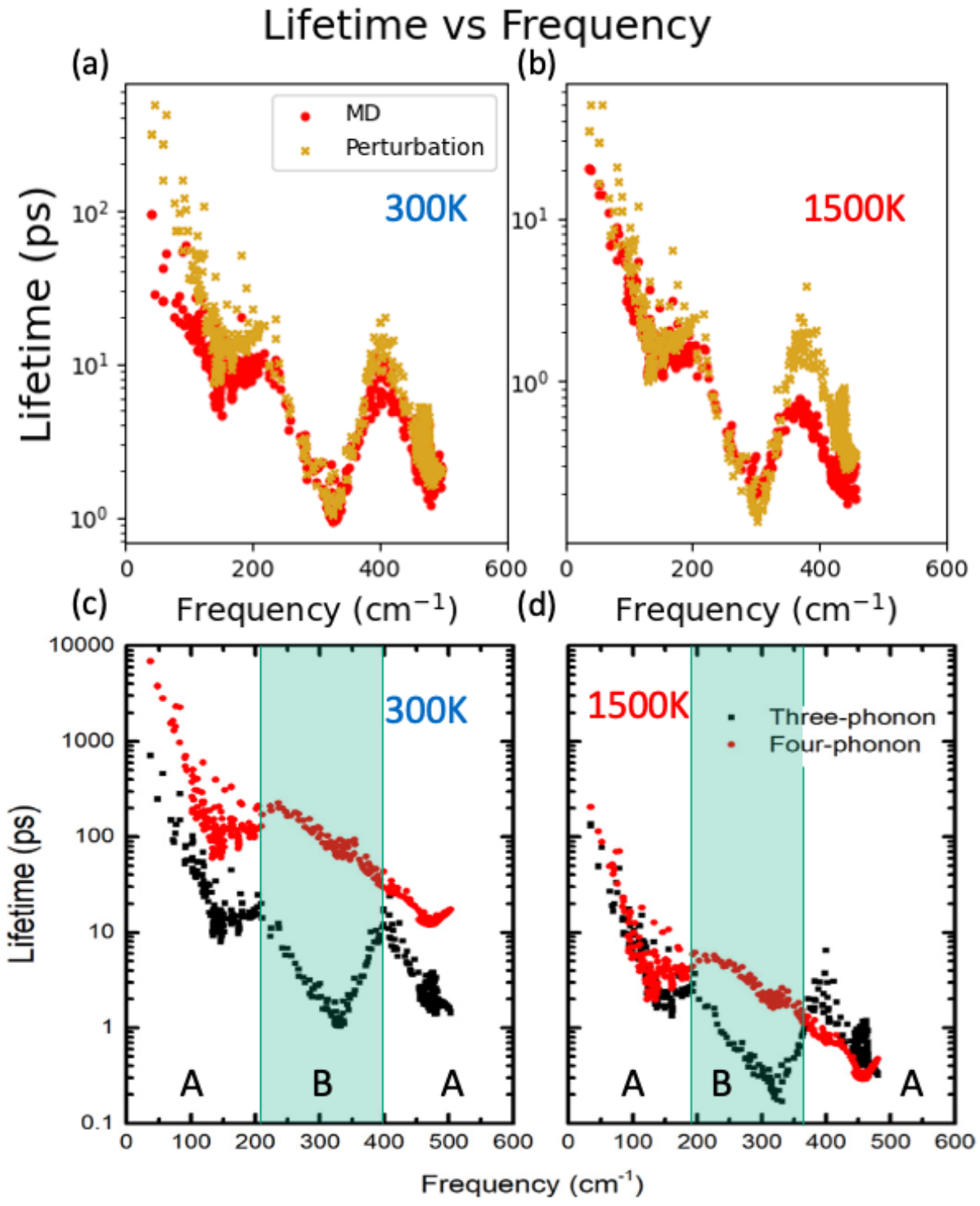

Figure 4.10: Lifetime vs Frequency from MD and perturbation theory (a) at 300K, and (b) 1500K. First principle calculations by Gu et. al. (2020) of 3-phonon and 4-phonon lifetimes (c) at 300K, and (b) 1500K [19]

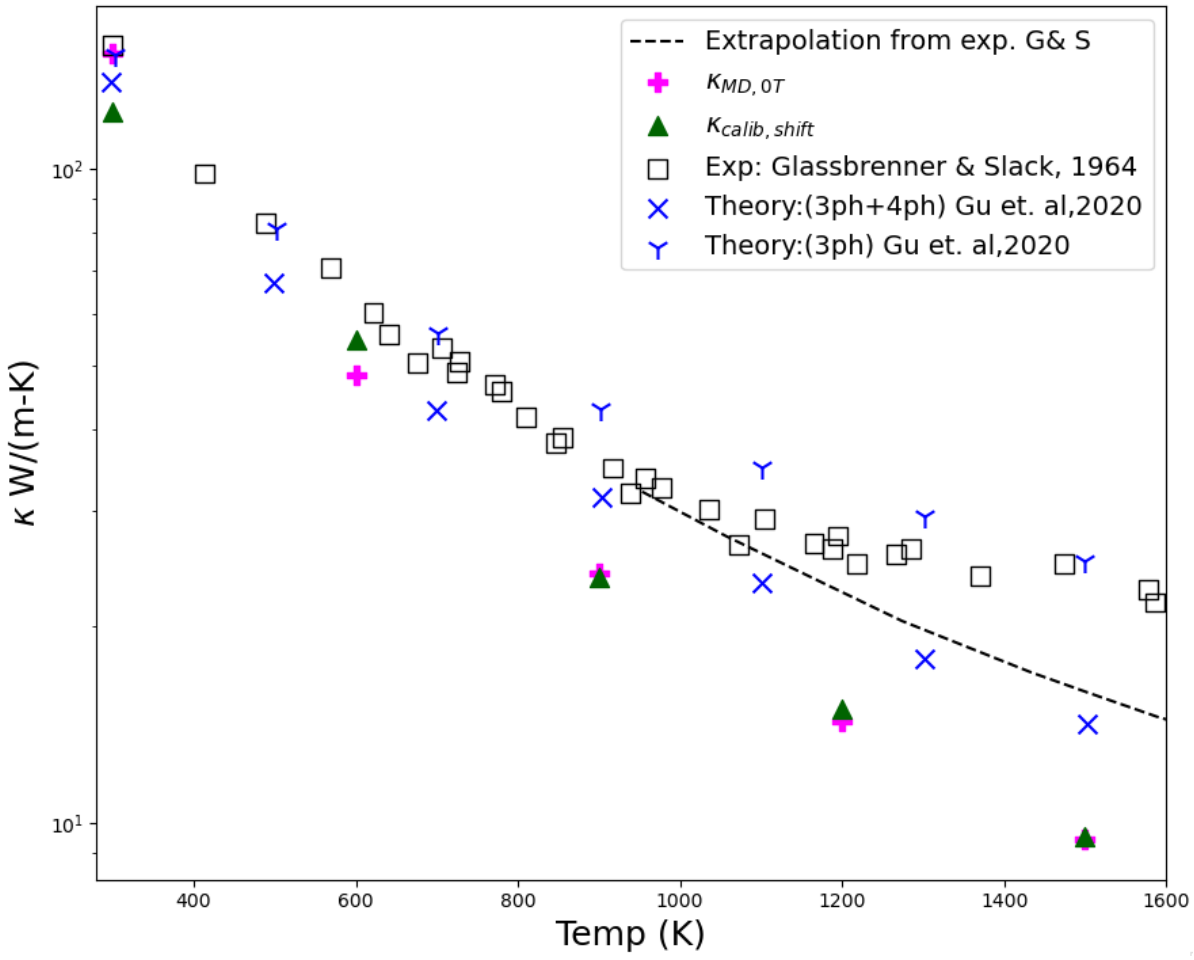

Figure 4.11: Thermal conductivity from (plus) fitting MD lifetimes as a function of temperature and subtracting the constant value, (triangle) adding MD lifetime shift to perturbation theory lifetime, (blue) 3-phonon scattering and 3-phonon plus 4-phonon scattering with first principle calculations presented by Gu et. al. (2020) [19], and (black) experimental measurements by Glassbrenner & Slack [17] with an estimated lattice component by extrapolation (dotted line)

where $\Delta\Gamma_{MD,0}$ is the broadening shift from 0K. Without any rigorous theory to analytically define broadening as a function of temperature, the MD broadening is fitted with a 2^{nd} order polynomial ($AT^2 + BT + C$) as a function of temperature (T). A linear term (B) accounts for the $\frac{1}{T}$ dependence, the quadratic term (A) absorbing any higher order dependence, and the constant term C is the intrinsic broadening. The new lifetime $\tau_{MD,0T}$ becomes:

$$\tau_{MD,0T} = \frac{1}{2(AT^2 + BT)} \tag{4.6}$$

Although a 2^{nd} order polynomial is used as a simplified case, there is no guarantee that any non-linear dependence will not cause a zero broadening prediction at 0K since fitting perturbation broadening gives non-zero constant values with a 2^{nd} order polynomial for certain modes especially those around $\sim$ 40 meV. A more reasonable equation could be used by finding a broadening equation that gives a similar line shape to κ/τ when taking the reciprocal of said equation.

The other quick solution assumes that the MD broadening shifts captures broadening shifts but not the absolute value. Using the perturbation theory lifetimes with the calibrated FC_2 at 300K as a reference point, a new lifetime is calculated by adding the MD broadening shift from 300K, $\Delta\Gamma_{MD,300}$, to the perturbation broadening from the calibrated FC_2 at 300K, $\Gamma_{calib,300}$, such that:

$$\tau_{calib,shift} = \frac{1}{2(\Gamma_{calib,300} + \Delta\Gamma_{MD,300})} \tag{4.7}$$

The thermal conductivity by the first approach, $\kappa_{MD,0T}$, is $\sim$ 150 W/(m-K) at 300K and much closer to the experimental results than the perturbation results at 300K shown in Fig 4.11. As temperature increases, both $\kappa_{MD,0T}$ and $\kappa_{calib,shift}$ converge to the same result of $\sim$ 10 W/(m-K) at 1500K. Both are in-between the previously predicted 1500K MD prediction κ_{MD} and perturbation prediction $\kappa_{pert,renorm}$ in Fig 4.9 while also being far below the extrapolated $\kappa_{lattice}$ prediction.

These quick solutions proves that not only does MD predicted a lower thermal conductivity at each temperature but also predicts an overall larger broadening shifts (especially for high κ contribution modes). First principle calculations were done by Gu et. al. [19] to examine the

contribution of 4-phonon scattering on κ. The phonon lifetime was decomposed as:

$$\frac{1}{\tau_{phonon}} = \frac{1}{\tau_{3-phonon}} + \frac{1}{\tau_{4-phonon}} \tag{4.8}$$

or:

$$\tau_{phonon} = \frac{1}{\frac{1}{\tau_{3-phonon}} + \frac{1}{\tau_{4-phonon}}} \tag{4.9}$$

where the 3-phonon and 4-phonon lifetimes are calculated by Fermi's golden rule (Eq 2.25) with the FC_3 and FC_4, respectively. By Fig 4.10, the 4-phonon lifetimes were about an order of magnitude higher than the 3-phonon lifetimes at a given frequency at 300K but comparable at 1500K at all frequencies except the region B on Fig 4.10 (the 200-350 cm^{-1} or 24.6-43.2 meV range). This means that the 3-phonon lifetime was the dominant factor at 300K at all frequencies and region B at 1500K. The full phonon lifetime would be $\sim \frac{1}{2}$ the predicted lifetime if only 3-phonon scattering was considered. With κ_{MD} being $\sim \frac{1}{3} \kappa_{pert,renorm}$ at 300K, MD either predicts a larger 4-phonon contribution to the lifetime, 5+-phonon scattering, or possible sampling issues with the lifetime. At 1500K, the thermal conductivity results by Gu et. al. [19] with only 3-phonon and 4-phonon scattering approaches the extrapolated thermal conductivity [17] while the original κ_{MD} is about half that value. This would mean that the MD lifetime may have another lifetime (possibly 5+-phonon) that is comparable to both the 3-phonon and 4-phonon lifetime at higher temperatures.

Possible sampling issues would come from the total correlation time. The 100 ps run-time gives a 50 ps correlation time with a .08 meV frequency resolution. When plotting the DHO fitting, the time was extended by an order of magnitude to display smooth Lorentzian functions in the 1-phonon spectra. The first 20 ps of the correlation function is fitted to not include the end tail 'noise'. This means that any lifetime where $\tau >> 20$ ps (mostly the acoustic branches) may not be properly sampled in the correlation fitting. Although the fitting showed great representation of the raw MD data in the frequency regime, a singular longer run that is an order of magnitude longer ($\sim$1 ns or 1,000,00 fs) could be done to clarify if the fitting captures the high lifetime acoustic modes. Since anharmonicity rises with temperature, any anharmonicity higher than the 4^{th} order would be negligible at 300K meaning the predicted

lifetimes are expected to be similar to the pattern seen at 1500K for the high lifetime acoustic modes in Fig 4.10 (b). If a longer run would fix this issue, then that 300K MD simulation could be used as the reference lifetime and create new predictions similar to the methodology for $\kappa_{calib,shift}$. The validity of the predicted τ_{MD} will be expanded upon in the next chapter by comparing the sm-RTA results to the heat flux ACF calculations.

4.6 Conclusions

In conclusion, our novel algorithm, incorporating enforced q-point symmetry and accounting for "accidental" degeneracy, has proven to be a numerically robust and efficient method for extracting temperature-dependent phonon properties, specifically frequency (ω), lifetime (τ), and group velocity ($\vec{v_g}$), from molecular dynamics (MD) simulations. We have convincingly demonstrated the robust predictive capability of our MD methods in capturing phonon frequency renormalization even at very high temperatures. However, our findings underscore the high sensitivity of τ for low-frequency (small wave numbers) acoustic phonons to numeric artifacts in MD simulations, significantly impacting the accuracy of lattice thermal conductivity (κ_L) predictions.

In light of these observations, we recommend two avenues for future research. Firstly, extending simulation times beyond the duration employed in this study (100 ps) would enhance our understanding of the convergence of numerically evaluated τ for low-frequency acoustic modes at different temperatures. Secondly, we advocate for a mixed approach involving perturbative calculations for these modes with large τ, while τ for other phonon modes is directly simulated using MD. The intricacies of this proposed hybrid methodology, combining MD and perturbation theory, should be thoroughly developed to efficiently predict κ_L

Chapter 5

Second-Order Heat Flux $J_{2,lattice}$

The kinetic phonon transport theory, as discussed in Chapter 4, is known for a notable limitation tied to its reliance on the Peierls' heat flux model of phonons, $\vec{J} = \sum_\lambda f_\lambda \hbar \omega_\lambda \vec{v_g}_\lambda$. As previously discussed by various researchers, such as Hardy in 1963, Peierls' model serves as merely a first-order approximation of the total lattice heat flux. This approximation incorporates the intra-mode phonon contribution to the heat flux associated with the harmonic force constant FC2. According to Hardy, the second-order Hardy heat flux, $\vec{J}_{2,lattice}$, when projected into q-space, comprises two distinct components: the intra-phonon-mode and the inter-phonon-mode part. Notably, the former aligns precisely with Peierls' term.

Recent studies have introduced novel unified theories aiming to individually account for contributions to total lattice thermal conductivity (κ_L) from inter-model and intra-mode interactions. However, the interaction between intra-mode $\vec{J}_{2,lattice}$ and inter-mode $\vec{J}_{2,lattice}$ has been largely overlooked without adequate justification. A significant numerical challenge in quantitatively determining the individual contributions of various factors to total κ_L stems from numeric fluctuations resulting from interactions between different q-points. Our study is carried out under the hypothesis that the averaged interaction contribution between distinct q-points is close to zero. We have verified that the implementation based on $\delta(\vec{q} - |\vec{q}|)$ proves to be pivotal in addressing the ensemble issue of Green-Kubo (G-K) thermal conductivity. While Sun & Allen associate this enforcement with the elimination of "vertex corrections" [47], this chapter aims to affirm the validity of this omission.

With our algorithm, we can quantitatively calculate self-correlation functions of intra-mode $\vec{J}_{2,lattice}$, self-correlation functions of inter-mode $\vec{J}_{2,lattice}$, and cross-correlation functions

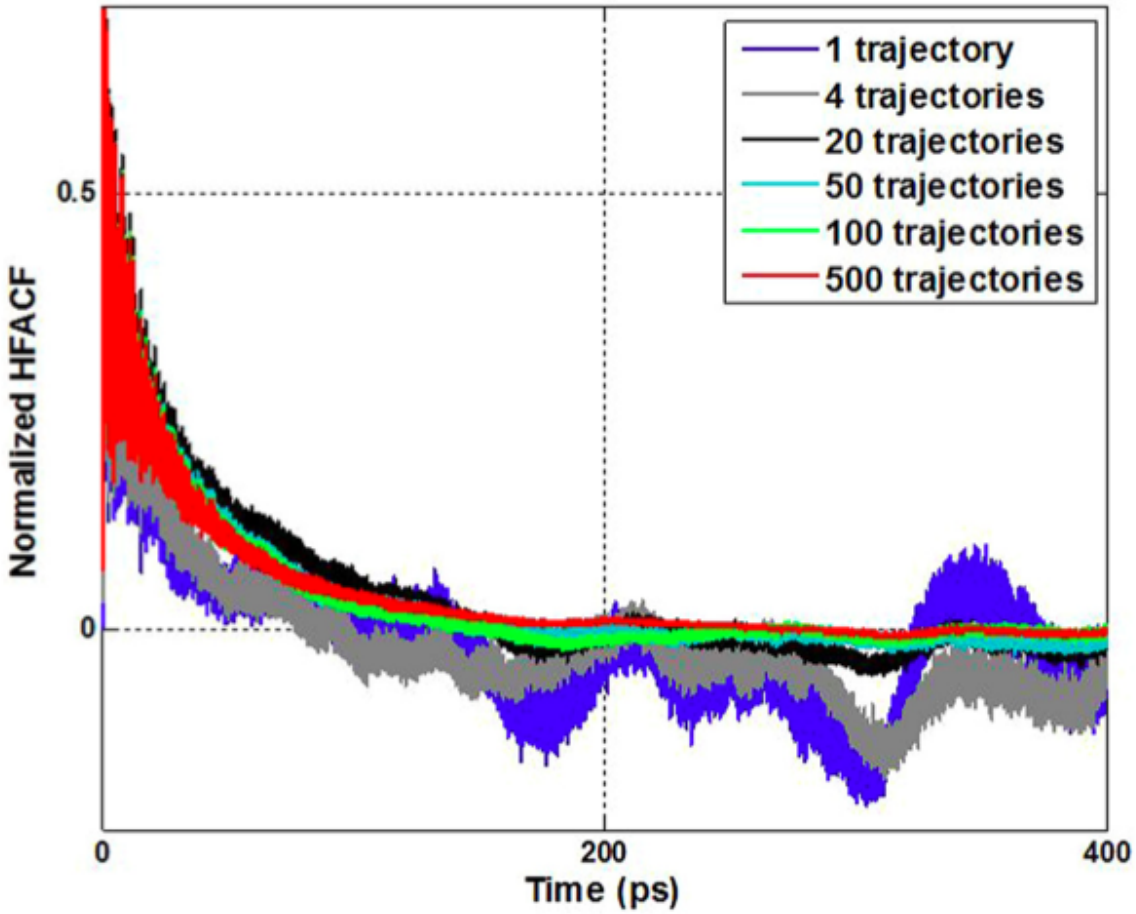

Figure 5.1: Gordiz et. al. [18] Heat flux ACF (HFACF) calculations at 300K with LAMMPS simulations of 500 atoms, 800 ps runtime (or 400 ps correlation time), and Tersoff potential. Trajectories are the number of ensembles.

between inter-mode $\vec{J}_{2,lattice}$ and intra-mode $\vec{J}_{2,lattice}$. The contribution to κ_L from this cross-correlation has not yet been reported in the existing literature.

5.1 Real Space vs Q-space

The main downside of the Green-Kubo formalism (G-K):

$$\kappa = \frac{V}{k_b T^2} \int_0^\infty \langle \vec{J}(t) | \vec{J}^*(0) \rangle dt \tag{5.1}$$

is the integral not converging without averaging over a large number of ensembles. Because G-K requires an integration over the correlation function, the uncertainty of the thermal conductivity κ is a direct result of the oscillations and time of integration. The heat flux ACF (HFACF) calculated by Gordiz et al. (Fig 5.1) shows that a minimum of $\sim$100 ensembles is needed to have a reliable convergence when ensemble averaging is implemented. The correlation function must be as smooth as possible for the integration to saturate over time. Ensemble averages with small sets (1, 4, and, 20) either decay too early or oscillate about zero which halts the increase of the integration and lowers the predicted κ. Gordiz et al. predicts a thermal conductivity of 183 W/(m-K) with only a correlation time of 400 ps [18]. Discussed later, an optimal simulation time could be determined for efficiency at higher temperatures.

The real space $J_{2,lattice}$ can be defined as a summation over the commensurate grid N_q:

$$J_{2,lattice} = \frac{1}{\sqrt{N_q}} \sum_{\vec{q}} \vec{J_{\vec{q}}} \tag{5.2}$$

where:

$$\vec{J_{\vec{q}}} = \frac{1}{2mV} \sum_{ij} \sum_{\alpha\beta} \vec{\nabla}_{\vec{q}} A_{i\alpha,j\beta}(\vec{q}) Q_{j\beta}(\vec{q}) P^*_{i\alpha}(\vec{q}) \tag{5.3}$$

By Fig 5.2 a), real space $J_{2,lattice}$ of one ensemble followed the trends of the low ensemble (trajectories) averages of Fig 5.1 with large oscillations that prevent the G-K integral from converging. Also, the x,y, and z components of the G-K had a standard deviation of 85.71 W/(m-K) (or 79.71 W/(m-K) without zero-padding) at 300K, which a larger ensemble average should reduce.

Typically, a simulation time produces a correlation function of half the simulation time (due to periodicity forwards and backwards in time). A technique implemented in correlation functions (especially signal processing) involves padding the end of the signal with extra zeros to lengthen it and can give an artificial correlation function beyond the half the simulation time. Without zero padding, the true correlation function (of half the simulation time) is the truncation of the zero padded correlation function. As seen in Fig 5.2 b), zero-padding can

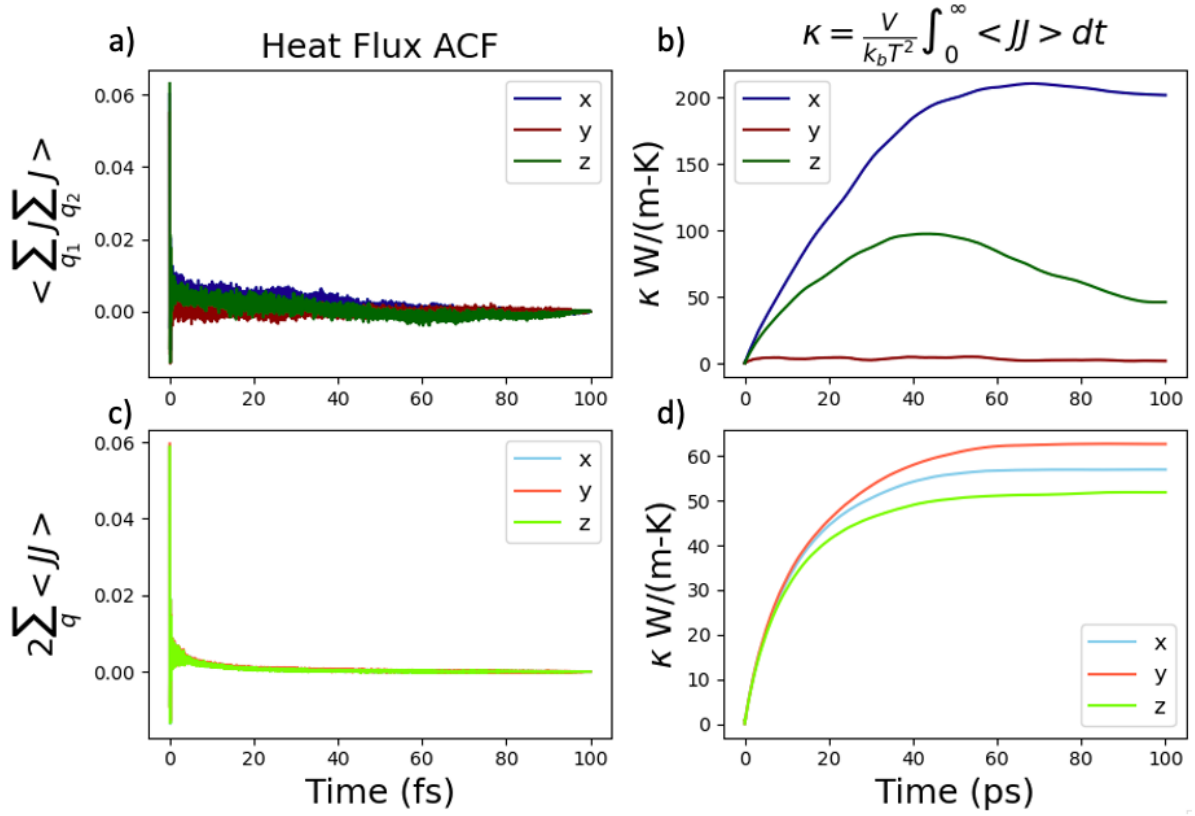

Figure 5.2: a) Real space $J_{2,lattice}$ HFACF and b) corresponding G-K integration at 300K. c) $J_{2,lattice}$ HFACF with enforcement of $\delta(\vec{q} - |\vec{q}'|)$ between q-points and d) corresponding G-K integration at 300K. Results beyond 50,000 fs (50 ps) are zero-padded. All correlation graphs are scaled by the G-K integration factor $\frac{Vdt}{T^2}$ so the integral directly computes thermal conductivity

hurt the predicted value of the integration if the HFACF is already oscillating about zero (z-direction) or improve the predictions where the decay is much slower than the oscillations (x-direction). The latter will be shown to make zero-padding useful after greatly reducing the oscillations by enforcing no cross q-point interactions $\delta_{q,q'}$. All graphed HFACF above 50 ps (or 50,000 fs) are zero-padded results.

The enforcement of $\delta_{q,q'}$ can be explained by looking at the HFACF $\langle \vec{J}\vec{J}^* \rangle_{\vec{q}_1,\vec{q}_2,\vec{q}_3,\vec{q}_4}$ between 4 q-points, $\vec{q}_1$ $\vec{q}_2$, $\vec{q}_3$, and $\vec{q}_4$, where $\vec{q}_1 = -\vec{q}_2$, and $\vec{q}_3 = -\vec{q}_4$. By expanding the correlation:

$$\begin{aligned}
\langle \vec{J}\vec{J}^* \rangle_{\vec{q}_1,\vec{q}_2,\vec{q}_3,\vec{q}_4} &= \langle \sum_{\vec{q}_1 \dots \vec{q}_4} \vec{J}_{\vec{q}} | \sum_{\vec{q}_1 \dots \vec{q}_4} \vec{J}^*_{\vec{q}} \rangle \\
&= \langle \vec{J}_{\vec{q}_1} + \vec{J}_{\vec{q}_2} + \vec{J}_{\vec{q}_3} + \vec{J}_{\vec{q}_4} | \vec{J}^*_{\vec{q}_1} + \vec{J}^*_{\vec{q}_2} + \vec{J}^*_{\vec{q}_3} + \vec{J}^*_{\vec{q}_4} \rangle \\
&= \langle \vec{J}_{\vec{q}_1} + \vec{J}_{\vec{q}_2} | \vec{J}^*_{\vec{q}_1} + \vec{J}^*_{\vec{q}_2} \rangle + \langle \vec{J}_{\vec{q}_3} + \vec{J}_{\vec{q}_4} | \vec{J}^*_{\vec{q}_3} + \vec{J}^*_{\vec{q}_4} \rangle \\
&\quad + \langle \vec{J}_{\vec{q}_1} + \vec{J}_{\vec{q}_2} | \vec{J}^*_{\vec{q}_3} + \vec{J}^*_{\vec{q}_4} \rangle + \langle \vec{J}_{\vec{q}_3} + \vec{J}_{\vec{q}_4} | \vec{J}^*_{\vec{q}_1} + \vec{J}^*_{\vec{q}_2} \rangle
\end{aligned} \tag{5.4}$$

By the definition of the heat flux, $\vec{J}_{\vec{q}} = \vec{J}^*_{-\vec{q}}$ with the summation over a grid with both $\vec{q}$ and $-\vec{q}$ only leaving a real component $2\text{Re}(\vec{J}_{\vec{q}})$. With this, Eq 5.4 becomes:

$$\begin{aligned}
\langle \vec{J}\vec{J}^* \rangle_{\vec{q}_1,\vec{q}_2,\vec{q}_3,\vec{q}_4} &= \langle 2\text{Re}(\vec{J}_{\vec{q}_1}) | 2\text{Re}(\vec{J}_{\vec{q}_1}) \rangle + \langle 2\text{Re}(\vec{J}_{\vec{q}_3}) | 2\text{Re}(\vec{J}_{\vec{q}_3}) \rangle \\
&\quad + \langle \vec{J}_{\vec{q}_1} + \vec{J}_{\vec{q}_2} | \vec{J}^*_{\vec{q}_3} + \vec{J}^*_{\vec{q}_4} \rangle + \langle \vec{J}_{\vec{q}_3} + \vec{J}_{\vec{q}_4} | \vec{J}^*_{\vec{q}_1} + \vec{J}^*_{\vec{q}_2} \rangle
\end{aligned} \tag{5.5}$$

This demonstrates that the heat flux at $\vec{q}$ and $-\vec{q}$ can correlate with each other while all other cross-terms are assumed to be zero meaning:

$$\begin{aligned}
\langle \vec{J}\vec{J}^* \rangle &= \langle \sum_{\vec{q}} \vec{J}_{\vec{q}} | \sum_{\vec{q}'} \vec{J}^*_{\vec{q}'} \rangle \delta(\vec{q} - |\vec{q}'|) \\
&= 2 \sum_{\vec{q}} \langle \vec{J}_{\vec{q}} | \vec{J}^*_{\vec{q}} \rangle
\end{aligned} \tag{5.6}$$

The even-numbered commensurate grid, which samples the Γ-point, is not a symmetric grid as the boundary points do not have a negative component. A new odd-numbered symmetric grid could be produced by adding points to all the boundary points to include both 0.5 and -0.5 while the total irreducible q-points remains the same. Although this fixes the symmetry, the new grid has little effect on the HFACF as the new boundary points contribute less than the near zone-centered q-points while increasing the grid size N_q in Eq 5.2.

With Eq 5.6, the G-K integration of the HFACF in the x-, y-, and z-direction have an improved standard deviation of 4.41 W/(m-K) at 300K. Zero-padding the correlation improves

the results here (beyond 50 ps) since the HFACF has a smooth decay with no low frequency oscillations. This cross-term enforcement HFACF resembles the 500 ensemble HFACF (by Gu et. al. in Fig 5.1[18]) with only one ensemble without considering the relative decay lifetime. As a result, ensembles can be used to refine the final value instead of a requirement to reduce numerical uncertainty for convergence.

5.2 Intra-mode Heat Flux

As discussed previously, $\vec{J}_{2,diagonal}$ reduces to the Peris heat flux ($\vec{J}_{rta} \equiv \sum_\lambda \Delta f_{\lambda,rta} \hbar\omega_\lambda \vec{v_g}_\lambda$) using raising and lowering operators. Both currents should be match if the fitted lifetime is true to the 1-phonon spectra. The diagonal heat flux $\vec{J}_{2,diagonal}$ is defined as the heat flux from a dynamical matrix with the derivative having no cross mode components ($\vec{\nabla}_{\vec{q}} D(\vec{q})_{\lambda\lambda'} = 0$ if $\lambda \neq \lambda'$). This diagonal derivative $\vec{\nabla}_{\vec{q}} D^{diag}_{i\alpha,j\beta}(\vec{q})$ is a summation of modes λ such that:

$$\vec{\nabla}_{\vec{q}} D^{diag}_{i\alpha,j\beta}(\vec{q}) = \sum_\lambda 2\omega_\lambda \vec{v_g}_\lambda e^*_{i\alpha}(\vec{q},\lambda) e_{j\beta}(\vec{q},\lambda) \tag{5.7}$$

where $e_{i\alpha}$ is the eigenvector of the i-th basis atom in the α-direction and $2\omega_\lambda \vec{v_g}_\lambda$ is the expectation value of the dynamical matrix derivative:

$$2\omega_\lambda \vec{v_g}_\lambda = \langle e_{i\alpha}(\vec{q},\lambda) | \vec{\nabla}_{\vec{q}} D(\vec{q})_\lambda | e_{j\beta}(\vec{q},\lambda) \rangle \tag{5.8}$$

Substituting these terms into the diagonal heat flux,:

$$\vec{J}_{2,diagonal} = \frac{1}{2V} \sum_{ij} \sum_{\alpha\beta} \sum_{\vec{q}} \vec{\nabla}_{\vec{q}} D^{diag}_{i\alpha,j\beta}(\vec{q}) Q_\beta(\vec{q}) P^*_\alpha(\vec{q}) \tag{5.9}$$

The HFACF with $\vec{J}_{rta}$ is:

$$\langle \vec{J}_{rta} | \vec{J}_{rta} \rangle = \sum_{\lambda,\lambda'} \langle \hbar\omega_\lambda \vec{v_g}_\lambda \Delta f_\lambda(t) | \hbar\omega_{\lambda'} \vec{v_g}_{\lambda'} \Delta f_{\lambda'}(0) \rangle \tag{5.10}$$

By orthogonality, the group velocity ($\vec{v_g}$), frequency (ω), and change in probability density (Δf) is assumed to have no cross mode correlations. Thus, Eq 5.10 reduces to:

$$\langle \vec{J}_{rta} | \vec{J}_{rta} \rangle = \sum_{\lambda} (\hbar \omega_{\lambda} \vec{v_g}_{\lambda})^2 \langle \Delta f_{\lambda}(t) | \Delta f_{\lambda}(0) \rangle \tag{5.11}$$

The change of probability distribution correlation $\langle \Delta f_{\lambda}(t) | \Delta f_{\lambda}(0) \rangle$ has a maximum value at $t = 0$ of $\frac{k_B T^2 c_{v,\lambda}}{(\hbar \omega_{\lambda})^2}$, then decays exponentially based on the phonon lifetime τ_{λ}. The HFACF with the Peris heat flux becomes:

$$\langle \vec{J}_{rta} | \vec{J}_{rta} \rangle = \sum_{\lambda} \vec{v_g}_{\lambda}^{\,2} k_B T^2 c_{v,\lambda} e^{-t/\tau_{\lambda}} \tag{5.12}$$

with the thermal conductivity κ_{rta} with G-K as:

$$\kappa_{rta}(\vec{q}) = \frac{1}{V} \sum_{\lambda} c_{v,\lambda} \vec{v_g}_{\lambda}^{\,2} \int_0^{\infty} e^{-t/\tau_{\lambda}} dt \tag{5.13}$$

where:

$$\lim_{t \to \infty} \int_0^{\infty} e^{-t/\tau} dt = \tau \tag{5.14}$$

For both heat flux to be equivalent, the $t = 0$ HFACF should be identical but by Fig 5.3 not only does the initial correlation not match but the selected FC_2 matrix has a larger impact on the initial value. Previously with the smRTA, the calibrated and renormalized FC_2 made negligible change when using the same lifetime values. The thermal conductivity using G-K, κ_{G-K}, predicted higher values at all temperatures seen in Table 5.1 even though it had lower predicted mode contributions at some high contributing q-points seen in Fig 5.4. The calibrated FC_2 increases the κ by $\sim$10% has compared to the renormalized FC_2 and $\sim$30% to the smRTA with MD 1-phonon spectra at both 300K and 1500K. Normalizing the HFACF to 1 gives a more accurate comparison of the total decay rates (lifetimes) with all of the MD predictions being almost identical. This confirms that overall the results from the fitting algorithm was reliable. The discrepancies (mainly at 300K) between MD and perturbation are most likely due to sampling issues that could be resolved with a longer simulation or 4^{th} order anharmonicity.

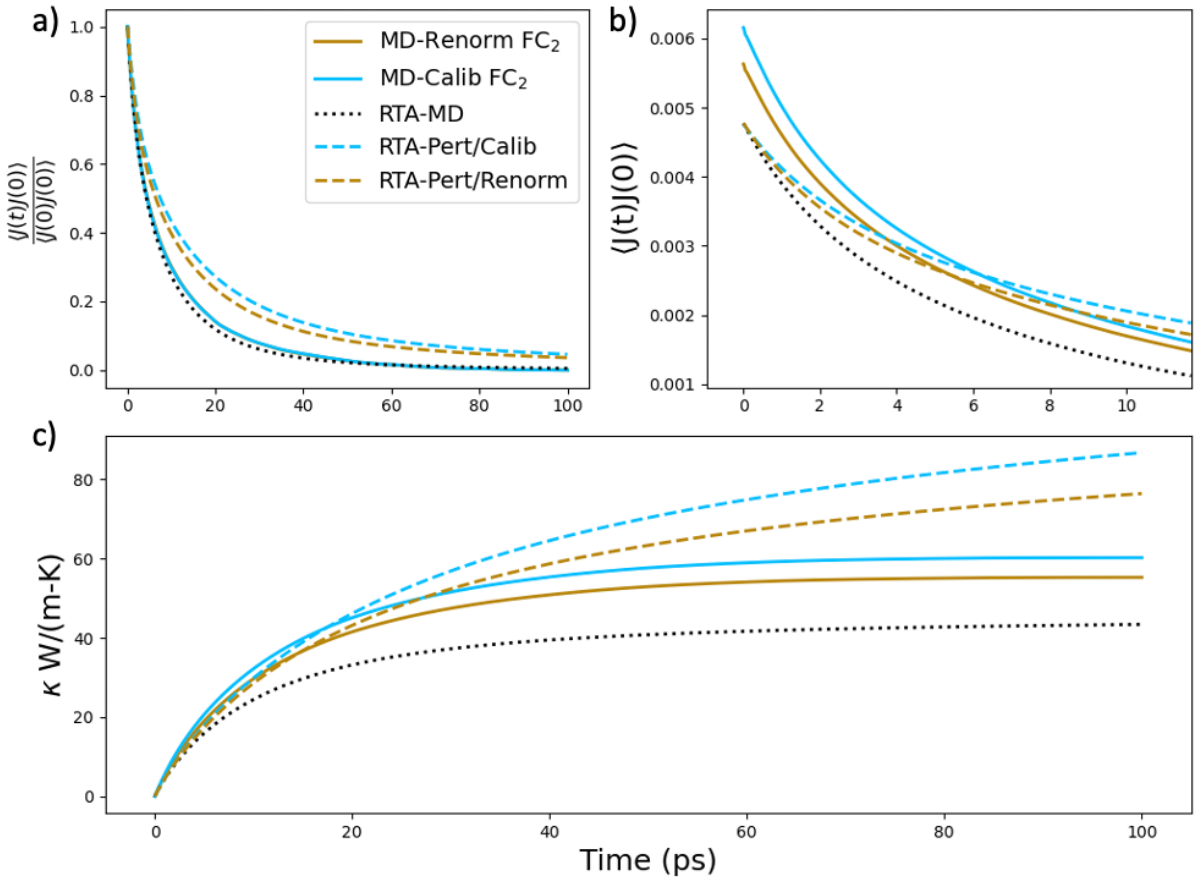

Figure 5.3: b) HFACF with the Peierls heat flux and Hardy, a) normalized heat flux, and c) resultant thermal conductivity from each HFACF at 300K

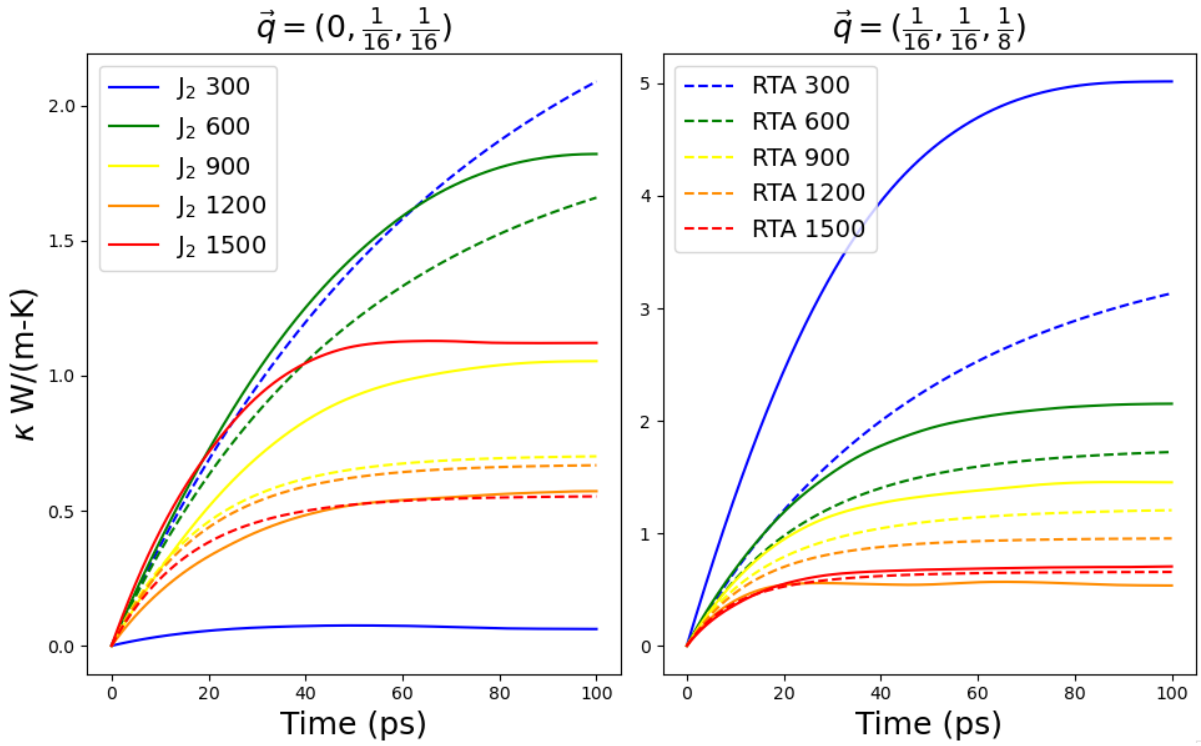

Figure 5.4: Total mode contribution to κ at q-points, (left) $\vec{q} = (0, \frac{1}{16}, \frac{1}{16})$ and (right) $\vec{q} = (\frac{1}{16}, \frac{1}{16}, \frac{1}{8})$, where perturbation predicted the highest κ values.

Although $\vec{J}_{2,diagonal}$ correlation has a higher initial position, the slower decay (long lifetime) prediction of the perturbation theory causes the drastically higher thermal conductivity predictions $\kappa_{pert,calib}$ and $\kappa_{pert,renorm}$. This prevents these HFACF integrations with perturbation theory from converging to the limit of 125 W/(m-K) and 105 W/(m-K), respectively at 50 ps correlation time (or even 100 ps zero-padded correlation time). For efficiency of resources (and possible sampling), an ideal simulation time per temperature can be calculated based on the percent convergence of the highest phonon lifetime. With the exponential integration in Eq 5.13, the κ_{rta} will reach 90% of the true integration value at some time $t_{90\%}$ by evaluating the integral:

$$\int_0^{t_{90\%}} e^{-t/\tau_\lambda} dt = .9\tau_\lambda \tag{5.15}$$

To capture 90% of the thermal conductivity of a phonon mode λ by integration, the integration time must be $2.3\times\tau_\lambda$, which corresponds to a $4.6\times\tau_\lambda$ simulation time without zero-padding. The longest perturbation lifetime of 543 ps would need a simulation time of 2,500 ps (or 2.5 ns) to accurately predict the total κ contribution. With this being the upper limit, an integration

Thermal Conductivity (κ) W/(m-K)			
Temp	$\kappa = \frac{1}{VT^2}\int_0^{100ps}\langle J_{2,diagonal}J_{2,diagonal}\rangle dt$		$\kappa = c_v\vec{v_g}^2\tau$
300K	55.29 (renormalized)	60.27 (calibrated)	44.90
600K	30.14	32.95	26.11
900K	18.09	19.70	15.83
1200K	11.38	12.62	10.99
1500K	8.69	9.63	7.59

Table 5.1: κ with $J_{2,diagoanl}$ HFACF and smRTA based on the 1-phonon spectra using MD

time of 100 ps, 500 ps, and 1,000 ps gives 69.1%, 91.7%, and 97.2% of the total predicted κ with the calibrated perturbation lifetimes. Reliable G-K calculations have been performed at much shorter simulation times than the estimated upper limit for Silicon [18, 7].

Assuming the heat flux as a zero-mean stochastic quantity, the HFACF at $t = 0$ (maximum value) equates to the variance of the heat flux. The success of the G-K approach relies on having a realistic measurement of the magnitude heat flux [4, 13], which alters variance of the HFACF. Currently, the calibrated heat flux $J_2^{calib}$is defined by substituting the dynamical matrix in Eq 5.9 with a dynamical matrix with experimentally calibrated frequencies at 300K and MD frequency downshifts at higher temperatures. Based on the differences of the calibrated and renormalized FC_2 results with G-K, it can be reasoned that the displacement and velocity must also be calibrated to have a true predictor of the thermal conductivity with G-K (after accounting for sampling issues).

The calibration method took as inputs scale factors that matched the fitted MD mode frequencies to the frequencies presented by Dolling [12] at 300K and output scale factors a_λ at all phonon modes λ. The new calibrated FC_2 would have scaled eigenvalues of $m\omega_{calib}^2 = m(a_\lambda\omega_{renorm})^2$ compared to the renormalized FC_2. The q-projected displacement x_q and velocity v_q are assumed to be a summation of orthogonal coordinate modes and conjugate momentum modes, respectively. It can be reasoned, with harmonic representation of the coordinate mode and conjugate momentum, that if the displacement follows a sinusoidal function with amplitude $A(\omega_{renorm})$ and the velocity is proportional to the derivative, then the displacement would scale based on $A(a_\lambda\omega_{renorm})$ while the velocity would scale by $a_\lambda A(a_\lambda\omega_{renorm})$. If the amplitude is independent of the frequency, then total calibrated heat flux would scale by an additional scale factor including that from the calibrated FC_2. Applying a scale factor, based on fraction

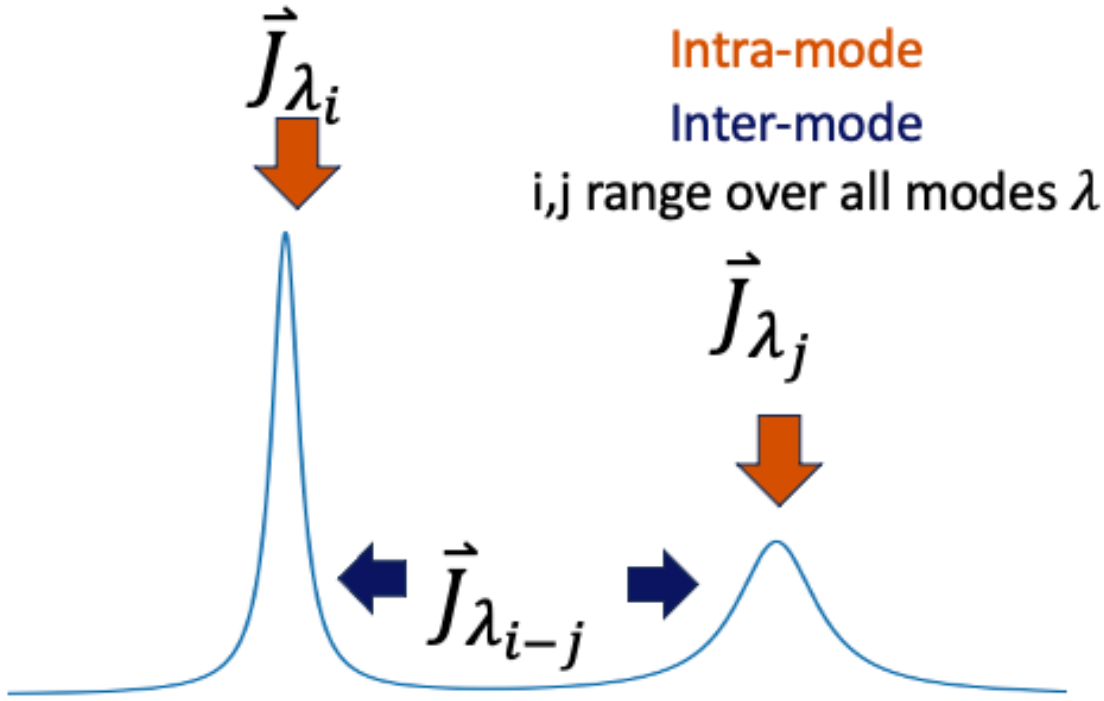

Figure 5.5: Intra-mode and inter-mode heat flux within the second-order Hardy heat flux

between 1500K κ from $\vec{J}_2$ HFACF and the extrapolated $\kappa_{lattice}$ line of Glassbrenner & Slack [17], of 1.96 to all the temperature results gives a 107.59, 57.60, 34.11, 21.21, 15.82 W/(m-K) prediction at 300K, 600K, 900K, 1200K, and 1500K, respectively, thus, demonstrating the an impact of a calibrated scale factor for the heat flux.

5.3 Inter-mode Heat Flux

By definition, the Peierls heat flux is an intra-mode heat flux ($\vec{J}_{\lambda\lambda'} = 0$ when $\lambda \neq \lambda'$) while the Hardy $\vec{J}_{2,lattice}$ (shorted to $\vec{J}_2$ for the remainder of the chapter) includes both intra-mode and inter-mode components at a particular q-point shown in Fig 5.5. As such, each heat flux does not consider any cross q-point terms. Separating $\vec{J}_2$ as

$$\vec{J}_2 = \vec{J}_{2,diagonal} + \vec{J}_{2,off-diagonal} \equiv \vec{J}_{inter-mode} + \vec{J}_{intra-mode} \tag{5.16}$$

allows the $\vec{J}_2$ HFACF to quantify the contribution of both the inter- and intra-mode heat flux to the total thermal conductivity.

As seen by the agreement between smRTA approximation and experimental conductivity measurements, the intra-mode heat flux is the dominant term for a low defect ordered material like diamond Silicon at ambient temperatures. For a disordered system like amorphous Silicon, there is no q-point projection due to the lack of translational symmetry. Phillips (1972) proposed that the heat transfer in amorphous solids comes from the tunneling between phonon states with thermal conductivity increasing then saturating at high temperatures[39]. By combining the heat flux operator $\vec{S}_{\lambda\lambda'}$ by Hardy[21] and G-K formalism, Allen-Feldman (1993) derives the thermal conductivity for disordered harmonic solids as [1]:

$$\begin{aligned} \kappa_{disordered} &= \frac{1}{V}\sum_{\lambda} C_\lambda(T) D_\lambda \\ D_\lambda &= \frac{\pi V^2}{3\hbar^2\omega_\lambda^2}\sum_{\lambda\neq\lambda'} |S_{\lambda\lambda'}|^2 \delta(\omega_\lambda - \omega_{\lambda'}) \end{aligned} \tag{5.17}$$

where $C_\lambda(T)$ is the heat capacity of the λ-th mode at some temperature T, and D is a diffusivity term defined by the heat flux operator. The 1^{st} order approximation of the $\vec{S}_{\lambda\lambda'}$ becomes [8]:

$$S^\alpha_{\lambda\lambda'} = \frac{\omega_\lambda + \omega_{\lambda'}}{2}\hat{V}^\alpha_{\lambda\lambda'} \tag{5.18}$$

where $\hat{V}^\alpha_{\lambda\lambda'}$ is a velocity operator. The Wigner transport equation in the single mode approximation (SMA) [44]:

$$\begin{gathered} \kappa^{\alpha\beta}_{SMA} = \frac{\hbar^2}{k_B T^2}\frac{1}{VN_a}\sum_{\vec{q}}\sum_{\lambda\lambda'} \frac{\omega_\lambda + \omega_{\lambda'}}{2} V^\alpha_{\lambda\lambda'} V^\beta_{\lambda\lambda'} \times \frac{\omega_\lambda f_\lambda(f_\lambda+1) + \omega_{\lambda'} f_{\lambda'}(f_{\lambda'}+1)}{4(\omega_{\lambda'}-\omega_\lambda)^2 + (\Gamma_\lambda + \Gamma_{\lambda'})^2}(\Gamma_\lambda + \Gamma_{\lambda'}) \\ \text{where } V^\alpha_{\lambda\lambda'} = \frac{2\sqrt{\omega_\lambda\omega_{\lambda'}}}{\omega_\lambda + \omega_{\lambda'}}\hat{V}^\alpha_{\lambda\lambda'} \end{gathered} \tag{5.19}$$

is a unified theory for the transport equation that reduces to the Peierls equation when $\lambda = \lambda'$ and Eq 5.17 with the 1^{st} order heat flux operator when $\lambda \neq \lambda'$. The Wigner transport equation models the inter-mode thermal conductivity as a function of a linear combination of mode frequencies ω_λ and $\omega_{\lambda'}$, which will be useful in understanding the $\vec{J}_{off-diagonal}$ HFACF.

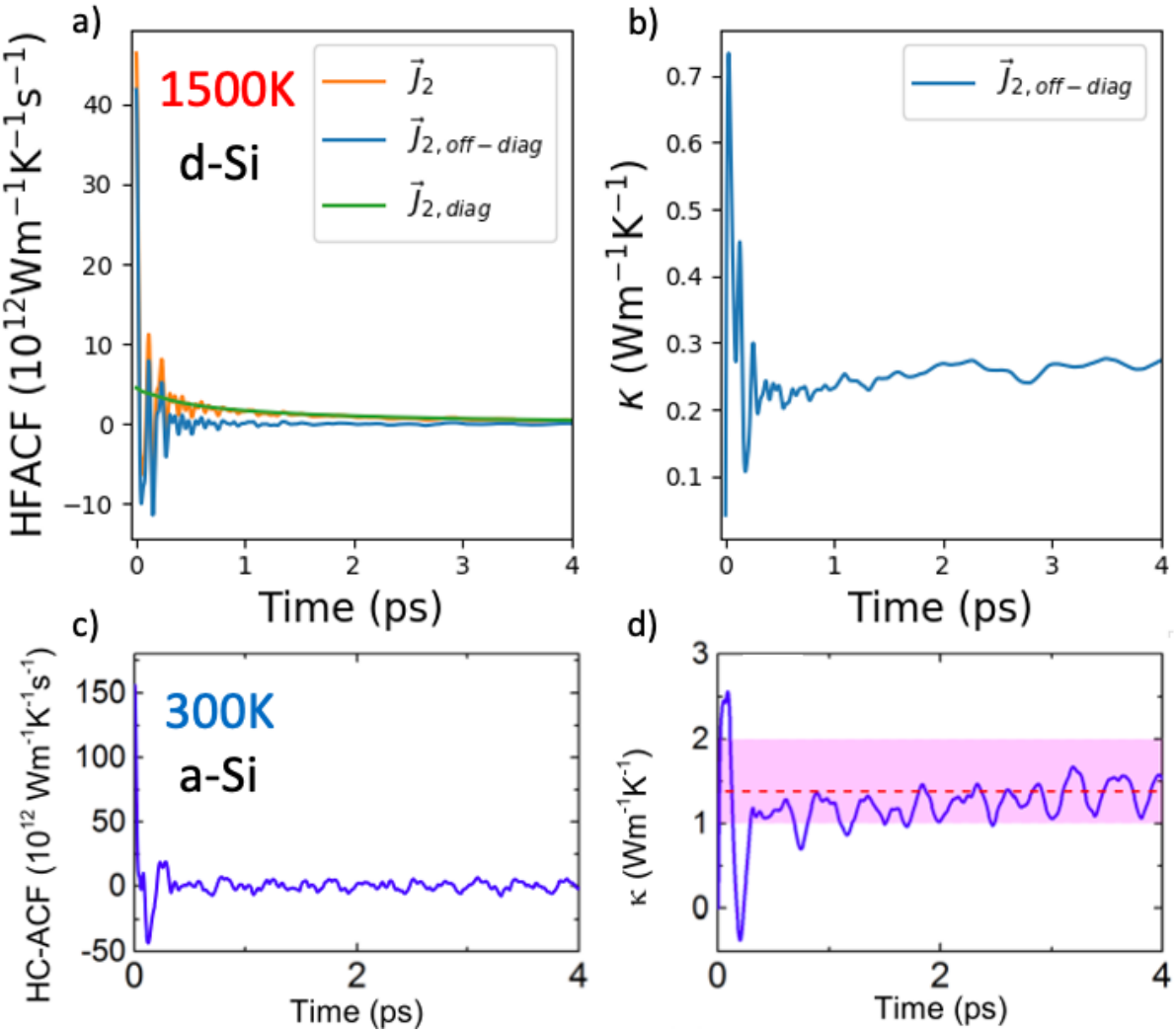

Figure 5.6: a) HFACF from the components of $\vec{J}_2$ and b) resulting κ from the $\vec{J}_{2,off-diagonal}$ HFACF at 1500K. c) Kang et. al. (2017) results [25] of amorphous HFACF and b) resultant κ by integration at 300K

Thermal Conductivity (κ) W/(m-K)				
Temp	$\kappa_{\vec{J}_2}$	$\kappa_{diagonal}$	$\kappa_{off-diagonal}$	κ_{cross}
300K	54.88	55.29	0.66	-1.07
600K	29.38	30.14	0.42	-1.18
900K	17.40	18.09	0.36	-1.06
1200K	10.82	11.38	0.34	-0.90
1500K	8.07	8.69	0.32	-0.94

Table 5.2: κ from all the HFACF components of $\vec{J}_2$

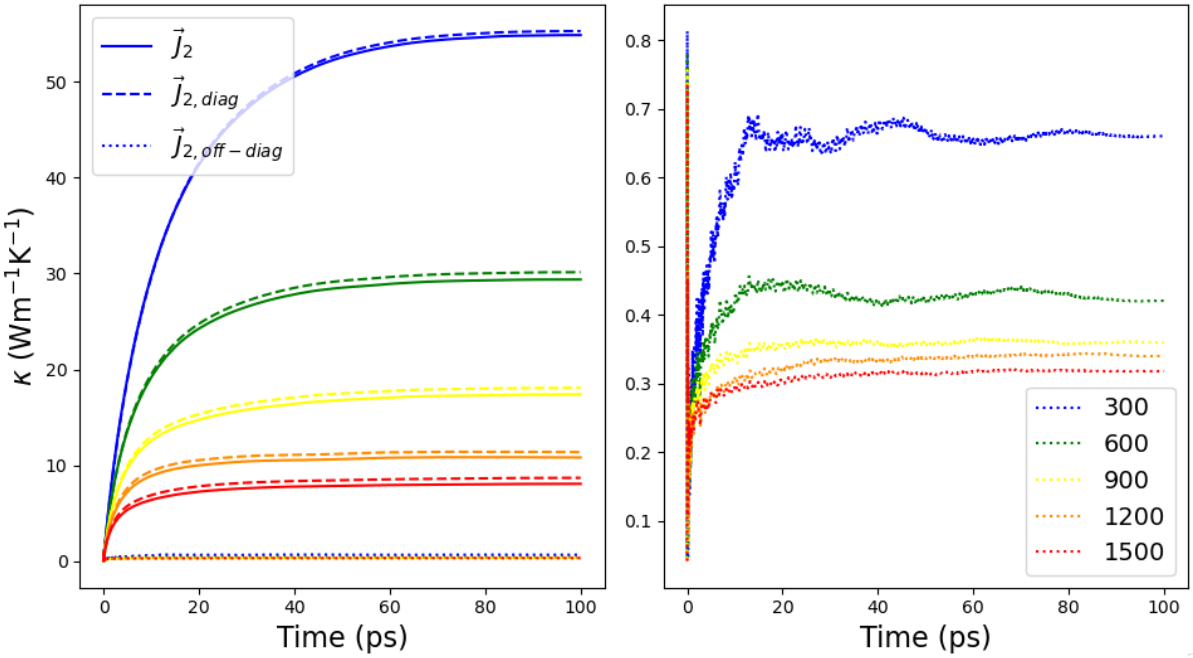

Figure 5.7: κ from (left) the HFACF components of $\vec{J}_2$ (excluding the cross terms) with (right) a zoomed axes for the smaller $\vec{J}_{off-diagonal}$ HFACF integration values

The $\vec{J}_{2,off-diagonal}$ HFACF at 1500K resembles that of the amorphous HFACF at 300K [25] with a quicker decay than the $\vec{J}_{2,diagonal}$ HFACF and causes most the oscillations of the $\vec{J}_2$ HFACF. At 1500K, $\kappa_{off-diagonal}$, the thermal conductivity from the $\vec{J}_{2,off-diagonal}$ HFACF, takes $\sim$15 ps to converge to .32 W/(m-K) while amorphous G-K calculations reached convergence of 1.5 W/(m-K) at $\sim$4 ps [25]. $\kappa_{off-diagonal}$ decreases with temperature (from 0.66 W/(m-K) at 300K to 0.32 W/(m-K) at 1500K shown in Table 5.2), which is contrary to amorphous thermal conductivity increasing to a value between 1-2 W/(m-K) at temperatures up to 750K. [6, 56] Comparatively, the Wigner transport equation predicts a total inter-mode $\kappa_{\lambda\neq\lambda'}$ of 0.23 W/(m-K) at 300K. Although the meaning of $\kappa_{off-diagonal}$ comes from a cross-mode heat flux similar to the amorphous theory, $\kappa_{off-diagonal}$ behaves differently than the amorphous thermal conductivity given the limited high temperature data for amorphous.

5.4 Intra/Inter-mode Cross Correlation κ_{cross}

Although $\kappa_{diagonal}$ and $\kappa_{off-diagonal}$ are positively defined, the thermal conductivity from the $\vec{J}_2$ HFACF, $\kappa_{\vec{J}_2}$, is slightly lower than $\kappa_{diagonal}$ for all temperatures. This is explained by separating

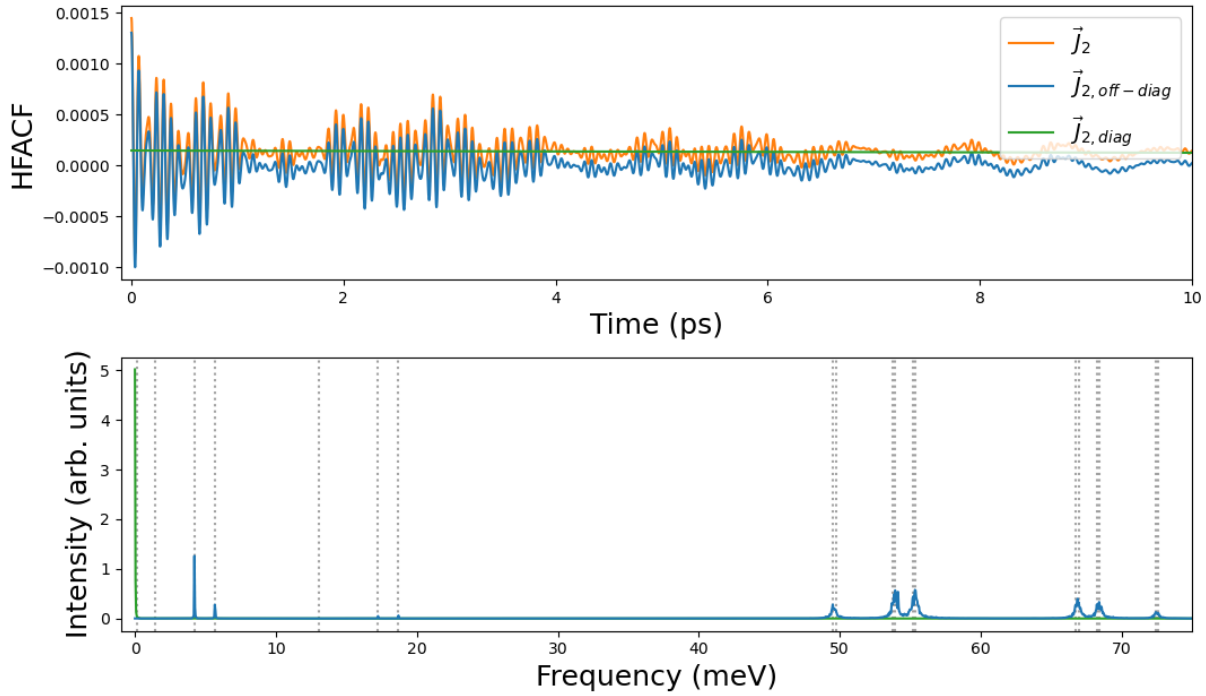

Figure 5.8: (top) HFACF from $\vec{J}_2$ (and its components) and (bottom) Fourier transformation at $\vec{q} = (\frac{1}{16}, \frac{1}{16}, \frac{1}{8})$ and 300K. (dotted lines) All combinations of $\omega_\lambda - \omega_{\lambda'}$ and $\omega_\lambda + \omega_{\lambda'}$

the components of $\kappa_{\vec{J}_2}$ as:

$$\begin{aligned}\kappa_{\vec{J}_2} &= \frac{1}{VT^2}\int_0^\infty \langle \vec{J}_2 \vec{J}_2 \rangle = \frac{1}{VT^2}\int_0^\infty \langle \vec{J}_{diagonal} + \vec{J}_{off-diagonal} | \vec{J}_{diagonal} + \vec{J}_{off-diagonal} \rangle dt \\ &= \frac{1}{VT^2}\int_0^\infty \langle \vec{J}_{diagonal}\vec{J}_{diagonal} \rangle + \langle \vec{J}_{off-diagonal}\vec{J}_{off-diagonal} \rangle + 2\langle \vec{J}_{diagonal}\vec{J}_{off-diagonal} \rangle dt \\ &= \kappa_{diagonal} + \kappa_{off-diagonal} + \kappa_{cross}\end{aligned} \tag{5.20}$$

With no additional restrictions, there is no guarantee that the cross term, $2\langle \vec{J}_{diagonal}\vec{J}_{off-diagonal} \rangle$, is always positive or should be assumed zero. Even with $\kappa_{off-diagonal} \ll \kappa_{diagonal}$, the combination $\kappa_{off-diagonal} + \kappa_{cross}$ causes an overall reduction in the predicted thermal conductivity with κ_{cross} accounting for $\sim$1 W/(m-K). Thus, considering cross-mode heat flux contributions lowered the total predicted thermal conductivity, which is contrary to the Wigner transport equation.

Due to the importance of the κ_{cross}, a unified theory should reduce to a combination of an inter-mode and intra-mode heat flux. A foundation for this proposed theory relies on an

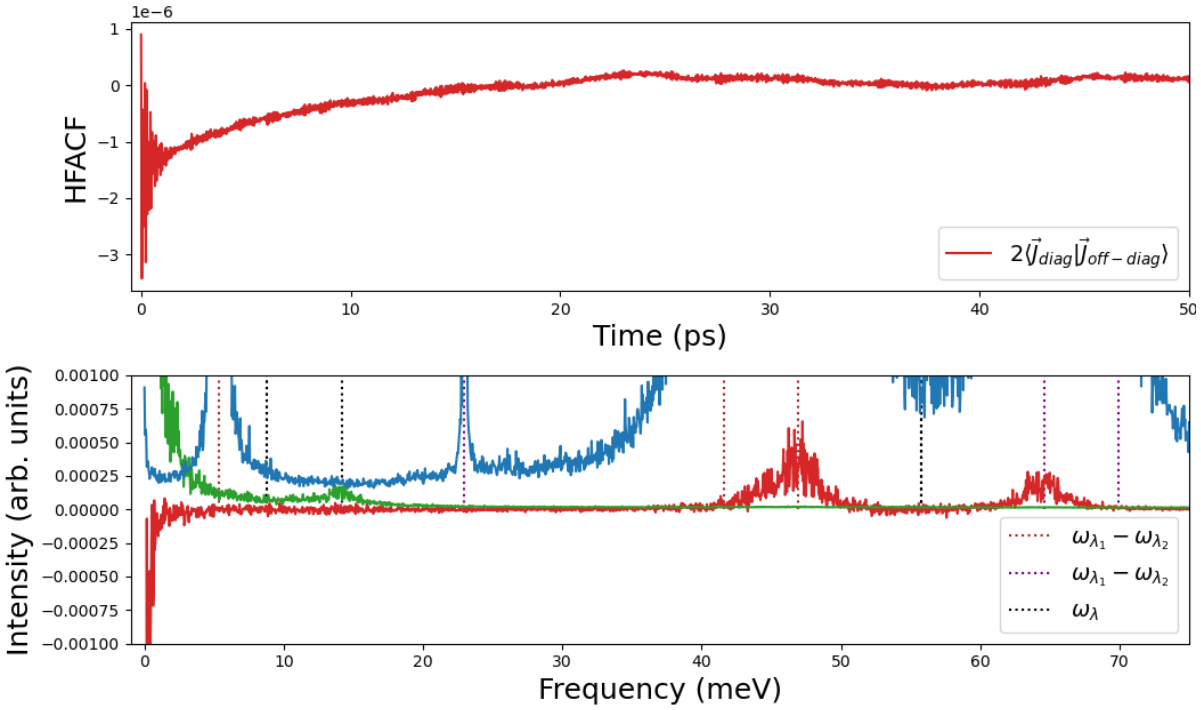

Figure 5.9: (top) Cross term $2\langle\vec{J}_{diagonal}\vec{J}_{off-diagonal}\rangle$ HFACF and (bottom) Fourier transformation of cross term, $\vec{J}_{diagonal}$ and $\vec{J}_{off-diagonal}$ HFACF at $(0, \frac{1}{8}, \frac{1}{8})$ and 1500K

analytical analysis of the $\vec{J}_2$ HFACF to decouple the $\vec{J}_{diagonal}$ and $\vec{J}_{off-diagonal}$ HFACF. The current implementation of this work calculates $\vec{J}_{diagonal}$ with the renormalized eigenvectors and $\vec{J}_{off-diagonal} = \vec{J}_2 - \vec{J}_{diagonal}$. $\vec{J}_{diagaonal}$ HFACF has the shape $\sum_\lambda e^{-\frac{t}{\tau_\lambda}}$ which Fourier transformations are Lorentzians centered at $\omega = 0$ while $\vec{J}_{off-diagonal}$ resembles a series of under-damped harmonic oscillators. The frequency of the oscillators (location of peaks in the FFT Fig 5.8) sample all the $\omega_\lambda - \omega_{\lambda'}$ and $\omega_\lambda + \omega_{\lambda'}$ pairs with the renormalized frequencies ω of modes λ. At 1500K, the q-point $(0, \frac{1}{8}, \frac{1}{8})$ exhibits only 3 unique frequency modes: 8.82, 14.14, and 55.74 meV. A closer look at the Fourier transformation of the $\vec{J}_{diagonal}$ HFACF at this q-point (Fig 5.9) shows an excitation at ω =14.14 meV, which is unexpected by the Peierls HFACF. Other q-points shows the same excitation mainly at acoustic renormalized frequency locations. The Fourier transformation of the cross term $2\langle\vec{J}_{diagonal}\vec{J}_{off-diagonal}\rangle$ has noticeable peaks at locations 55.74 $\pm$ 8.82 meV. This leads to a reasoning that $\vec{J}_{diagonal}$ may include all excitaion at the renormalized frequency locations with the acoustic frequencies being the strongest. With the inclusion of the negative Lorentzian, $2\langle\vec{J}_{diagonal}\vec{J}_{off-diagonal}\rangle$ could be

modeled as a under-damped harmonic oscillator and a negative exponential decay such that:

$$2\langle \vec{J}_{diagonal}\vec{J}_{off-diagonal}\rangle = \sum_{\lambda} Ae^{-\frac{t}{\tau_\lambda}} + \sum_{\lambda\neq\lambda'} e^{-\frac{t}{\tau_{\lambda\lambda'}}}(Bcos((\omega_\lambda-\omega_{\lambda'})t) + Ccos((\omega_\lambda+\omega_{\lambda'})t)) \tag{5.21}$$

where $\tau_{\lambda\lambda'}$ is a lifetime matrix between different modes λ and $A/B/C$ are constants. To combine the lifetime matrix, a possible reduction to Eq 5.22 is:

$$2\langle \vec{J}_{diagonal}\vec{J}_{off-diagonal}\rangle = \sum_{\lambda\lambda'} Ae^{-\frac{t}{\tau_{\lambda\lambda'}}}(cos((\omega_\lambda-\omega_{\lambda'})t) + \frac{\omega_\lambda-\omega_{\lambda'}}{\omega_\lambda+\omega_{\lambda'}}cos((\omega_\lambda-\omega_{\lambda'})t)) \tag{5.22}$$

such that:

$$\lim_{\omega_{\lambda'}\to\omega_\lambda} 2\langle \vec{J}_{diagonal}\vec{J}_{off-diagonal}\rangle = \sum_{\lambda} Ae^{-\frac{t}{\tau_\lambda}} \tag{5.23}$$

reduces to the Peierls HFACF for degenerate states.

5.5 Conclusions

In summary, we show that the integral convergence issues of the Green-Kubo formalism can be mitigated by enforcing $\delta(|\vec{q}_1-\vec{q}_2|)$ since $\vec{J}_{2,lattice}$ has no imaginary component with a summation over q-space. We separated $\vec{J}_{2,lattice}$ into an intra-mode and inter-mode component. The intra-mode self-correlation confirmed the lifetime predictions of Chapter 4 while the inter-mode demonstrated how near-melting point diamond Silicon resembles room temperature amorphous Silicon. Previous unified transport theories like Wigner transport equation predicts κ_L as a summation of positively-defined intra-mode and inter-mode terms but we proved that adding an inter-mode contribution also creates an inter-/intra-mode cross correlation term. This term, neglected by previous theories, is: 1) larger in magnitude than the inter-mode term and 2) negative at all simulated temperatures of this work. A unified transport theory should instead define a unified definition of the heat flux (with intra- and inter-mode terms) to insert into the Green-Kubo formalism to account for cross-term interactions.

Chapter 6

Higher Order Heat Flux $\vec{J}_{2,displacement}$,$\vec{J}_{3,lattice}$, and $\vec{J}_{4,lattice}$

As our primary research focus centers on simulating the heat transport properties of crystals at elevated temperatures extending up to their melting points, we broaden our investigation to encompass higher-order heat flux terms within the comprehensive framework of the general Hardy heat flux. This expansion aims to discern whether anharmonicity significantly amplifies these terms, consequently influencing the predicted thermal conductivity. Notably, conventional kinetic phonon transport theory systematically overlooks the contribution of these higher-order terms, addressing them only indirectly through discussions of phonon frequency renormalization at elevated temperatures. Previous simulation studies on these higher terms are sparse, often constrained by oversimplified material systems, such as hypothetical two-dimensional Argon lattices. To the best of our knowledge, no direct reports exist on MD simulations of these higher-order heat flux terms for realistic materials like Silicon crystals, utilizing accurate interatomic potentials (IAP) of the caliber of DFT-IAPs or ML-IAPs. This chapter not only introduces a technique for renormalizing the FC3/FC4 but also incorporates q-space orthogonality enforcement for higher-order Heat Flux Auto-Correlation Functions (HFACF). The significance of the third-order heat flux, $\vec{J}_{3,lattice}$, and its cross correlations will be emphasized, shedding light on the need for further exploration to effectively handle the fourth-order heat flux, $\vec{J}_{4,lattice}$

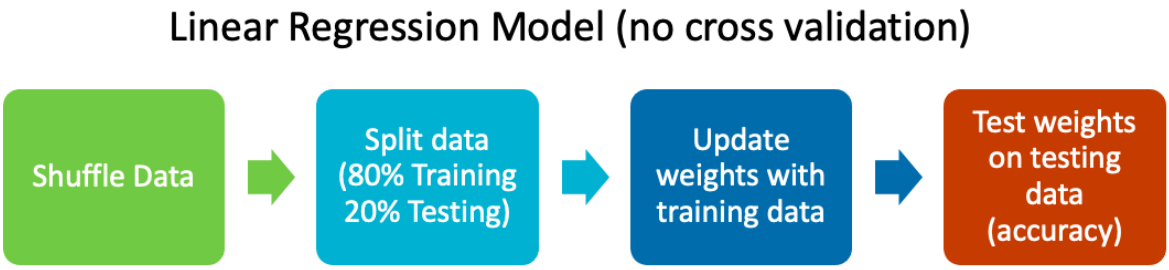

Figure 6.1: Workflow for a linear regression model without cross validation

6.1 Renormalized FC_2 and FC_4

Temperature dependent FC_3 have been computed by fitting MD forces with a Taylor series expansion of the force in real space. [23]. Two real space fittings:

$$\begin{aligned}\vec{f}^{I} &\approx -\sum_{j\beta} A^{renorm}_{i\alpha j\beta} u_{j\beta} - W^{1}_{34} \sum_{j\beta}\sum_{k\gamma} B_{i\alpha j\beta k\gamma} u_{j\beta} u_{k\gamma} - W^{2}_{34} \sum_{j\beta}\sum_{k\gamma}\sum_{l\rho} C_{i\alpha j\beta k\gamma, l\rho} u_{j\beta} u_{k\gamma} u_{l\rho} \\ &\approx \vec{f}_2^{renorm} + W^{1}_{34}\vec{f}_3 + W^{2}_{34}\vec{f}_4\end{aligned} \tag{6.1}$$

and

$$\begin{aligned}\vec{f}^{II} &\approx -\sum_{j\beta} A^{renorm}_{i\alpha j\beta} u_{j\beta} - W^{1}_{34} \sum_{j\beta}\sum_{k\gamma} B_{i\alpha j\beta k\gamma} u_{j\beta} u_{k\gamma} \\ &\approx \vec{f}_2^{renorm} + W^{1}_{3}\vec{f}_3\end{aligned} \tag{6.2}$$

were performed by finding the weights W on a single i^{th}-atom with force $\vec{f}$ as a function of displacement $\vec{u}$ using a linear regression model. In real space, each weight W is only a function of temperature. The renormalized second order force $\vec{f}_2^{renorm}$ remained constant since it was built from the 1-phonon spectra fitting. Eq 6.2 is used to adjusted the bare FC_3 for perturbation calculations while Eq 6.1 is a basis to compare to the q-projected force fitting.

W_3^1 Linear Regression Values		
Temp (K)	Mean	Std
300	0.956	0.00194
600	0.909	0.00430
900	0.853	0.00770
1200	0.797	0.00371
1500	0.740	0.00409

Table 6.1: Weights for the linear regression model by fitting the forces of a single atom in real space

A linear regression model solves for a linear combinations of weights W to predict some value Y from data X with i features with the equation:

$$Y = W^0 + \sum_i W^i X_i \tag{6.3}$$

The constant W^0 is $\vec{f}_2^{renorm}$ and the features are the 3^{rd} order forces (and 4^{th} order forces depending on the equation). The steps to determine the weights are shown in Fig 6.1. To prevent over-fitting and improve the generality of the model, a validation sets is usually used. Validation sets are training/testing sets created by further splitting the training data in N total validation sets. These sets are used to swap around the data used for training with both accounts for possible outliers and prevents over-fitting to a specific trained data set. Since over-fitting and accuracy of this model is not a priority for this work, no validation sets are used and an ensemble average is taken over all the models. For the real space model with only the $\vec{f}_3$ feature, the model returned W_3^1 values listed in Table 6.1 and W_{34}^1 were 0.018 greater than W_3^1 at both 300K and 1500K.

This work determined another set of weights by fitting the q-projected force:

$$\vec{f}(\vec{q}) = \frac{1}{\sqrt{N}} \sum_{\vec{l}_i} \vec{f}(l) e^{-i\vec{q}\cdot(\vec{l}_i + \vec{r}_i)} \tag{6.4}$$

at each q-point such that:

$$\begin{aligned}\vec{f}(\vec{q}) &\approx \sum_{j\beta} A_{i\alpha j\beta}(\vec{q}) u_{j\beta}(\vec{q}) + \frac{W^1_{34}(\vec{q})}{2!} \sum_{j\beta}\sum_{k\gamma}\sum_{\vec{q}_2,\vec{q}_3} B_{i\alpha j\beta k\gamma}(-\vec{q},\vec{q}_2,\vec{q}_3) u_{j\beta}(\vec{q}_2) u_{k\gamma}(\vec{q}_3) \Delta(-\vec{q}+\vec{q}_2+\vec{q}_2) \\ &\quad + W^2_{34}(\vec{q}) \sum_{j\beta} A^{eff}_{i\alpha j\beta}(\vec{q}) u_{j\beta}(\vec{q}) \\ &\approx \vec{f}_2^{renorm}(\vec{q}) + W^1_{34}(\vec{q}) \vec{f}_3(\vec{q}) + W^2_{34}(\vec{q}) \vec{f}_4^{eff}(\vec{q})\end{aligned} \tag{6.5}$$

with A^{eff} being a reduction of FC_4 by Eq 2.91. In q-space, each weight $W(\vec{q})$ is a function of both temperature and q-point. The q-projected forces are a complex number, which is not supported by the scikit-learn package. The data points were split into a real component and imaginary component. These components are fitted equally, thus, doubling the total training data. Without a mode projection, two features are used per q-point for the 3^{rd} and 4^{th} order anharmonicity for a total of (2048×2) total weights. No additional work was done to reduce the total weights to the irreducible set of q-points. Although anharmonicity is mode dependent at each q-point based on the smRTA analysis, two features per q-point provides flexibility to capture the q-point anharmonicity as compared to the real space fitting. Two alternative equations was tested to check for possible double counting of anharmonicity: 1) allowing $\vec{f}_2^{renorm}$ to be an adjustable parameter, and 2) changing $\vec{f}_2^{renorm}$ to an adjustable $\vec{f}_2^{bare}$. There was no major differences between any of the methods. This confirms that the renormalized FC_2 resembles a scaled bare FC_2 since the renormalized FC_2 is built with the bare eigenvectors as a basis.

6.2 Consequences of Selection Rule

As a means to reduce the computational cost of the q-projected FC_4, an approximate FC_2, A^{eff}, was used by integrating over the FC_4 twice in real space. One consequence of this folding reduces the selection rule from $\Delta(-\vec{q}+\vec{q}_2+\vec{q}_3+\vec{q}_4)$ to $\Delta(-\vec{q}+\vec{q}_2)$ or $\vec{q}=\vec{q}_2$ for the q-projected 4^{th} order force $\vec{f}_4(\vec{q})$ calculations. As a result, there is no noticeable change in the q-space fitting at both 300K and 1500K as compared the changes seen in the real space fitting shown in Fig 6.2. While the Γ-point forces give the best comparison to the real space since the

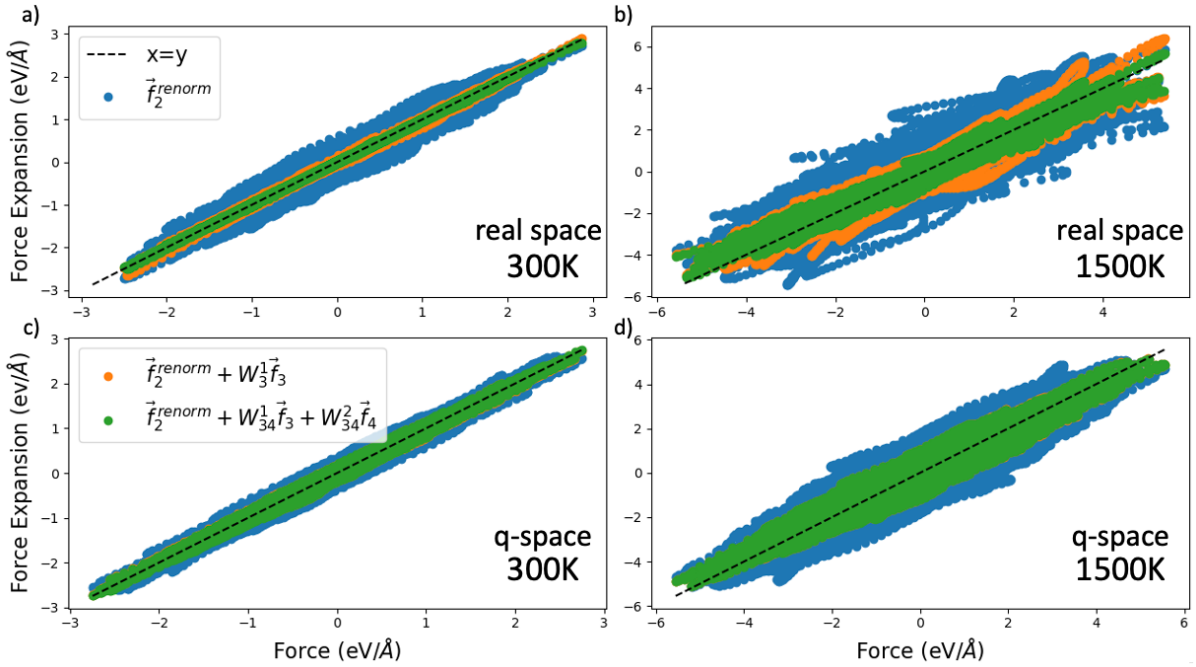

Figure 6.2: Linear Regression Model fitting of a) real space forces of the first atom at 300K b) and 1500K. Linear Regression Model fitting of q-space forces at the zone center $\Gamma-$point at c) 300K and d) 1500K. The force has no imaginary component at the Γ-point

imaginary component is zero, this low impact A^{eff} was present in all of the first 10 q-points of the commensurate grid that were tested. Two of these points,$\vec{q} = (0, \frac{1}{16}, \frac{1}{16})$ and $\vec{q} = (\frac{1}{16}, \frac{1}{16}, \frac{1}{8})$, were expected to have a higher 4^{th} order anharmonicity based on the lifetime analysis. The A^{eff} matrix does not fully capture the 4^{th} order anharmonicity and the information lost is a direct result of the reduced selection rule. Thus, anharmonicity (in q-space) is linked to the selection rule and folding a FC_4 into an approximate FC_2 provides no added benefit alongside a renormalized FC_2. An alternative reduction method for the FC_4 could be attempted with the q-projected forces with a selection rule changed from $\Delta(-\vec{q}+\vec{q}_2+\vec{q}_3+\vec{q}_4)$ to $\Delta(-\vec{q}+\vec{q}-\vec{q}_3+\vec{q}_3)$. While this would increase the computational cost close to the 3^{rd} order calculations and should provide more information than the previous A^{eff}, it would exclude any U-process-like ($\vec{G} \neq 0$) selections. While U-process scattering at high temperatures have been found negligible at high temperatures for κ calculations[33], more work could be done to study the importance of U-process-like selection rule in the q-projected forces or correlation with U-process scattering in κ calculations.

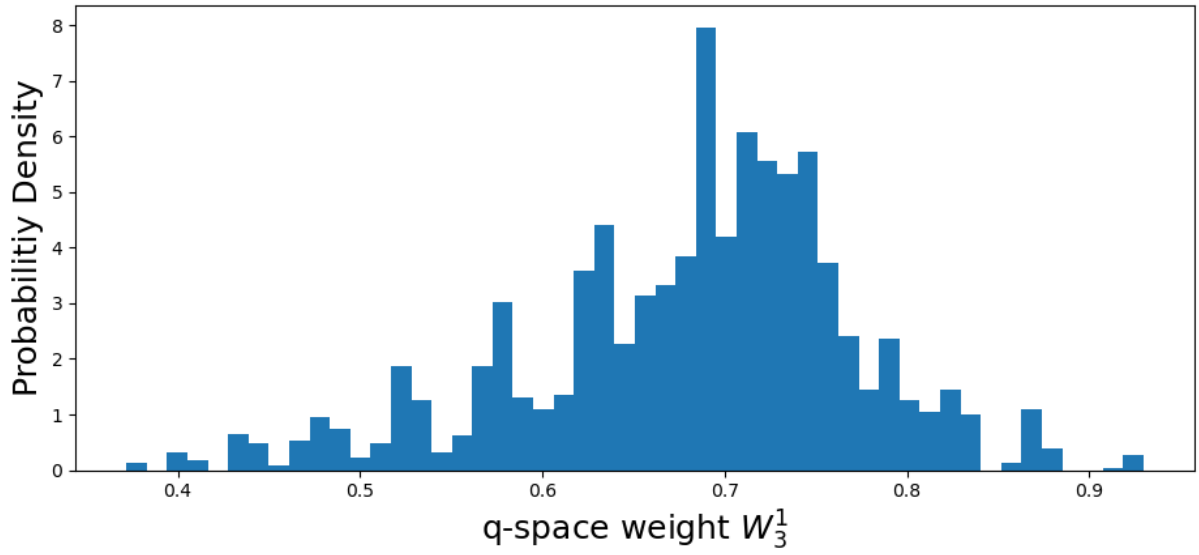

Figure 6.3: Probability distribution of $W_3^1(\vec{q})$ in q-space at 300K

With only $\vec{f}_3(\vec{q})$ being the important feature during the fitting process, the q-space model became:

$$\vec{f}(\vec{q}) \approx \vec{f}_2^{renorm}(\vec{q}) + W_3^1(\vec{q})\vec{f}_3(\vec{q}) \tag{6.6}$$

with one feature, $W_3^1(\vec{q})$, per q-point per temperature. While W_3^1 in real space was 0.956 at 300K, the q-space equivalent had a distribution shown in Fig 6.3. $W_3^1(\vec{q})$ values over 0.9 at 300K included the Γ-point and other high lifetime q-points. Lower values have smaller deviations from $\vec{f}_2^{renorm}$ with a q-point near the average value ($W_3^1 = 0.682$) shown in Fig 6.4. $W_3^1(\vec{q})$ attempts to fit the $\vec{f}_3$ based on all higher anharmonicity and lower values do not necessarily correlate to lower 3^{rd} order anharmonicity. An improved methodology to account for the 4^{th} order forces would clarify whether all anharmonicity is small at the q-point or just the 3^{rd} order. The q-space $W_3^1(\vec{q})$ is assumed to be the scale factor for the renormalized q-projected FC_3 per temperature such that the bare phonon FC_3, $B(\vec{q}_1, \vec{q}_2, \vec{q}_3)$, is replace with $W_3^1(\vec{q}_1)B(\vec{q}_1, \vec{q}_2, \vec{q}_3)$ in Eq 2.88 at q-point $\vec{q}_1$. This FC_3 is used for the subsequent $\vec{J}_3$ calculations while $\vec{J}_4$ is neglected since it is derived from A^{eff}.

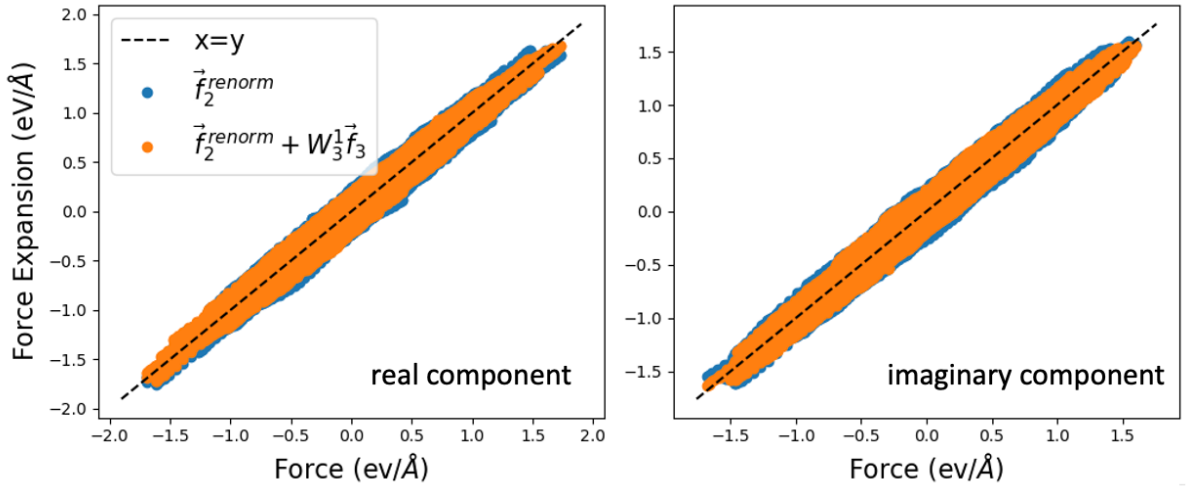

Figure 6.4: Linear Regression Model force fitting at $\vec{q} = (0, \frac{5}{16}, \frac{5}{16})$ and 300K with a W_3^1 value of 0.709

6.3 Orthogonality Enforcement of Higher Order HFACF

Cross q-point orthogonality was enforced in both the $\vec{J}_{2,dis}$ and $\vec{J}_{3,lattice}$ (shortened to $\vec{J}_3$ since $\vec{J}_{3,dis}$ is not calculated) HFACF. With the summation over a commensurate mesh, both $\vec{J}_{2,dis}$ and $\vec{J}_3$ are taken as real values. Similar to the $\vec{J}_2$, the $\vec{J}_{2,dis}$ equation (Eq 2.85) is a function of only one q-point. Thus the corresponding HFACF orthogonality rule is:

$$\begin{aligned}\langle \vec{J}_{2,dis}\vec{J}^*_{2,dis}\rangle &= \langle \sum_{\vec{q}} \vec{J}_{2,dis}(\vec{q}) | \sum_{\vec{q}'} \vec{J}^*_{2,dis}(\vec{q}')\rangle \delta(\vec{q} - |\vec{q}'|) \\ &= 2\sum_{\vec{q}} \langle \vec{J}_{2,dis}(\vec{q}) | \vec{J}^*_{2,dis}(\vec{q})\rangle\end{aligned} \tag{6.7}$$

Although $\vec{J}_3$ is a function of 3 q-points ($\vec{q}_1$,$\vec{q}_2$, and $\vec{q}_3$), the domain of these q-points are restricted by the selection rule $\Delta(\vec{q}_1 + \vec{q}_2 + \vec{q}_3)$. Given two q-points $\vec{q}_1'$ and $\vec{q}_1$" with selection rules, $\Delta(\vec{q}_1' + \vec{q}_2' + \vec{q}_3')$ and $\Delta(\vec{q}_1" + \vec{q}_2" + \vec{q}_3")$, all cross mode interactions of $\vec{q}_1'$ are assumed allowable with the set $\Delta(\vec{q}_1' + \vec{q}_2' + \vec{q}_3')$ but not with the set $\Delta(\vec{q}_1" + \vec{q}_2" + \vec{q}_3")$. This defines the $\vec{J}_3$ HFACF

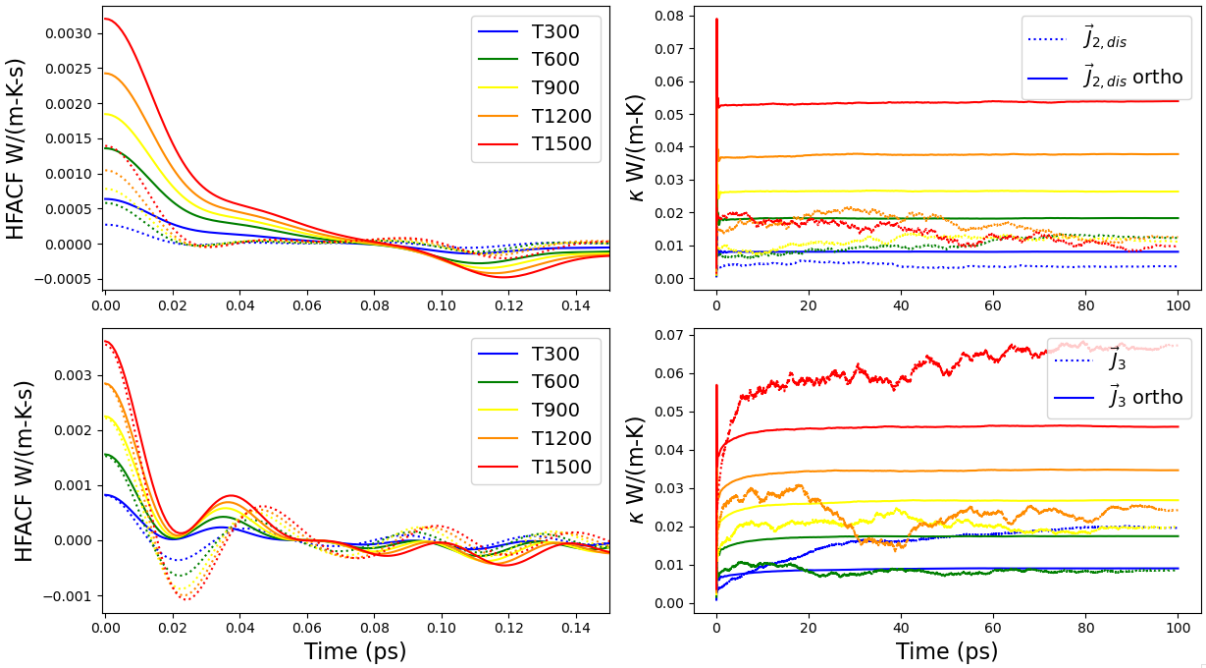

Figure 6.5: (top left) $\langle \vec{J}_2 \vec{J}_2^* \rangle$ HFACF and (top right) corresponding thermal conductivity by integration at all temperatures. (bottom left) $\langle \vec{J}_3 \vec{J}_3^* \rangle$ HFACF with (bottom right) resultant thermal conductivity by integration.

orthogonality as:

$$\begin{aligned} \langle \vec{J}_3 \vec{J}_3^* \rangle &= \langle \sum_{\vec{q}'} \sum_{\vec{q}_2' \vec{q}_3'} \vec{J}_3(\vec{q}', \vec{q}_2', \vec{q}_3') | \sum_{\vec{q}''} \sum_{\vec{q}_2'' \vec{q}_3''} \vec{J}_3^*(\vec{q}'', \vec{q}_2'', \vec{q}_3'') \rangle \delta(\vec{q}' - |\vec{q}''|) \\ &= 2 \sum_{\vec{q}'} \langle \sum_{\vec{q}_2' \vec{q}_3'} \vec{J}_3(\vec{q}', \vec{q}_2', \vec{q}_3') | \sum_{\vec{q}_2' \vec{q}_3'} \vec{J}_3^*(\vec{q}', \vec{q}_2', \vec{q}_3') \rangle \end{aligned} \tag{6.8}$$

By Fig 6.5, the orthogonality rule works to reduce the long time oscillations of the HFACF even with the double summation of the $\vec{J}_3$ heat flux. The amplitude of the $\vec{J}_{2,dis}$ HFACF differs by a factor of 2.3 when enforcing orthogonality where as the $\vec{J}_3$ HFACF differences are marginal. A factor of 2.3 could arise from the following cases between $\vec{J}_2(\vec{q})$ and $\vec{J}_2(-\vec{q})$: 1) they do not correlate with one another or 2) there is a significant negative cross correlation between these q-points. Although more work might need to be done to clarify the origin of the deviation for the $\vec{J}_{2,dis}$ HFACF, both orthogonality rules saturate the integration for κ. Both κ increasing with temperature are expected if 3^{rd} order anharmonicity increases with temperature and the total displacement of atoms increasing to an average of 12% of the lattice constant at 1500K.

Temp (K)	κ_{22}	$\kappa_{2_{dis}2_{dis}}$	κ_{33}	$\kappa_{22_{dis}}$	κ_{23}	$\kappa_{2_{dis}3}$	κ_{sum}
300	54.881	0.008	0.009	0.022	-0.699	-0.005	54.215
600	29.380	0.018	0.018	0.003	-0.719	-0.011	28.689
900	17.399	0.026	0.027	0.005	-0.669	-0.017	16.771
1200	10.814	0.038	0.035	-0.002	-0.552	-0.025	10.309
1500	8.066	0.054	0.046	-0.017	-0.549	-0.037	7.597

Table 6.2: All of the calculated thermal conductivity contributions up to the 3^{rd} order.κ_{ab} refers to the integration of the $\langle \vec{J}_a(0)\vec{J}_b(t)\rangle$ HFACF while κ_{sum} comes from the addition of all the calculated heat flux.

6.4 κ From All Orders

After applying the orthogonality rule to all the HFACF, all the component including the cross terms as displayed in Table 6.2. While κ_{33}, the thermal conductivity contribution from the $\langle \vec{J}_3(0)\vec{J}_3(t)\rangle$ HFACF, is 3 order of magnitudes smaller than κ_{22}, the cross term κ_{23} is 6.8% of the total κ_{22}. Based on the absolute magnitudes of all the κ contributions and truncation of heat flux of the order $\vec{J}_{3,dis}$ and above, only accounting for the lattice site heat flux $\vec{J}_{3,lattice}$ and $\vec{J}_{2,lattice}$ would give a prediction within 1.05% of the total prediction. This might change for a system with a higher percentage of the atomic displacement to the lattice constant.

The limitations of a heat flux truncation $\vec{J}_3$ and possible importance of the $\vec{J}_4$ heat flux can be seen with a comparison of the $\vec{J}_3$ cross terms (Figs 6.6 and 6.7) and inclusion of $\vec{J}_4$ terms (Fig 6.6) calculated by Sun Allen [47] Even with the differences of dimensions (two- vs three-dimensional) and potentials (Lennard-Jones vs GAP), similar large negative cross terms with $\vec{J}_3$ and $\vec{J}_2$. Sun & Allen attributes all of the negative cross terms involving $\vec{J}_3$ to the purely imaginary 3^{rd} order phonon-phonon interactions by Fermi's Golden Rule based on the inversion symmetry shown by Ipatova et. al. [24]. The inclusion of the $\vec{J}_4$ terms led to an overall increase in the predicted thermal conductivity after accounting for the negative cross components by $\vec{J}_3$.[47]. While this gives support for an improved implementation of the 4^{th} order heat flux (and renormalized forces), there is no guarantee that this will compensate for the underestimated κ_{22} compared to perturbation theory. However, this would clarify if the underestimated lifetimes is due to 4^{th+} order anharmonicity or sampling issues due to the simulation time. Similar work [40], up to 500K with EMD simulations and GAP with 200 ps HFACF, predicted the κ

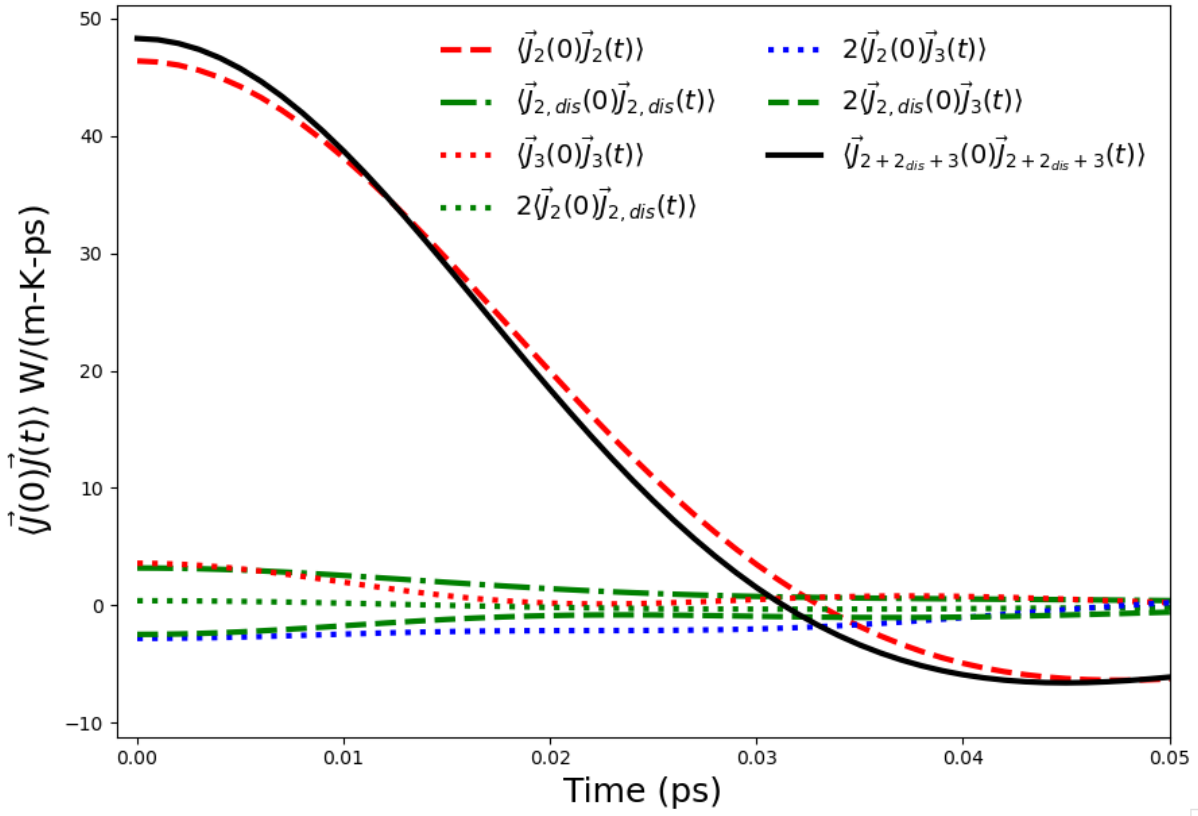

Figure 6.6: All HFACF and cross terms by combinations of $\vec{J}_2$,$\vec{J}_{2,dis}$, and $\vec{J}_3$ averaged over x,y,z at 1500K

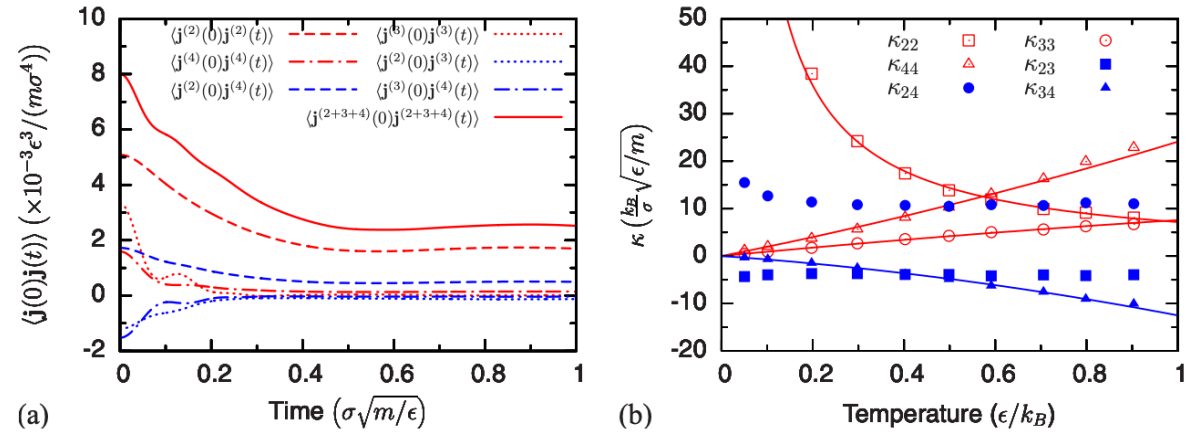

Figure 6.7: Higher order heat flux calculations by Sun Allen with MD and a Lennard-Jones potential of a two-dimensional triangular lattice.[48, 47] (a) HFACF with $\mathbf{j}^{(a)}$ being the lattice site heat flux with the ath order FC matrix at temperature T=.2 ϵ/k_b and (right) corresponding κ by G-K integration at all temperatures.

as 121 W/(m-K) at room temperature, which gives evidence a longer run-time of $\sim 400+$ ps simulation time.

6.5 Conclusions

In summary, our numeric analysis reported in this chapter emphasises the potency of the q-projected force fitting as a robust tool for comprehending anharmonicity and constructing temperature-dependent anharmonic force constant matrices at very high temperature, beyond the perturbation approximation. This algorithm likely exhibits superior numerical robustness compared to the real-space super-cell-based temperature-dependent-effective-potential approach, as it allows the enforcement of q-space symmetry to mitigate numeric noises effectively. While the current study applied the q-projected force fitting to derive temperature-dependent FC matrices, this technique holds promise for extending its utility to create innovative inter-atomic potential fittings akin to the GAP potential. The resulting temperature-dependent FC3, encapsulated by $\vec{J}_{3,lattice}$, imparts an overall negative correction to thermal conductivity (κ_L) when considering all cross terms, resembling behavior observed in 2D systems. Although the use of $\vec{f}_4^{eff}$ with the selection rule $\Delta(-\vec{q}+\vec{q}_2)$ yielded inconclusive results, it nonetheless provided valuable insights into the significance of the selection rule and potentially U-process-like selection rules. Future calculations should consider adopting a q-projected $\vec{f}_4^{eff}$, incorporating either the selection rule $\Delta(-\vec{q}+\vec{q}+\vec{q}_3-\vec{q}_3)$ or $\Delta(-\vec{q}+\vec{q}_2+\vec{q}_3+\vec{q}_4)$, contingent upon improved resources or parallelization. Validation of this approach with Linear Regression Model fitting will further enhance its credibility and applicability.

Chapter 7

Final Remarks

The rapid progression of machine-learning interatomic potentials (MLIAP) has opened avenues for direct exploration of anharmonic lattice dynamics in molecular dynamics simulations, transcending the constraints of perturbation approximations. Our primary objective is to quantitatively improve our understanding of the complex heat conduction mechanisms in lattices at elevated temperatures, where anharmonic effects, though significant, remain comparatively smaller than their harmonic counterparts. In pursuit of this goal, we harness the capabilities of GAP-type MLIAP, which is regarded as one of the most precise MLIAP models available, despite the accompanying computational overhead. To mitigate the increased computational costs, we implement an efficient q-space symmetrization technique, a strategic measure that substantially diminishes the numerical uncertainty inherent in molecular dynamics simulations applied to crystalline structures.

Our investigation, detailed in Chapter 4, unequivocally affirms the merit of employing q-space symmetry to alleviate noise in the 1-phonon spectra in MD simulations, a methodology we advocate for widespread adoption in future crystal studies. This not only expedites the fitting algorithm but also elevates the numerical precision of both the renormalized frequency (ω) and phonon lifetime (τ). Our MD simulations, presented in this dissertation, underscore the distinct numeric sensitivities governing the renormalized phonon frequencies and lifetimes. While ω exhibits minimal variation in response to changes in the fitting algorithm, τ proves more susceptible, leading to the formulation of an "accidental degeneracy" rule during fitting. This rule serves dual purposes: it succinctly encapsulates the success in capturing the temperature dependence of ω and acknowledges the partial success in modeling τ, particularly for low-frequency

acoustic phonons. However, the underestimation of lifetimes in these low-frequency acoustic modes consistently results in the predicted lattice thermal conductivity (κ_L), derived from the single-mode relaxation time approximation, falling below experimental and perturbation results, even at elevated temperatures. Exploring a hybrid approach that integrates perturbation treatment of acoustic modes at the lowest frequencies or engages in a dedicated low-frequency projected MD simulation might be a promising avenue for future research. This strategy has the potential to generate more robust predictions of κ_L without incurring the substantial numerical costs associated with conventional methods aimed at enhancing MD simulation accuracy, such as expanding cell sizes and extending time periods in MD simulations.

Our investigations, as discussed in Chapters 5-6, showcase the promise of Molecular Dynamics (MD) simulations based on Machine-Learning Interatomic Potentials (MLIAP) for modeling thermal transport properties. In extending beyond the Peierls kinetic model of phonon heat currents, our studies reveal that the contribution of anharmonic terms becomes non-negligible at high temperatures. Furthermore, our introduced algorithm, projecting an approximate Hardy's lattice model of heat flux into q-space, proves instrumental in mitigating the numeric uncertainties commonly encountered in conventional MD simulations.

The q-projection technique we have developed in this dissertation research effectively resolves numerical challenges in the Green-Kubo method by employing heat flux summation over commensurate grid symmetries. This approach asserts that all cross q-point correlations are zero unless $\vec{q} = -\vec{q}$. Demonstrated efficacy was observed even with a selection rule, particularly with the 3^{rd} order heat flux. The significance of cross correlations is evident in both inter/intra-mode heat flux cross correlations and second/third-order heat flux cross correlations, each contributing to a reduction in thermal conductivity predictions by 0.94 W/(m-K) and 0.549 W/(m-K), respectively, at 1500K, with the former being overlooked in the Wigner transport equation.

While the attempt to calculate a renormalized FC_4 encountered challenges with an effective FC_2 folding in q-space, this emphasized the critical role of the selection rule in addressing anharmonicity. A selection rule of $\Delta(-\vec{q} + \vec{q} + \vec{q}_3 - \vec{q}_3)$ or $\Delta(-\vec{q} + \vec{q}_2 + \vec{q}_3 + \vec{q}_4)$ could be explored further through testing with q-projected forces. The q-projected 3^{rd} order force fitting

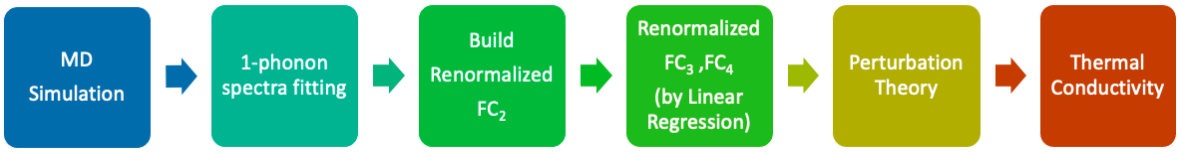

Figure 7.1: Mixed approach to calculating thermal conductivity with MD and perturbation theory.

illustrated the flexibility of this approach in handling anharmonic systems compared to real space force fitting. Additionally, it showcased how mode projection could determine anharmonicity per mode instead of per q-point. Alternatively, our proposed fitting technique could be applied to generate innovative interatomic potentials utilizing a q-space fitting approach instead of a real-space fitting.

Despite challenges in clarifying lifetime predictions within the reported MD simulation parameters, the method found success in determining renormalized and calibrated frequencies. A hybrid approach, combining MD and perturbation calculations as illustrated in Fig 7.1, capitalizes on the frequency-based temperature information from MD simulations and the reliability of perturbation. The outcomes of this combined method, featuring only the renormalized FC_2 and FC_3, are depicted in Fig 7.2. Temperature-dependent calibrated FC_2 values are defined based on the calibrated FC_2 at 300K, incorporating the temperature-dependent frequency shift from MD simulations. While bare FC_2 perturbation results predict values below the theoretically theorized lattice conductivity according to experimental results, the renormalized FC_3 perturbation outcomes align more closely with the total experimental measurements.

Currently, perturbation calculations incorporate the real space weight, W_3^1, of the renormalized FC_3, and further efforts are needed to integrate the q-space weight into these calculations. Considering the distribution of $W_3^1(\vec{q})$ in q-space, incorporating the overall weights would result in a downward shift, consequently lowering the renormalized FC_3. According to Fermi's Golden Rule, the scattering matrix would be constituted solely of 3-phonon interactions, with only an FC_3 as an input. Consequently, the predicted lifetime and κ would increase, given their inverse proportionality to the scattering matrix. The introduction of 4-phonon interactions to the scattering matrix, involving a renormalized FC_4, diminishes the lifetime, as

expressed by $\frac{1}{\tau} = \frac{1}{\tau_3} + \frac{1}{\tau_4}$. This renormalized FC_4 could potentially play a pivotal role in solidifying lattice thermal conductivity through perturbation calculations, especially with FC_4 implementations like FourPhonon.

In summary, the combination of highly accurate Machine-Learning Interatomic Potentials (MLIPs) and Molecular Dynamics (MD) simulations establishes a promising computational framework for the exploration of anharmonic lattice dynamics at exceedingly high temperatures, surpassing the limitations of perturbation approximations. Our study highlights the paramount importance of leveraging crystal symmetries in MD-based simulations. For instance, in the context of silicon crystals, our models comprising 4096 atoms prove sufficiently large, aided by our q-space symmetrization algorithm, to capture anharmonicity-induced frequency renormalization, even at temperatures as high as 1500K. However, our evaluation of phonon lifetimes yields mixed results. While we can quantitatively predict lifetimes for most mid and high-frequency modes with greater accuracy than achievable through inelastic neutron scattering, our MD results for low-frequency acoustic phonons, characterized by longer lifetimes, only reach a semi-quantitative level. Unfortunately, these low-frequency, long-lifetime acoustic phonon modes exert a substantial influence on total thermal conductivity. Consequently, it seems that significantly prolonged MD simulation times may be necessary to notably enhance the numerical accuracy of predicted lifetimes for these modes. Under the current simulation parameters, addressing the lifetimes for low-frequency acoustic modes at the perturbation theory level appears prudent, with the minimum inputs being the renormalized FC_2, FC_3, and FC_4.

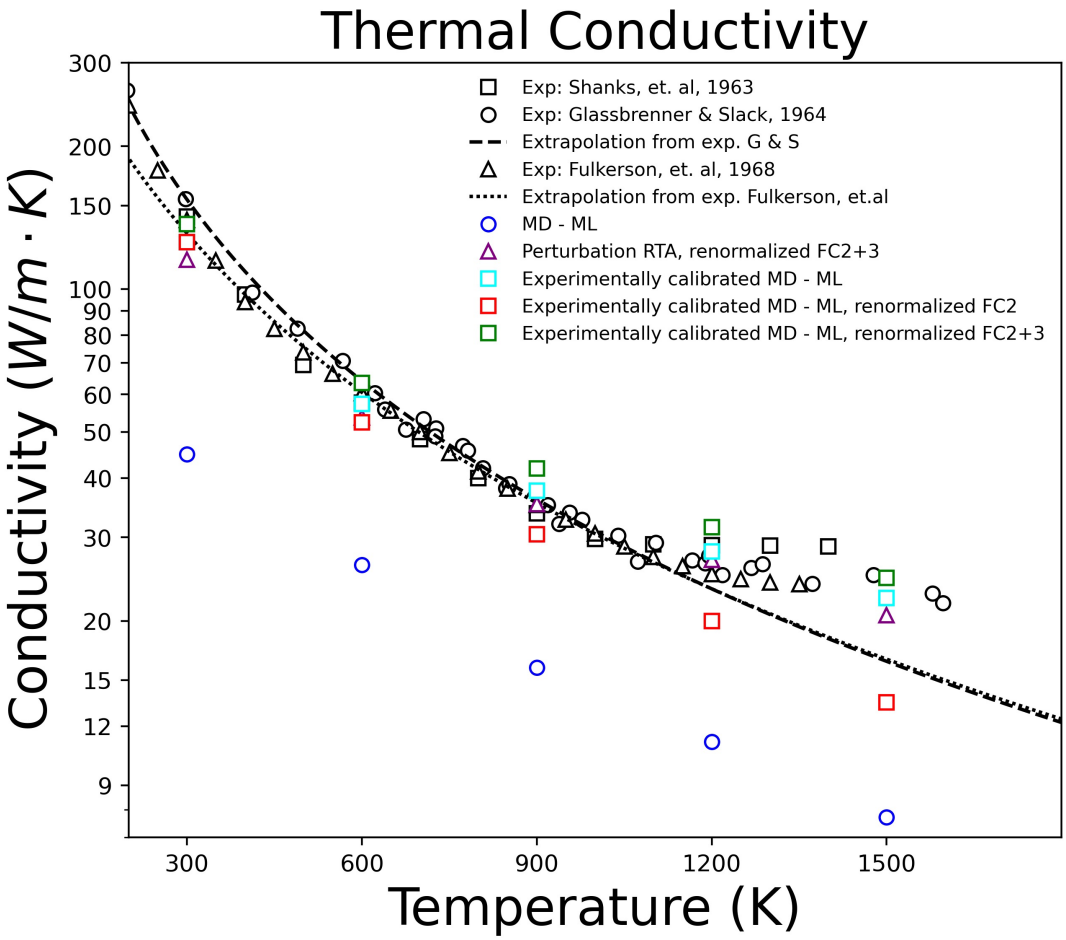

Figure 7.2: Thermal conductivity from (blue circles) MD with the RTA approximation, perturbation theory with (magenta triangle) renormalized FC_2 and FC_3, (blue square) calibrated FC_2 (300K with perturbation temperature prediction) and bare phonon FC_3, (red square) calibrated FC_2 (300K with MD temperature prediction) and bare phonon FC_3, and (green square) calibrated FC_2 (300K with MD temperature prediction) and renormalized phonon FC_3. Extrapolation lines (dashed by Glassbrenner Slack [17], and dotted by Fulkerson, et. al. [16]) are proposed lattice thermal conductivity based on experimental results

References

[1] Philip B Allen and Joseph L Feldman. Thermal conductivity of disordered harmonic solids. *Physical Review B*, 48(17):12581, 1993.

[2] Neil W Ashcroft and ND Mermin. Solid state. *Physics (New York: Holt, Rinehart and Winston) Appendix C*, 1976.

[3] Albert P Bartók, James Kermode, Noam Bernstein, and Gábor Csányi. Machine learning a general-purpose interatomic potential for silicon. *Physical Review X*, 8(4):041048, 2018.

[4] Paul Boone, Hasan Babaei, and Christopher E Wilmer. Heat flux for many-body interactions: corrections to lammps. *Journal of chemical theory and computation*, 15(10):5579–5587, 2019.

[5] B. N. Brockhouse and P. K. Iyengar. Normal vibrations of germanium by neutron spectrometry. *Phys. Rev.*, 108:894–895, Nov 1957.

[6] David G Cahill, My Katiyar, and JR Abelson. Thermal conductivity of a-si: H thin films. *Physical review B*, 50(9):6077, 1994.

[7] Christian Carbogno, Rampi Ramprasad, and Matthias Scheffler. Ab initio green-kubo approach for the thermal conductivity of solids. *Physical review letters*, 118(17):175901, 2017.

[8] B Chakraborty and PB Allen. Boltzmann theory generalized to include band mixing: A possible theory for" resistivity saturation" in metals. *Physical Review Letters*, 42(11):736, 1979.

[9] David R Clarke and Simon R Phillpot. Thermal barrier coating materials. *Materials today*, 8(6):22–29, 2005.

[10] RA Cowley. The lattice dynamics of an anharmonic crystal. *Advances in Physics*, 12(48):421–480, 1963.

[11] P. Debye. Zur theorie der spezifischen wärmen. *Annalen der Physik*, 344(14):789–839, 1912.

[12] G Dolling. Lattice vibrations in crystals with the diamond structure. In *Inelastic Scattering of Neutrons in Solids and Liquids. V. II. Proceedings of the Symposium on Inelastic Scattering of Neurons in Solids and Liquids*, 1963.

[13] Zheyong Fan, Luiz Felipe C Pereira, Hui-Qiong Wang, Jin-Cheng Zheng, Davide Donadio, and Ari Harju. Force and heat current formulas for many-body potentials in molecular dynamics simulations with applications to thermal conductivity calculations. *Physical Review B*, 92(9):094301, 2015.

[14] Tianli Feng, Lucas Lindsay, and Xiulin Ruan. Four-phonon scattering significantly reduces intrinsic thermal conductivity of solids. *Physical Review B*, 96(16):161201, 2017.

[15] Tianli Feng and Xiulin Ruan. Quantum mechanical prediction of four-phonon scattering rates and reduced thermal conductivity of solids. *Physical Review B*, 93(4):045202, 2016.

[16] W. Fulkerson, J. P. Moore, R. K. Williams, R. S. Graves, and D. L. McElroy. Thermal conductivity, electrical resistivity, and seebeck coefficient of silicon from 100 to 1300°k. *Phys. Rev.*, 167:765–782, Mar 1968.

[17] C. J. Glassbrenner and Glen A. Slack. Thermal conductivity of silicon and germanium from 3°k to the melting point. *Phys. Rev.*, 134:A1058–A1069, May 1964.

[18] Kiarash Gordiz, David J Singh, and Asegun Henry. Ensemble averaging vs. time averaging in molecular dynamics simulations of thermal conductivity. *Journal of Applied Physics*, 117(4), 2015.

[19] Xiaokun Gu, Shouhang Li, and Hua Bao. Thermal conductivity of silicon at elevated temperature: role of four-phonon scattering and electronic heat conduction. *International Journal of Heat and Mass Transfer*, 160:120165, 2020.

[20] Zherui Han, Xiaolong Yang, Wu Li, Tianli Feng, and Xiulin Ruan. Fourphonon: An extension module to shengbte for computing four-phonon scattering rates and thermal conductivity. *Computer Physics Communications*, 270:108179, 2022.

[21] Robert J Hardy. Energy-flux operator for a lattice. *Physical Review*, 132(1):168, 1963.

[22] Jian He and Terry M Tritt. Advances in thermoelectric materials research: Looking back and moving forward. *Science*, 357(6358):eaak9997, 2017.

[23] Olle Hellman, Peter Steneteg, Igor A Abrikosov, and Sergei I Simak. Temperature dependent effective potential method for accurate free energy calculations of solids. *Physical Review B*, 87(10):104111, 2013.

[24] IP Ipatova, AA Maradudin, and RF Wallis. Temperature dependence of the width of the fundamental lattice-vibration absorption peak in ionic crystals. ii. approximate numerical results. *Physical Review*, 155(3):882, 1967.

[25] Jun Kang and Lin-Wang Wang. First-principles green-kubo method for thermal conductivity calculations. *Physical Review B*, 96(2):020302, 2017.

[26] PH Keesom and G Seidel. Specific heat of germanium and silicon at low temperatures. *Physical Review*, 113(1):33, 1959.

[27] Dennis S Kim, O Hellman, J Herriman, HL Smith, JYY Lin, N Shulumba, JL Niedziela, CW Li, DL Abernathy, and B Fultz. Nuclear quantum effect with pure anharmonicity and the anomalous thermal expansion of silicon. *Proceedings of the National Academy of Sciences*, 115(9):1992–1997, 2018.

[28] Dennis S Kim, O Hellman, N Shulumba, Claire N Saunders, Jiao YY Lin, Hillary L Smith, JE Herriman, Jennifer L Niedziela, Douglas L Abernathy, Chen W Li, et al.

Temperature-dependent phonon lifetimes and thermal conductivity of silicon by inelastic neutron scattering and ab initio calculations. *Physical Review B*, 102(17):174311, 2020.

[29] Walter Kohn and Lu Jeu Sham. Self-consistent equations including exchange and correlation effects. *Physical review*, 140(4A):A1133, 1965.

[30] Ling-Ti Kong. latgen, 2023.

[31] Wu Li, Jesús Carrete, Nebil A. Katcho, and Natalio Mingo. ShengBTE: a solver of the Boltzmann transport equation for phonons. *Comp. Phys. Commun.*, 185:1747–1758, 2014.

[32] Wei Lv and Asegun Henry. Examining the validity of the phonon gas model in amorphous materials. *Scientific reports*, 6(1):37675, 2016.

[33] AA Maznev and OB Wright. Demystifying umklapp vs normal scattering in lattice thermal conductivity. *American journal of physics*, 82(11):1062–1066, 2014.

[34] José Menéndez and Manuel Cardona. Temperature dependence of the first-order raman scattering by phonons in si, ge, and $\alpha - \mathrm{Sn}$: Anharmonic effects. *Phys. Rev. B*, 29:2051–2059, Feb 1984.

[35] Matthew Newville, Till Stensitzki, Daniel B Allen, Michal Rawlik, Antonino Ingargiola, and Andrew Nelson. Lmfit: Non-linear least-square minimization and curve-fitting for python. *Astrophysics Source Code Library*, pages ascl–1606, 2016.

[36] Yasumasa Okada and Yozo Tokumaru. Precise determination of lattice parameter and thermal expansion coefficient of silicon between 300 and 1500 k. *Journal of applied physics*, 56(2):314–320, 1984.

[37] F. Pedregosa, G. Varoquaux, A. Gramfort, V. Michel, B. Thirion, O. Grisel, M. Blondel, P. Prettenhofer, R. Weiss, V. Dubourg, J. Vanderplas, A. Passos, D. Cournapeau, M. Brucher, M. Perrot, and E. Duchesnay. Scikit-learn: Machine learning in Python. *Journal of Machine Learning Research*, 12:2825–2830, 2011.

[38] Rudolf Ernst Peierls. *Quantum theory of solids*. Oxford University Press, 1955.

[39] William A Phillips. Tunneling states in amorphous solids. *Journal of low temperature physics*, 7:351–360, 1972.

[40] Xin Qian, Shenyou Peng, Xiaobo Li, Yujie Wei, and Ronggui Yang. Thermal conductivity modeling using machine learning potentials: application to crystalline and amorphous silicon. *Materials Today Physics*, 10:100140, 2019.

[41] Patrick K Schelling, Simon R Phillpot, and Pawel Keblinski. Comparison of atomic-level simulation methods for computing thermal conductivity. *Physical Review B*, 65(14):144306, 2002.

[42] Wahyu Setyawan and Stefano Curtarolo. High-throughput electronic band structure calculations: Challenges and tools. *Computational Materials Science*, 49(2):299–312, 2010.

[43] HR Shanks, PD Maycock, PH Sidles, and GC Danielson. Thermal conductivity of silicon from 300 to 1400 k. *Physical Review*, 130(5):1743, 1963.

[44] Michele Simoncelli, Nicola Marzari, and Francesco Mauri. Unified theory of thermal transport in crystals and disordered solids. *arXiv preprint arXiv:1901.01964*, 2019.

[45] Frank H Stillinger and Thomas A Weber. Computer simulation of local order in condensed phases of silicon. *Physical review B*, 31(8):5262, 1985.

[46] Alexander Stukowski. Visualization and analysis of atomistic simulation data with OVITO-the Open Visualization Tool. *Modelling Simul. Mater. Sci. Eng.*, 18(1):015012, January 2010.

[47] Tao Sun and Philip B Allen. Lattice thermal conductivity: Computations and theory of the high-temperature breakdown of the phonon-gas model. *Physical Review B*, 82(22):224305, 2010.

[48] Tao Sun, Xiao Shen, and Philip B Allen. Phonon quasiparticles and anharmonic perturbation theory tested by molecular dynamics on a model system. *Physical Review B*, 82(22):224304, 2010.

[49] Xiaoli Tang and Jianjun Dong. Lattice thermal conductivity of mgo at conditions of earth's interior. *Proceedings of the National Academy of Sciences*, 107(10):4539–4543, 2010.

[50] Jerry Tersoff. New empirical approach for the structure and energy of covalent systems. *Physical review B*, 37(12):6991, 1988.

[51] A. P. Thompson, H. M. Aktulga, R. Berger, D. S. Bolintineanu, W. M. Brown, P. S. Crozier, P. J. in 't Veld, A. Kohlmeyer, S. G. Moore, T. D. Nguyen, R. Shan, M. J. Stevens, J. Tranchida, C. Trott, and S. J. Plimpton. LAMMPS - a flexible simulation tool for particle-based materials modeling at the atomic, meso, and continuum scales. *Comp. Phys. Comm.*, 271:108171, 2022.

[52] Aidan P Thompson, Laura P Swiler, Christian R Trott, Stephen M Foiles, and Garritt J Tucker. Spectral neighbor analysis method for automated generation of quantum-accurate interatomic potentials. *Journal of Computational Physics*, 285:316–330, 2015.

[53] Fei Tian, Bai Song, Xi Chen, Navaneetha K Ravichandran, Yinchuan Lv, Ke Chen, Sean Sullivan, Jaehyun Kim, Yuanyuan Zhou, Te-Huan Liu, et al. Unusual high thermal conductivity in boron arsenide bulk crystals. *Science*, 361(6402):582–585, 2018.

[54] Atsushi Togo, Laurent Chaput, Terumasa Tadano, and Isao Tanaka. Implementation strategies in phonopy and phono3py. *J. Phys. Condens. Matter*, 35(35):353001, 2023.

[55] Raphael Tsu and Jesus Gonzalez Hernandez. Temperature dependence of silicon Raman lines. *Applied Physics Letters*, 41(11):1016–1018, 12 1982.

[56] BL Zink, R Pietri, and F Hellman. Thermal conductivity and specific heat of thin-film amorphous silicon. *Physical review letters*, 96(5):055902, 2006.

[57] Yunxing Zuo, Chi Chen, Xiangguo Li, Zhi Deng, Yiming Chen, Jörg Behler, Gábor Csányi, Alexander V Shapeev, Aidan P Thompson, Mitchell A Wood, et al. Performance and cost assessment of machine learning interatomic potentials. *The Journal of Physical Chemistry A*, 124(4):731–745, 2020.